UNIVERSITY OF CALIFORNIA SAN DIEGO

Dilute Nitride III-V Nanowires Grown on Si (111) by Gas-Source Molecular Beam Epitaxy

A dissertation submitted in partial satisfaction of the

requirements for the degree

Doctor of Philosophy

in

Material Science and Engineering

by

Rui La

Committee in charge:

Professor Charles W. Tu, Chair
Professor Prabhakar R. Bandaru
Professor Shadi A. Dayeh
Professor Yu-Hwa Lo
Professor Tina Nga Ng

2018

The dissertation of Rui La is approved, and it is acceptable in quality and form for publication on microfilm and electronically:

_____

_____

_____

_____

Co-chair

_____

Chair

University of California San Diego

2018

DEDICATION

To my family and Haoqing.

EPIGRAPH

Not pleased by external gains,
not saddened by personal losses.
— Fan Zhongyan

TABLE OF CONTENTS

LIST OF FIGURES

LIST OF TABLES

ACKNOWLEDGEMENTS

First of all, I would like to express my sincere gratitude to my advisor Prof. Charles W. Tu for the continuous support of my Ph.D. study. His patience, his valuable guidance all helped me during the last five years of study and life in UCSD. I have encountered many difficulties during my Ph.D. life and Prof. Tu has always been there to help me. The most valuable lessons I learned from him are his critical altitude to science and optimism. He gave me many good suggestions during my research and helped me with troubleshooting. What's more, he was always very generous to provide opportunities and space for my personal development and helped me with improving my drawbacks such as English writing and presentation skills.

In addition to my advisor, I greatly appreciate the kind support of the members of my thesis committee: Prof. Shadi Dayeh, Prof. Prabhakar Bandaru, Prof. Yu-Hwa Lo and Prof. Tina Nga Ng. I am sincerely grateful to Prof. Shadi Dayeh for his group's study on my sample GaAs/GaNAs nanowires grown patterned substrate and gave me valuable suggestions on my work.

I would like to appreciate Dr. Janet Pan for her great help in the growth and fabrication. Her expertise in Molecular Beam Epitaxy (MBE) solved several problems during my research and her experience in fabrication and characterization provided valuable suggestions to me. The enthusiasm and experience she shared are priceless. I also would like to thank Prof. Irina Buyanova and her group members in Sweden for their measurement and insight about my GaNAsP, GaAs/GaNAs nanowires samples. Their

experience and knowledge in applied physics broadened my horizon and provide numerous new ideas to my study.

I would like to thank my friends and fellow collegues at UCSD. I am greatly appreciated to Dr. Yanjin Kuang and Dr. Supanee Sukrittanon for teaching and training me all about MBE and troubleshooting skills. Dr. Supanee Sukrittanon devoted many of her precious time to show me the procedure of operating MBE, photoluminescence (PL) and different techniques in clean room. Dr. Yanjin Kuang helped me to come up with research ideas when I joined the group and provided his valuable experience in III-V semiconductor and devices. I would also thank Casey Sanchez and Jimmy Chuang for their help on lab works. They are not only my lab partners but also good friends in life. My thanks also go to Ren Liu, Renjie Chen, Yun Goo Ro and Atsunori Tanaka for the help with transmission electron microscopy (TEM), solar cell fabrication techniques, and X-ray diffraction measurements (XRD), respectively. I would also thank Weichuan Yao and Maribel Montero for their help with e-beam lithography. Many thanks to other colleagues with whom I have collaborated and assisted throughout my time at UCSD: Qian Ma, Dr. Ke Sun, Dr. Qing Gu and other lab members.

A special thanks to the staff in Nano3: Bernd Fruhberger, Larry Grissom, Sean Parks, Xuekun Lu, and Ryan Anderson. They were always there to provide technical support in the cleanroom whenever needed.

Lastly, I would like to thank my parents and my loving wife, Haoqing Zhu. My parents showed their great support to me whenever I ran into problems and always

believe in me. A very big thanks to my loving wife Haoqing Zhu for always supporting me in my life, care and patience on me.

Chapter 3 and chapter 4, in part, has been published in "Self-catalyzed Ga(N)AsP nanowires and GaAsP/GaNAsP core–shell nanowires grown on Si (111) by gas-source molecular beam epitaxy", Rui La, Janet L. Pan, Faebian Bastiman, Charles W. Tu, J. Vac. Sci., Technol. B 34, 02L108 (2016). The dissertation author was the primary investigator and author of this paper.

Chapter 5, in part, has been published in "Self-catalyzed core-shell GaAs/GaNAs nanowires grown on patterned Si (111) by gas-source molecular beam epitaxy", Rui La, Ren Liu, Weichuan Yao, Renjie Chen, Mattias Jansson, Janet L. Pan, Irina A. Buyanova, Jie Xiang, Shadi A Dayeh, Charles W. Tu, Appl. Phys. Lett., 111, 072106 (2017). The dissertation author was the primary investigator and author of this paper.

VITA

2010	B.S. in Materials Science and Engineering, University of Science and Technology, Beijing, Beijing
2012	M.S. in Material Science and Engineering, University of Florida, Gainesville, FL
2018	Ph.D. in Material Science and Engineering, University of California San Diego, CA

PUBLICATIONS

R. La, R. Liu, W. Yao, R. Chen, M. Jansson, J. L. Pan, I. A. Buyanova, J. Xiang, S. A Dayeh, C. W. Tu, "Self-catalyzed core-shell GaAs/GaNAs nanowires grown on patterned Si (111) by gas-source molecular beam epitaxy", *Appl. Phys. Lett*., 111, 072106 (2017).

R. La, J. L. Pan, F. Bastiman, C.W. Tu, "Self-catalyzed Ga (N) AsP nanowires and GaAsP/GaNAsP core–shell nanowires grown on Si (111) by gas-source molecular beam epitaxy", *J. Vac. Sci., Technol.* B 34, 02L108 (2016).

M. Jansson, S. Chen, **R. La,** J. E. Stehr, C. W. Tu, W. M. Chen, I. A. Buyanova, "Effects of Nitrogen Incorporation on Structural and Optical Properties of GaNAsP Nanowires", J. *Phys. Chem. C,* 121, 7047 (2017).

Q. Xu, **R. La,** Q. Cheng, Z. Zhang, R. Hong, Xi. Chen, Z. Wu, "Effect of rapid thermal annealing on Zn/ZnO layers", *J. Mater. Sci. Mater. Electron.* 24, 4075 (2013)

CONFERENCE PRESENTATIONS

(Invited talk) **R. La**, R. Liu, W. Yao, R. Chen, M. Jansson, J. L. Pan, I. A. Buyanova, J. Xiang, S. A Dayeh, C. W. Tu, "Self-catalyzed core-shell GaAs/GaNAs nanowires grown on patterned Si (111) by gas-source molecular beam epitaxy", China National Conference on Molecular Beam Epitaxy 2017, Taiyuan, Shanxi, PRC.

R. La, R. Liu, W. Yao, R. Chen, M. Jansson, J. L. Pan, I. A. Buyanova, J. Xiang, S. A Dayeh, C. W. Tu, "Investigation of GaAs/GaNAs nanowires grown on patterned Si (111) by gas-source molecular beam epitaxy", North American Molecular Beam Epitaxy Conference 2017, Galveston Island, Texas, USA.

R La, M. Jansson, S. Chen, J. Stehr, J. L. Pan, W. Chen, I. Buyanova, C.W. Tu, "Structural and optical effects of alloying with nitrogen in GaNAsP nanowires", Electronic Materials Conference 2016, Newark, Delaware,

R. La, R. Liu, W. Yao, J. L. Pan, J. Xiang, S. A Dayeh, C. W. Tu, "Selective area growth of core-shell GaAs/GaNAs nanowires grown on Si (111) by gas-source molecular beam epitaxy", North American Molecular Beam Epitaxy Conference 2016, Saratoga Springs, New York, USA.

R. La, J. L. Pan, and C. W. Tu, "Self-Catalyzed GaNAsP and GaAsP/GaNAsP Core-Shell Nanowires grown on Si (111) by Gas-Source Molecular Beam Epitaxy", North America Molecular Beam Epitaxy 2015, Mayan Riviera, Mexico

ABSTRACT OF THE DISSERTATION

Dilute Nitride III-V Nanowires Grown on Si (111) by Gas-Source Molecular Beam Epitaxy

by

Rui La

Doctor of Philosophy in Material Science and Engineering

University of California San Diego, 2018

Professor Charles W. Tu, Chair

III-V nanowires (NWs) have in recent years attracted an increasing research interest owing both to their interesting fundamental properties and to the prospect of numerous potential applications in electronics, optoelectronics, and photovoltaic. Dilute nitride NWs is a group of novel semiconductor material in which small amounts of N

atoms substrate group V elements in conventional III-V semiconductor. With the advantage of free of lattice mismatch constraints and high absorption coefficients, III-N-V NWs is a group of promising yet little-studied material for solar cell applications. As a first step towards III-N-V NW solar cells on Si, the goal of this dissertation is to optimize the growth conditions of different NWs including on arbitrary substrate, patterned substrate and core-shell NWs.

The dissertation is divided into three major parts. In the first part, we report epitaxial growth of dilute nitride GaNAsP nanowires (NWs) and GaAsP/ GaNAsP core–shell nanowires on Si (111) by a self-catalyzed method. Growth windows, structural properties are investigated. The structural properties and optical properties are characterized using SEM, photoluminescence (PL), EDX etc. The properties of GaAs/GaNAsP nanowires demonstrates that alloying GaAsP with nitrogen represents a viable and attractive approach of bandgap engineering, which allows efficient tuning of the electronic properties of the GaNAsP NWs as required for future optoelectronic and photonic applications.

The second part demonstrates the successful growth of GaAs/GaNAs core/shell nanowires on patterned Si substrate. The micro-PL and Transmission electron microscopy characterization results show good crystal structure of nanowires and minimal defects. The study illustrates the feasibility of the epitaxial growth of patterned GaAs with dilute nitride shells on Si substrates, which would have potential for Si-friendly intermediate band solar cells and telecom emitters.

In the last part, single pin-GaNP/GaNP/GaNP core/shell nanowires solar cell is fabricated utilizing e-beam writing technique. The metal contact is deposited by e-beam evaporation. The characteristic circuit current-voltage curve is measured and the performance of single nanowire solar cell is analyzed.

Chapter 1

Introduction

1.1 Motivation

Solar cell is an electronic device, which can collect the sun's energy to produce electricity. It has proven to be one of the most promising solutions to the world's energy crisis. Si-based solar cell technology has been very successful from laboratory to commercial integration and makes up to 90% market share[1] The cost-effectives property of silicon as well as increasing energy conversion efficiency make it attractive to both academia and industry. Since the first silicon solar cell was reported in 1941[2], there have been substantial improvements in silicon cell performance, culminating in the 26.7% value reported in the recent solar cell efficiency tables.[3] However, the progress of Si-based solar cell has remained stagnant for the past decade due to the Queisser-Shockley Limit. III-V compound semiconductor multi-junction (tandem) solar cells have made much progress in the last 15 years. They have the potential for achieving

high conversion efficiencies of over 40% and are promising for space and terrestrial applications. Therefore, the development of III-V compound semiconductor solar cells have been well developed because of its many materials characteristics such as high photovoltaic efficiency and flexible combination of a range of materials from binary to quaternary compounds with a corresponding flexibility of and bandgap engineering. More significantly, a number of these compounds interact strongly with light, since they largely retain direct bandgaps and correspondingly high absorption coefficients, and therefore also tend to radiate light efficiently. With these advantages, the III-V semiconductor is a group of materials well suited for opto-electronic applications. Figure 1.1 shows the progress of the past 25 years in solar cell[3]. The solar cell efficiency is calculated under 1-sun with cells of larger than 1 cm^2 area. Impressive progress has been made with monolithic III-V multi-junction cells where efficiency has been improved from 31.8% to 46%[3] over the 25-year period. Despite their higher efficiency, wide adoption of III-V solar cells is limited by their cost, especially the cost of the substrate. Thus, integration of high-efficiency III-V semiconductors directly onto Si substrate is a very attractive approach to create low-cost, highly efficient solar cells.

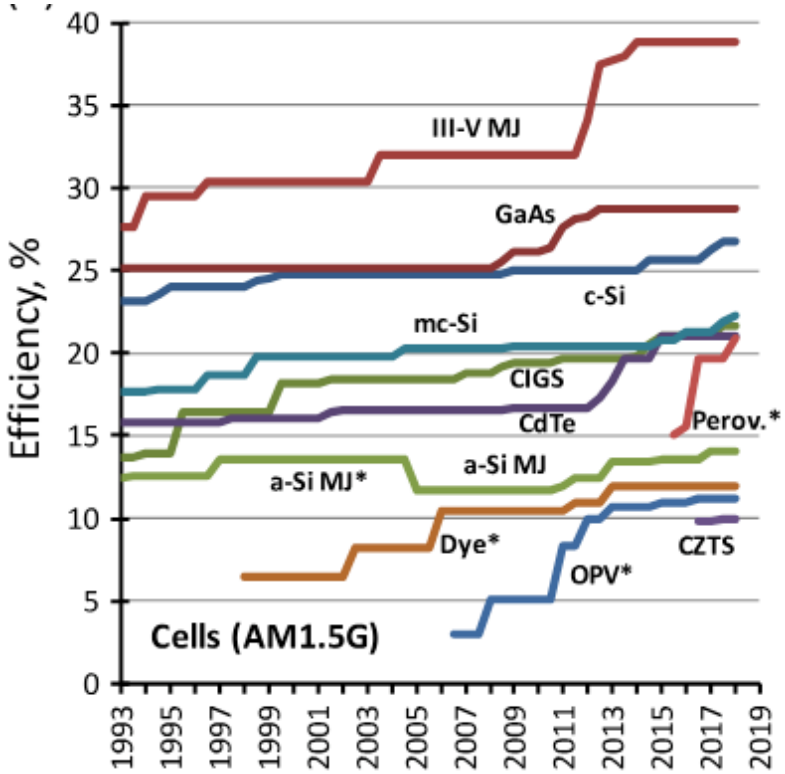

Figure 1.1 Twenty-five years of progress of highest confirmed efficiencies for ≥ 1 cm^2 area cells fabricated using the different technologies shown.[3]

The most commonly used substrates for III-V compound semiconductor materials growth are first GaAs and then InP, which have bandgaps near the ideal for solar conversion. Furthermore, materials compatible with these substrates are the most important. There are first of all lattice-matched compounds, which can be grown without strain relaxation and associated defects reducing device performance. From the bandgap of semiconductor we note that Si is close to lattice match with GaP and that a small amount of N (2%) to GaP can allow exact lattice matching to low cost Si substrates. The Si is therefore frequently used in designs of multi-junction of Si-III-V solar cells. Figure 1.2 shows transmission electron microscope (TEM) images and x-ray diffraction results

of various compositions of GaNP layers on a Si substrate[4]. The motivation of the structure is to have a two-junction device consisting of a 1.7-eV junction on a 1.1-eV silicon junction, which could reach the maximum theoretical efficiency for a two-junction cell of 38.75%[5]. The TEM images shows the defects are apparent at the GaP/Si interface but much less at the $GaN_{0.02}P_{0.98}$/Si interface.

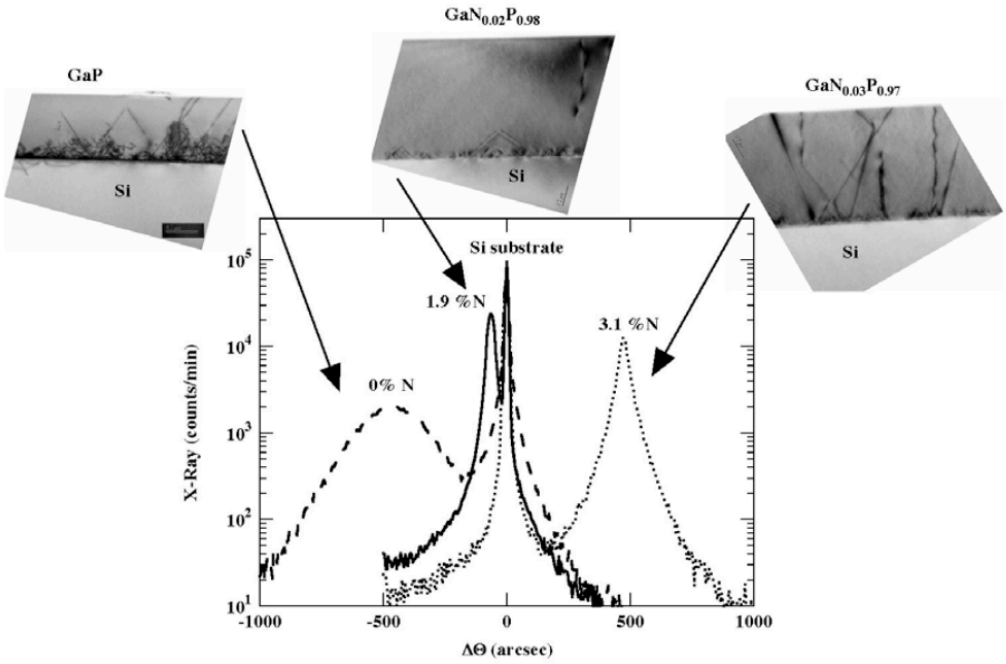

Figure 1.2 X-ray diffraction of GaN_xP_{1-x} grown on silicon taken in (004) reflection with corresponding TEM images.[4]

In recent years, it has been demonstrated that III-V semiconductor nanowires (NWs) can be successfully grown directly on Si substrates using molecular beam epitaxy (MBE), metalorganic chemical vapor deposition (MOCVD). [6-8] One of the advantages for growing III-V NWs on Si substrates as opposed to planar films is that the nanowire geometry effectively relaxes the lattice mismatch constraint due to their small interfacial

area.[9, 10] As a result, the interface between III-V nanowires and the Si substrate can posses minimal interfacial defect densities, low to no antiphase domain boundaries, and under optimized growth conditions defect-free III-V nanowire materials, all of which are attributes that are hard to accomplish with conventional planar thin film growth.

Successful growth of III-V NWs on Si was reported in recent publications. Araki et al. have grown mixed phase GaAs/GaNAs core/shell nanowires by plasma-assisted MBE and studied their photoluminescence characteristics.[11] Ahn et al. further conducted mechanistic growth studies to understand the influence of growth parameters on the resulting GaAs/GaNAs core/shell nanowires growth morphology.[12] Chen et al.[13] used micro-photoluminescence (μ-PL) and Stehr et al.[14] utilized photoluminescence and optically detected magnetic resonance (ODMR) spectroscopies to study non-radiative recombination processes in GaAs/GaNAs core/shell nanowires grown on Si by MBE. Through temperature-dependent PL, Chen et al. deduced the formation of localization potentials in GaAs cores upon the growth of GaNAs shells that can be overcome by thermal carrier at $T > 60K$.[15] Kasanaboina et al. used μ-PL, x-ray and Raman spectroscopy to study the N incorporation in GaAs/GaAsSbN/GaAs core/shell nanowires.[16] Using the vapor liquid solid (VLS) method, various III-V nanowires can be grown on Si with or without catalyst.

The ability to grow low-defect III-V NWs on Si makes it a very promising candidate for multi-junction solar cells. Another advantage of NW solar cells is its high absorption of light. Despite a small material volume in NW arrays as compared with that

in an epilayer geometry, it has been shown that optical absorption efficiency is increased due to multiple scattering and absorption – even a sparse NW array can absorb nearly 100% of the incident light, a property that is very promising for photovoltaic applications.[17]

1.2 Dilute nitride nanowires

Dilute nitride is a relatively new material system. According to the band anticrossing (BAC) model[18], the interaction between the host states and the N localized states results in two subbands, E_- and E_+ bands. The BAC model is able to predict the position of E_- and E_+ energy using a perturbation Hamiltonian.

$$\begin{vmatrix} E - E_M & C_{NM}\sqrt{x} \\ C_{NM}\sqrt{x} & E - E_N \end{vmatrix} = 0 \qquad (1.1)$$

where E_M is the dispersion relation for the matrix conduction band, E_N is the N state energy. C_{MN} is the interaction coefficient of the matrix conduction band and the N state energy and x is the N concentration. The large modification of the electronic band structure profoundly affects the optical and electrical properties of these materials.[19] In the $GaAs_xP_{1-x}$ alloy system, the N level falls below the conduction band edge for x > 0.3, resulting in a narrow E_- band which is suitable for intermediate band solar cells (IBSCs).[20,21] The E_- and E_+ bands can be calculated from the following formula:

$$E_{\pm}(k) = \frac{1}{2}\{[E_C(k) + E_N] \pm \sqrt{[E_C(k) - E_N]^2 + 4C_{NM}^2 \cdot x}\} \qquad (1.2)$$

where the E_C is the matrix lowest conduction band, and E_N is the N level in the GaAsP alloy, which is a function of As composition as shown previously. C_{NM} is the interaction

coefficient of the matrix conduction band and the N energy level, and x is the N content. As shown in Figure 1.2, GaAsP is an indirect bandgap material for [As] < 52% and the N states are higher than E_Γ for [As] > 0.67. Therefore, our desired [As] falls in the range between of 52% to 67%.

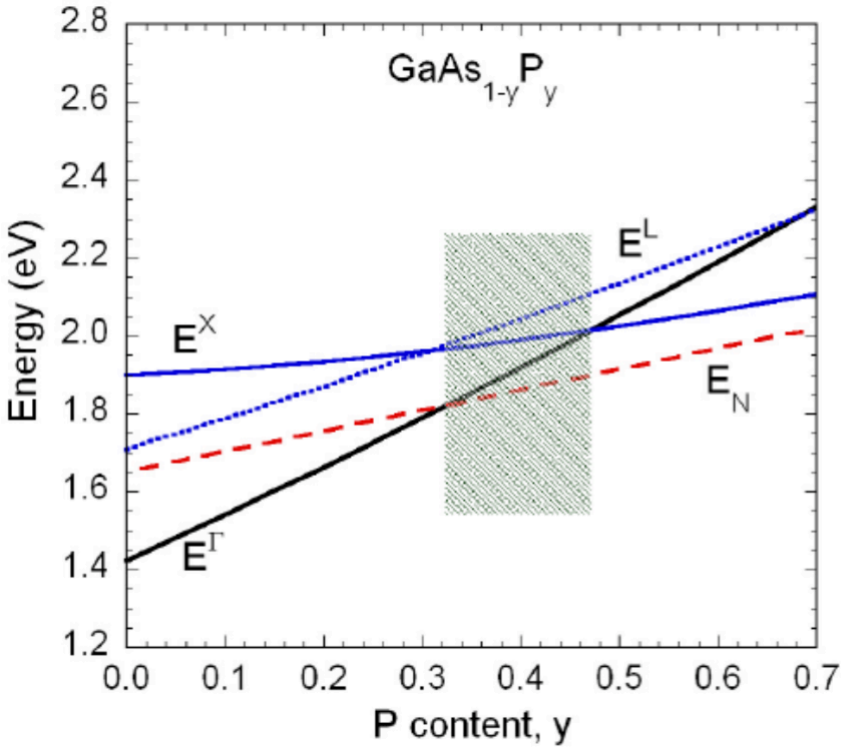

Figure 1.3: The N energy level position relative to the Γ band and the X band and the L band with different As composition in the GaAsP alloy[22]

Dilute nitrides NWs are a group of novel semiconductor material in which small amounts of N atoms substitute As or P (group V) elements in conventional III-V semiconductor. Many successful demonstration of dilute nitride NWs and their applications have been reported for a variety of materials with a broad spectral coverage before this dissertation. The following parts of this chapter will introduce some main

discoveries in dilute nitride nanowires.

GaAs/GaNAs core-shell NWs are a very promising material for long-wavelength applications. Figure 1.4 shows schematic dispersion relations for the sub-bands of $GaN_{0.005}As_{0.095}$ alloy near the Brillouin zone center. The bandgap of GaNAs decreases from 1.42 eV to 1.32 eV because incorporating N splits the conduction bandgap and the E_- band becomes the new conduction band. Chen et al.[13] have shown that this bandgap bowing effect is also true in GaAs/GaNAs core-shell NWs. From Figure 1.5 we can see the PL emission peak from GaNAs shells is approximately at 1.35 eV which is lower than the 1.467 eV from GaAs NW PL emission peak. This indicates that the PL emission in the core/shell NWs originates from the GaNAs shells with a smaller bandgap. In practice, Chen et al. demonstrated optically pumped lasing from the GaNAs shell of a single GaAs/GaNAs core-shell NW which represents the first step toward development of room-temperature infrared NW lasers based on dilute nitrides with extended tenability in the lasing wavelength.[24]

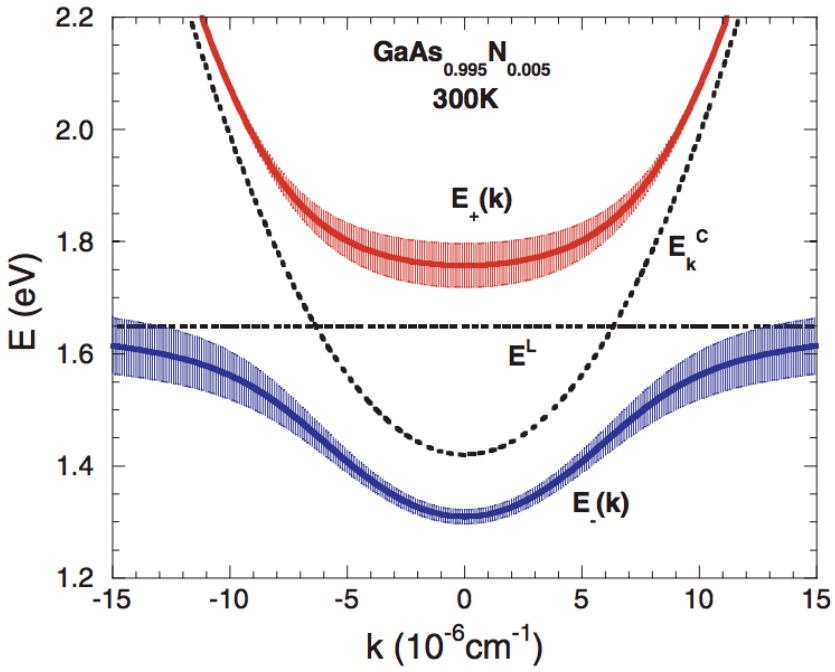

Figure 1.4 Conduction band restricting model according to BAC model for $GaN_{0.005}As_{0.095}$[23]

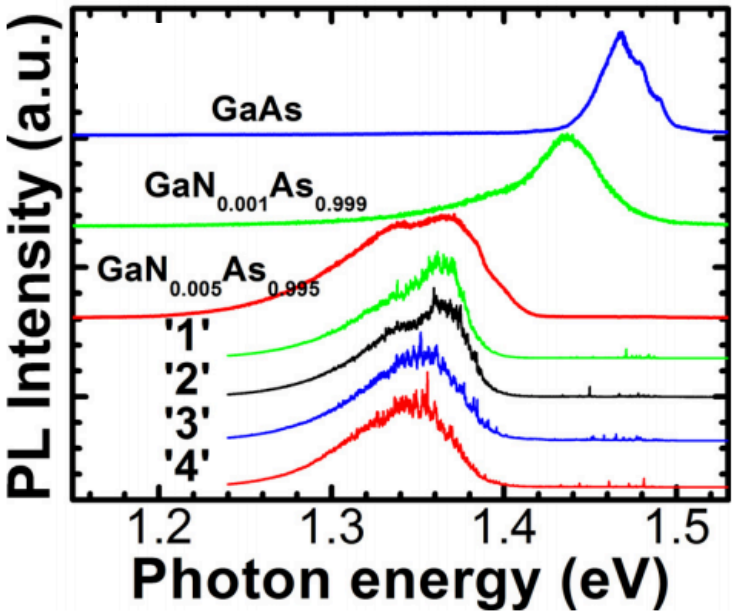

Figure 1.5 Representative PL spectra of the investigated structures obtained at 5 K. The three top spectra were measured from ensembles of GaAs NWs, GaAs/Ga $As_{0.999}N_{0.001}$, and GaAs/Ga $As_{0.995}N_{0.005}$ core/ shell NWs.[13]

Dilute nitride GaP/GaNP core-shell NWs are a promising candidate for

dual-junction wide band solar cells for several outstanding reasons. First, by introducing sufficient N concentration into GaP, the resulting GaNP exhibits a direct-bandgap.[24, 25] As N concentration passes ~0.4%, GaNP becomes a direct-bandgap semiconductor. In addition, N can be incorporated into GaP up to 16%[26] allowing the GaNP bandgap to be tunable from 1.22 eV to 2.15 eV, covering a wide range of the solar spectrum. The other members of our group have shown successful growth of GaNP, GaP/GaNP and GaNP/GaNP[27, 28] core/shell NWs, characterized their optical properties and investigated the effect of dilute nitride to the structural and optical properties of NWs.

1.3 Scope of dissertation

With the advantages of no lattice mismatch constraints and high absorption coefficients, III-N-V NWs are a group of promising yet little-studied material for solar cell applications. As a first step towards III-N-V NW solar cells on Si, the goal of this dissertation is to optimize the growth conditions of different NWs including self assembly, growth on a patterned substrate, and growth of core-shell NWs. The performance of a single NW solar cell is also investigated to study the limit of NW solar cells. Si is chosen as the substrate because of its cost effectiveness. In this dissertation, two branches of NWs growth are explored: (1) random growth on Si (111) substrate of Ga(N)AsP and GaAsP/GaNAsP NWs in Chapters 3 and 4, respectively, and (2) selective area growth of GaAs/GaNAs core-shell NWs on SI (111) substrate in Chapter 5. We also discuss the fabrication and measurement of single p-GaNP/i-GaNP/n-GaNP NW solar

cells to investigate its potential in photovoltaic application in Chapter 6. For all growth, gas-source MBE (GSMBE) is employed.

Chapter 2 describes our GSMBE modified to handle gas source (PH_3 and AsH_3) and a N plasma source. In addition, several techniques used for material characterization including photoluminescence (PL), current density-voltage (J-V), scanning electron microscopy (SEM), transmission electron microscopy (TEM), micro-photoluminescience, and Raman spectroscopies are described.

Chapter 3 reports on epitaxial growth of dilute nitride GaNAsP nanowires (NWs) and GaAsP/ GaNAsP core–shell nanowires on Si (111) by a self-catalyzed method. Growth windows and structural properties are investigated. The structural properties are characterized using SEM. Different sizes of GaNAsP NWs were observed with various N content. A growth model explains the observed diameters of GaAsP/GaNAsP core–shell NWs.

Chapter 4 demonstrates optical characterization of GaAsP, GaNAsP, and GaAsP/GaNAsP NWs. A variety of optical characterizations techniques are used to study the optical properties of these materials, especially the effect incorporating a small amount of nitrogen in the traditional III-V semiconductor system. In this chapter, optical properties are characterized using photoluminescence (PL), cathodoluminescence (CL), electronic dispersive x-ray (EDX) and Raman spectroscopy.

Chapter 5 is devoted to the epitaxial growth of GaAs/GaNAs core-shell nanowires (NWs) on patterned Si (111) by self-catalyzed method using GSMBE. The

growth conditions of GaAs NWs on patterned Si substrate are investigated. The optimized substrate temperature and diluted HF etching time are investigated to have the highest yield of the NWs. Optical properties are studied using micro-PL and Raman spectroscopy. Transmission electron microscopy (TEM) is used to study the crystal structure and defects in the NWs.

Chapter 6 presents the fabrication of single NW solar cells, including the process to create metal contact markers, the reactive ion etching (RIE) process to expose the core of NWs, the wet etch technique to smooth the rough sidewalls of NWs, and metal contact lines to connect a NW with measurement circuits.

Chapter 7 discusses possible future work.

Reference

[1] K. L. Chopra, P. D. Paulson, V. Dutta, Prog. Photovolt: Res Appl. 69, (2004)

[2] Ohl Rs. Light sensitive electric device. US patent 240252, filed 27 March 1941. Light-sensitive electric device including silicon. US patent 2443542, filed 27 May 1941.

[3] M. A. Green, Y. Hishikawa, E. D. Dunlop, D. H. Levi, J. Hohl-Ebinger, A. W. Y. Ho-Baillie, Prog. Photovolt: Res Appl, 26, 3 (2018)

[4] J. F. Geisz, J. M. Olson, and D. J. Friedman. Toward a Monolithic Lattice-Matched III-V on Silicon Tandem Solar Cell. United States: N. p., 2004. Web.

[5] S. R. Kurtz, P. Faine, and J. M. Olson, J. Appl. Phys. 68, 1890 (1990)

[6] G.E. Cirlin, V.G. Dubrovskii, Yu. B. Samsonenko, A. D. Bouravleuv, K. Durose, Y. Y. Proskuryakov, Budhikar Mendes, L. Bowen, M. A. Kaliteevski, R. A. Abram, and Dagou Zeze. Physs. Res. B 82, 035302 (2010)

[7] S. A. Dayeh, C. Soci, X. Bao, and D. Wang, Nano Today 4, 347 (2009).

[8] K. Tomioka, P. Mohan, J. Noborisaka, S. Hara, J. Motohisa, and T. Fukui, J. Cryst. Growth 298, 644 (2007).

[9] F. Glas, Phys. Rev. B 74, 121302 (2006).

[10] L. C. Chuang, M. Moewe, C. Chase, N. P. Kobayashi, C. Chang-Hasnain, and S. Crankshaw, Appl. Phys. Lett. 90, 043115 (2007).

[11]Y. Araki, M. Yamaguchi, and F. Ishikawa, Nanotechnology 24, 065601 (2013).

[12]N. Ahn, Y. Akari, M. Kondow, M. Yamaguchi, and F. Ishikawa, Jpn. J. Appl. Phys. 53, 065001 (2014).

[13]S. L. Chen, S. Filippov, F. Ishikawa, W. M. Chen and I. A. Buyanova, Appl. Phys. Lett. 105, 253106 (2014).

[14]J. E. Stehr, S. L. Chen, M. Jansson, F. Ishikawa, W. M. Chen, and I. A. Buyanova, Appl. Phys. Lett. 109, 203103 (2016).

[15]S. Chen, M. Jansson, S Filippov, F. Ishikawa, W. M. Chen and I. A. Buyanova, J. Vac, Sci. Technol. B 34, 04J104 (2016).

[16]P. K. Kasanaboina, E. Ahmad, J. Li, C. L. Reynolds, Jr., Y. Liu, and S. Iyer, Appl. Phys. Lett. 107, 103111 (2015).

[17] M. D. Kelzenberg, S. W. Boettcher, J. A. Petykiewicz, D. B. Turner-Evans, M. C. Putnam, E. L. Warren, J. M. Spurgeon, R. M. Briggs, N. S. Lewis, H. A. Atwater, Nat. Mater. 9, 239 (2010).

[18]H. P. Xin, C. W. Tu, Y. Zhang, and A. Mascarenhas, Appl. Phys. Lett. 76, 1267 (2000).
[19]K. M. Yu, W. Walukiewicz, J. W. Ager III, D. Bour, R. Farshchi, O. D. Dubon, S. X. Li, I. D. Shart, and E. E. Haller, Appl. Phys. Lett. 88, 092110 (2006).

[20]R. Kudrawiec, A.V. Luce, M. Gladysiewicz, M. Ting, Y. J. Kuang, C. W. Tu, O. D. Dubon, K. M. Yu, and W. Walukiewicz, Phys. Rev. Applied 1. 034007 (2014).

[21]M. Kondow, K. Uomi, A. Niwa, T. Kitatani, S. Watahiki, and Y. Yazawa, Jpn. J. Appl. Phys. Part 1 35, 1273 (1996).

[22]Y. J. Kuang, S. Chen, H. Li, S. K. Sinha, and C. W. Tu, J. Vac. Sci. Technol. B 30, 02B121 (2012).

[23] J. Wu, W. Shan, and W. Walukiewicz. Semicond. Sci. Technol. 17, 860 (2002).

[24] S. Chen, M. Jansson, J. E. Stehr, Y. Huang, F. Ishikawa, W. M. Chen, and I. A. Buyanova, Nano Lett. 17, 1775 (2017).

[25] I. A. Buyanova, G. Pozina, J. P. Bergman, W. M. Chen, H. P. Xin, and C. W. Tu. Time- resolved studies of photoluminescence in GaNP alloys: Evidence for indirect-direct band gap crossover. Applied Physics Letters, 81(1), 2002.

[26] S. Sukrittanon, Y. J. Kuang, C. W. Tu, J. Vac. Sci, Technol. *B*, 31, 03C110 (2013).
[27] W. G. Bi and C. W. Tu. Appl. Phys. Lett. 69, 24 (1996).

[28] S. Sukrittanon, Y. J. Kuang, A. Dobrovolsky, W. M. Kang, J. S. Jang, B. J. Kim, W. M. Chen, I. A. Buyanova, C. W. Tu, Appl. Phys. Lett., 105, 072107 (2014).

Chapter 2

Experiment Procedures

2.1 Overview

Molecular Beam Epitaxy (MBE) was invented in the late 1960s at AT&T Bell Labs by Cho and Arthur[1]. It has been widely used as an advanced technique to grow high-quality semiconductor thin films for fundamental scientific studies and various applications. The high purity of thin films grown by MBE is attributed to its advanced ultra-high vacuum (UHV) evaporation system. Besides the UHV growth chamber, a typical MBE machine contains effusion cells for material sources, shutters, a substrate holder/heater, vacuum gauges, and pumps to achieve UHV environment (cryogenic

pumps, turbo pumps, ion pumps and liquid nitrogen cryo-shroud, etc).

The samples grown in our gas-source MBE (GSMBE) were characterized with photoluminescence (PL), transmission electron microscope (TEM), scanning electron microscope (SEM), and X-ray diffraction (XRD). This chapter describes our GSMBE system and some of the characterization techniques.

2.2 Growth

2.2.1 Gas-source molecular beam epitaxy

The GSMBE reactor used in this thesis is a custom-assembled Varian Gen-II MBE system with AsH_3 and PH_3 as group-V sources. Two separate gas cabinets for AsH_3 (100%) and PH_3 (100%) were installed in the lab. A Pfeiffer TMU 1600 model turbomolecular pump with a pumping speed of 1500 l/s is mounted on the growth chamber and the exhaust goes to a potassium permanganate ($KMnO_4$) scrubber. The advantages of using GSMBE include reduction of chamber opening frequency to replace the AsH_3 and PH_3 sources and the ability to change the flux and type of group-V source rapidly.

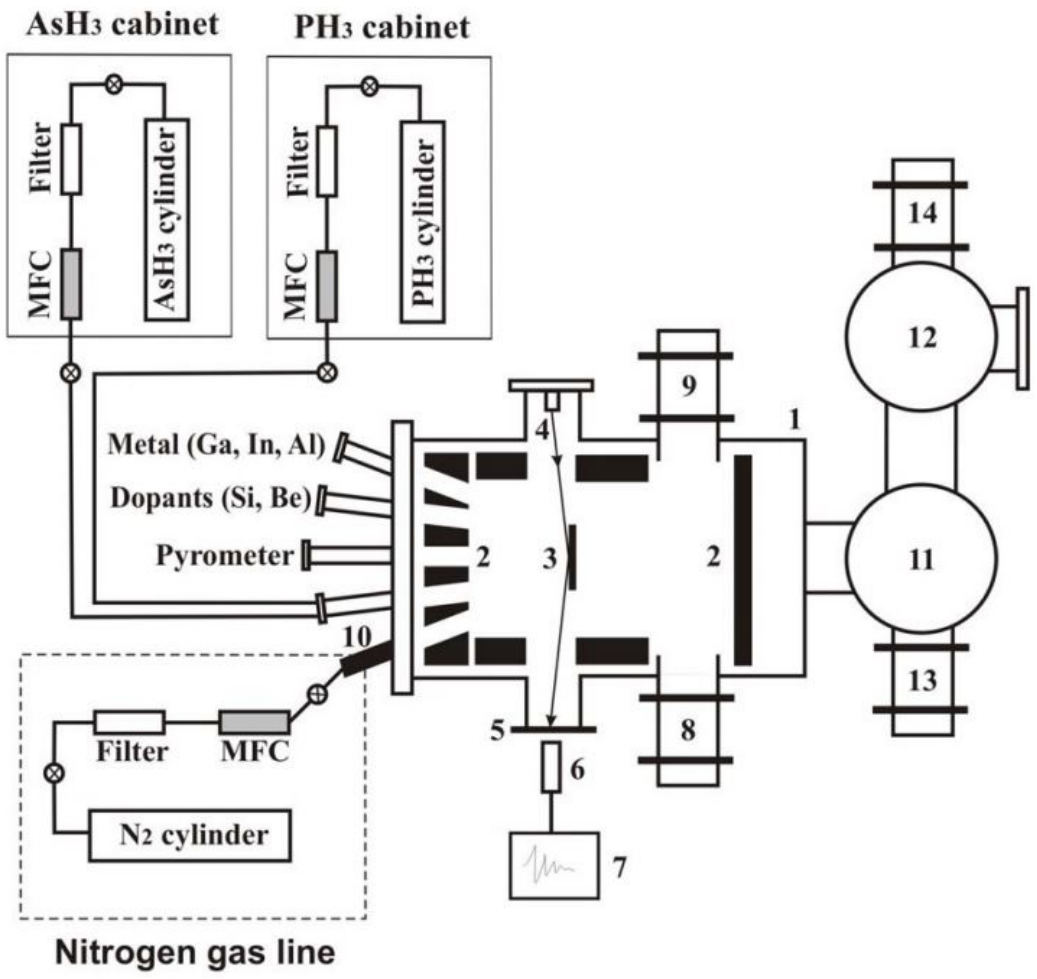

Figure 2.1. Schematics of the modified Varian Gen-II gas-source molecular beam epitaxy[11]

Besides the two group-V sources, solid elemental Ga, In and, Al are used as group-III sources. Si and Be are used as n-type and p-type dopant source, respectively. All of these solid-source-materials are filled in the crucibles mounted on the top of Knudsen effusion cells. Their fluxes are generated and controlled by temperature. The AsH_3 and PH_3 flow rates are controlled by mass flow controllers (MFCs). After injected

from the cabinets to the front panel, the group-V gases are thermally cracked at 1000 °C by cracker cells into As_2, P_2 and H_2. The full scale of AsH_3 and PH_3 by the MFC is 5 sccm and 20 sccm, respectively. Usually, we set the arsine and phosphine flow in the range of 0.5-2 sccm and 4-6 sccm, respectively. In front of the cells are pneumatic shutters which can be controlled both manually and automatically from a computer. The shutter open and close frequency and interval can be programmed.

The pumping system includes a Pfeiffer TMU 1600 turbomolecular pump with a pumping speed of 1500 l/s in the growth chamber, an Agilent Vacion ion pump with a pumping speed of 60 l/s in the buffer chamber and a small dry pump in the load-lock chamber. A liquid nitrogen shroud is in the growth chamber surrounding the effusion cells to condense background residual gases and reduce contamination during growth. Typical growth chamber pressure is in the mid-10^{-9} Torr with liquid nitrogen and effusion cells heated to operating temperature. The pressure will increase to low-10^{-5} with a range of group-V flux < 5 sccm during growth.

2.2.2 N plasma source

In order to incorporate dilute N into our samples, a radio-frequency (RF) plasma N source is mounted in one of the furnace ports. The model we used is the Oxford Applied Research model MPD21 RF nitrogen plasma source with the features of electrode-free to avoid contamination, UHV-compatible for operation at pressure <10^{-5} Torr and a wide range of beam flux of 0-5 sccm with a step of 0.005 sccm (controlled by

MFC). The N plasma is generated in the following steps. First, ultra-high purity (99.99%) N_2 gas passes a regulator, which control the pressure at around 50 psi. Then, the water vapor and oxygen are removed by sending the N_2 through a purifier (Matheson Gases & Equipment, 6190-V4MM Membrane Type) to remove water vapor and oxygen. Next, N_2 gas goes through an MFC and, finally, the RF plasma source, where nitrogen radicals are generated and escape into the growth chamber through a beam exit aperture, which has 16 holes with a diameter of 0.3 mm. The shutter in front of the N furnace port cuts off the N radical beam when no N is required.

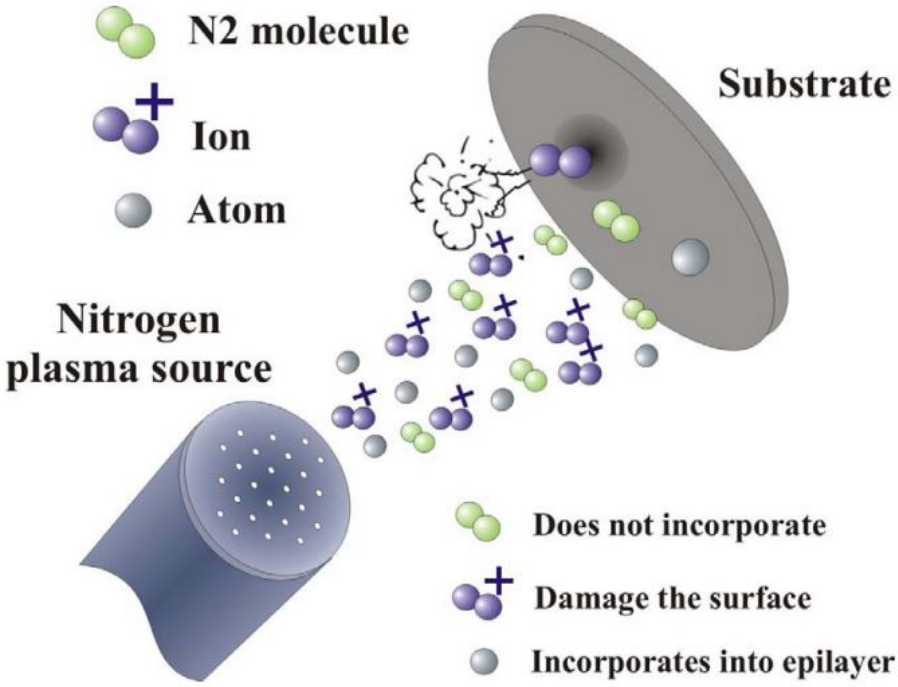

Figure 2.2. Schematic of the N plasma source and N species produced by plasma discharge[5]

The N plasma source is discharged from inductively-coupled RF excitation at 13.56 MHz inside a pyrolytic boron nitride (PBN) tube. Schematic plot of the N plasma source and species produced by plasma is shown in Figure 2.2. Several species of

particles are created during the RF excitation step including[3] 1. Atomic nitrogen converted from molecular nitrogen because their bonds are broken in the plasma discharge. These radicles are desired in the growth; 2. N molecules whose bonds are not fully broken by the RF field and do not participate in the growth. 3. N ions, which do not participate in the growth but will damage the sample surface with ion bombardment. In order to reduce the damage from N ions, the shutter in front of the plasma source is usually closed when the nitride is not needed. A manual valve is also installed between the MFC and the gas inlet of the N plasma source to isolate N_2 at the idle state.

There are two key parameters to adjust in order to get desired N plasma composition and the rate of plasma discharge, RF power (0-300 Watts) and N_2 flux (0-3 sccm). We tune these two factors and then observe the plasma discharge's optical emission intensity, which is monitored using a Si photodetector in our system to evaluate the discharged plasma. The amount of the desired radicle of nitrogen is proportional to the optical emission intensity of nitrogen plasma source. The plot of the relationship between RF plasma, N_2 flux, and optical emission intensity is shown in Figure 2.3. The experimental data are summarized by previous group members. From the plot, we can see that increasing plasma power or nitrogen flux can increase the plasma intensity, thus an increase of nitrogen incorporation into the growing film. The solid line in Figure 2.3 borders the linear region where the plasma intensity is proportional to the nitrogen flux. The black curves out of the red solid line area show that the intensity is close to saturation, which means that an excessive nitrogen flux and high plasma power will

create a lot of undesired ions, which will damage to the surface. To sum up, the optimal nitrogen plasma conditions are that area in the lower left corner of Figure 2.3, which provides a low-pressure growth environment and a maximum plasma efficiency.

2.3 Reflection high-energy electron diffraction

Reflection high-energy electron diffraction (RHEED) is an in-situ characterization technique to monitor the surface condition during growth. A complete RHEED composees of an electron gun and a photoluminescent detector screen[2]. The high-energy electrons generated by the electron gun strike a sample at a very small angle relative to the sample surface and a small fraction of the refracted electrons interfere constructively at specific angles and construct a reciprocal space map of the sample on the phosphorous screen. The different surface reconstruction patterns indicate different structures. The following discussion is about how we use RHEED to calibrate the growth rate.

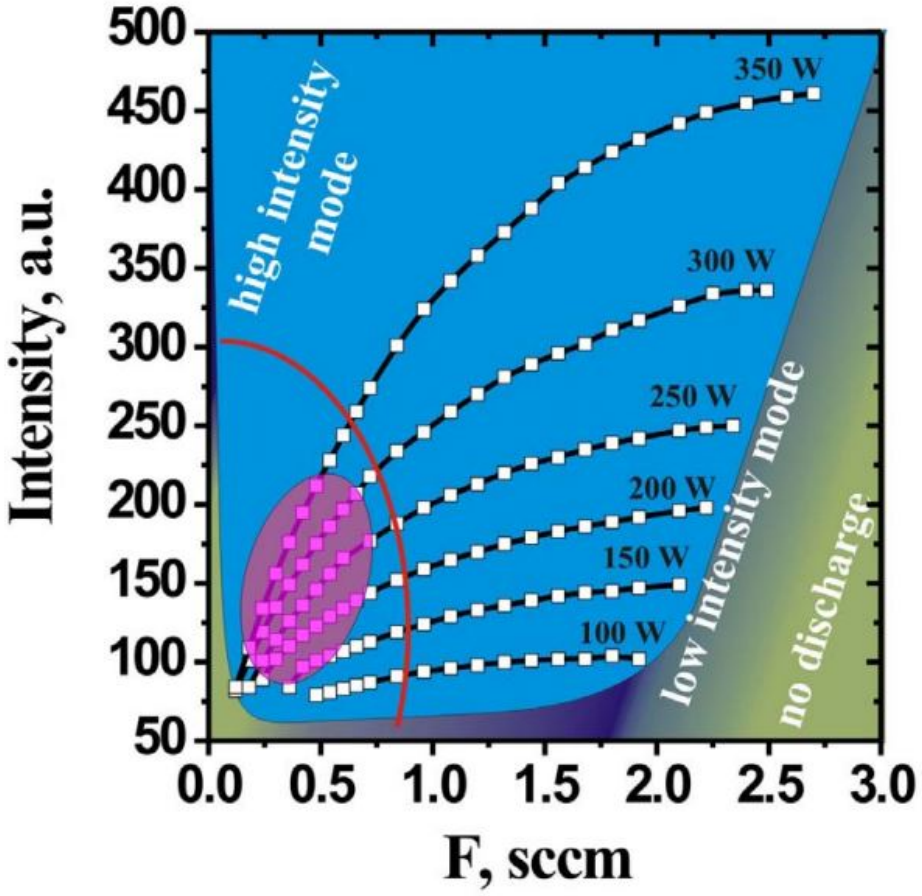

Figure 2.3. The relationship between the plasma intensity and the N2 flux at a given applied RF power[5].

Figure 2.4 shows the RHEED intensity measurement during a GaP MBE growth at 670 °C. The top binary signal indicates on-off states of Ga and P shutters. After a buffer layer growth, the group-III shutter is re-opened. In the presence of a Ga flux, the oscillation in time indicates layer-by-layer growth. The oscillation period can be used to calculate the beam flux to precisely control the growth rate, alloy composition, and layer thickness. The same method is used to calculate P and As growth rate. The V/III ratio discussed in this thesis is calculated with the equation of:

$$r = \frac{R_V}{R_{III}} \tag{2,1}$$

Where r is the V/III ratio, R_V, R_{III} are the growth rates of group-V and group-III materials, respectively.

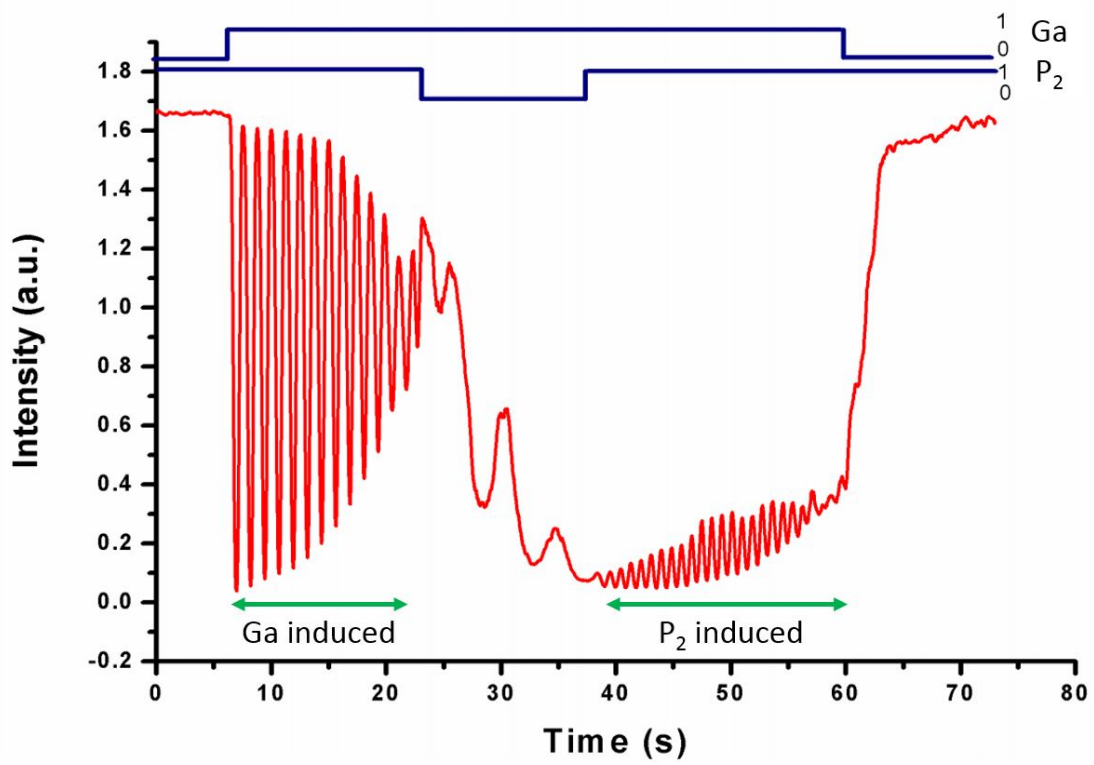

Figure 2.4.The RHEED oscillation triggered by Ga and P_2.(Adapted from Y. J. Kuang's Ph.D. thesis, UCSD, 2014). The binary signals indicate on-off state of Ga and P_2 shutters.

2.4 Characterization

2.4.1 Photoluminescence

Photoluminescence (PL) is a technique to characterize the optical and electronic properties of semiconductor materials. The sample is excited with a light source that provides photons with energy larger than the semiconductor bandgap. Once the photons are absorbed, electrons and holes pairs are formed, which then recombine with the

emission of photons. The advantage of PL measurement is that it's non-destructive and can be combined with microscopy, to map the lifetime of the photoluminescence of a sample. Figure 2.5 shows the set up of our PL system. In this study, a 532 nm semiconductor laser is used as the optical source in the PL system. The laser beam first goes through a chopper, which eliminates noise signal from ambient light. Then the beam hit the sample and excites the emission of the photons. The light emission is dispersed by wavelength inside a SPEX 1870 monochromator and detected by a Hamamatsu R636-10 photomultiplier tube (PMT). The photonic signal can be collected and recorded by a computer connected to the PMT detector. For low-temperature measurement, the sample is mounted on a cold finger and enclosed in a cryostat.

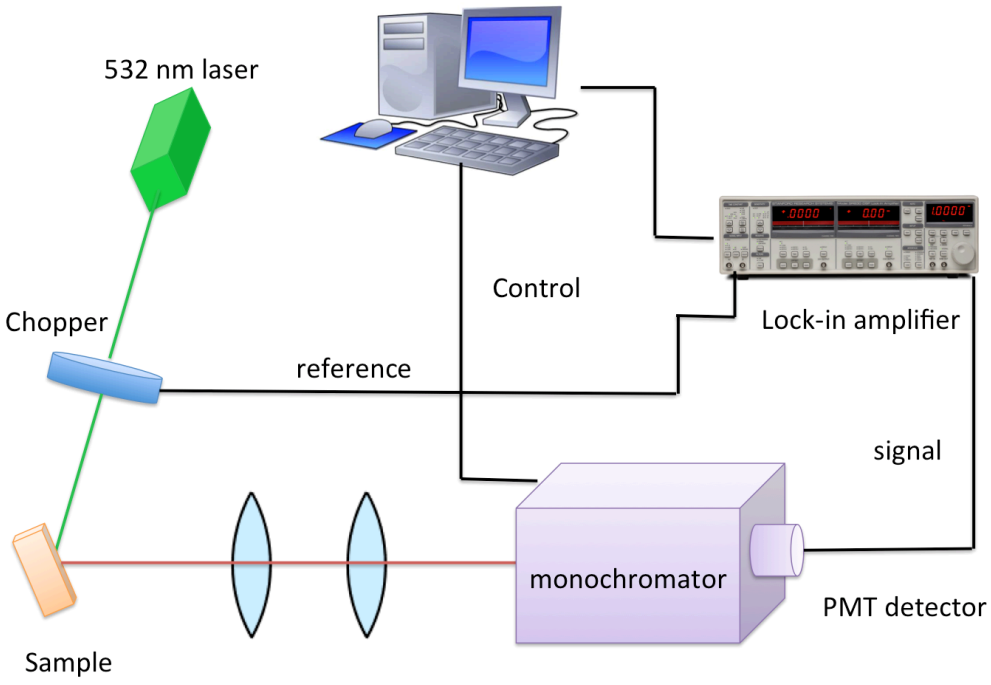

Figure 2.5 Schematic of the PL setup

2.4.2 Scanning Electron Microscope

Scanning electron microscope (SEM) is a type of electron microscope that produces images of a sample by scanning the surface with a focused beam of electrons. SEM can provide information on surface topography, crystalline structure and chemical composition. In an SEM the incident electrons typically have energies of 2-40 keV. There are three types of electron gun in general[4], 1: Tungsten hairpin flament which is heated to over 2500 °C to produce thermal emission of electrons from the tip. 2: Lanthanum hexaboride (LaB_6) filaments also work by thermionic emission. 3: Field emission guns provide the brightest beam with very small deviations in electron energy by applying a very high electric field to a finely pointed tip until quantum mechanical tunneling of electrons occurs. The SEM images shown in this dissertation are all acquired by field emission guns. A schematic representation of the SEM components is shown in Figure 2.6. Electromagnetic lenses are used to control the path of the electrons. The condenser defines the size of the electron beam, while the objective lens focus the beam on the sample. The brand of SEM used in this thesis is FEI Quanta 250 SEM.

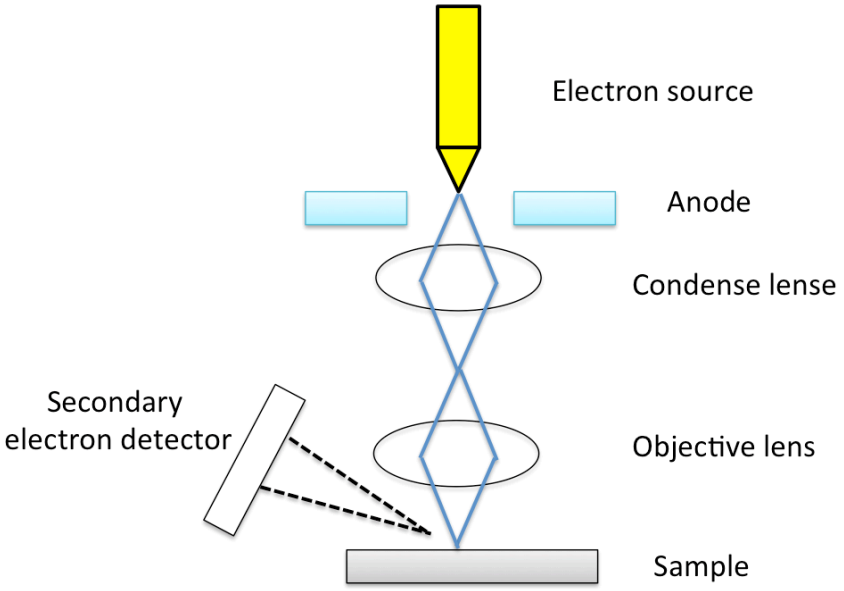

Figure 2.6 Schematic representation of the basic SEM components.[6]

2.4.3 Other characterization techniques

In this dissertation, optical properties were also characterized using photoluminescence excitation (PLE) and micro-Raman (μ-Raman) spectroscopies in our collaborator's lab in Linköping University. PLE is obtained by monitoring emission at a fixed wavelength while varying the excitation wavelength. A sample's excitation spectrum is nearly identical to its absorbance spectrum. The excitation spectrum provides a convenient means for measuring bandgap of materials. Figure 2.6 shows schematic plot of PLE components. A narrow band of wavelengths selected by the pump monochromator is incident on the sample and excites photoluminescence. The PLE signal is detected using a photomultiplier with a filter monochromator. In this study, PLE measurements were performed with a tunable Ti:sapphire laser as an excitation source. Transient photoluminescence studies were done at room temperature for NW arrays,

excited by a frequency-doubled pulsed Ti:sapphire laser at 440 nm with a pulse width of 2 ps.

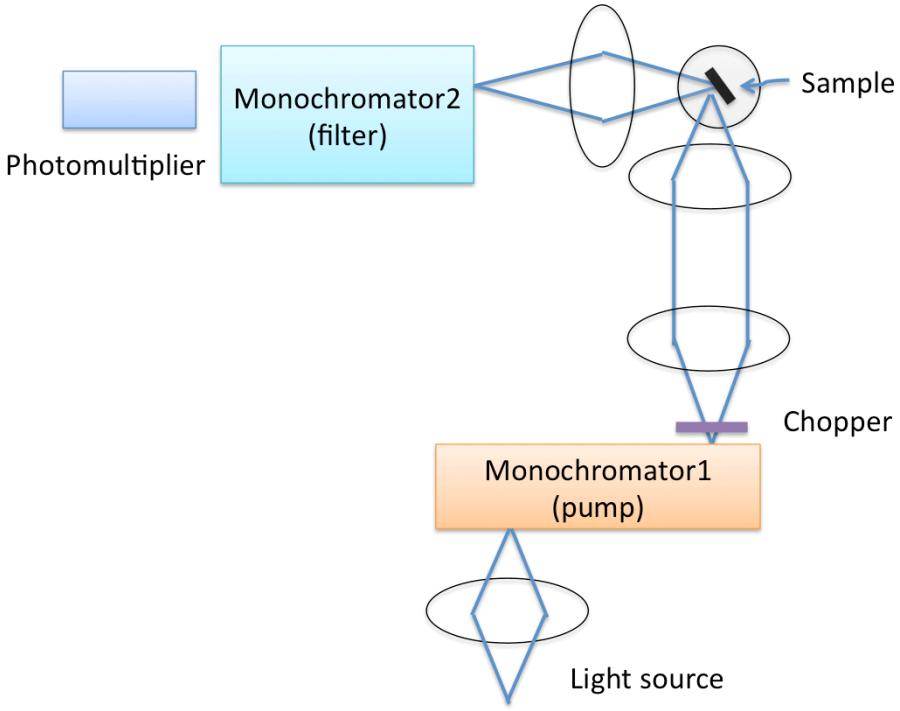

Figure 2.6 Schematic representation of PLE components.[7]

μ-Raman spectroscopy has emerged as a powerful noninvasive tool for probing the vibrational properties of nanostructures on substrates compatible with typical three terminal electronic devices.[8] Polarized Raman spectroscopy is commonly used to characterize crystal structure and stacking faults in NWs.[9] In this dissertation, μ-Raman spectra are acquired at room temperature from NW arrays using a 659 nm solid state laser as an excitation source. The spectra are measured in the back-scattering geometry and the excitation beam is focused on the sample using a 100X objective (NA = 0.9). The excitation power is 2.2 mW. The signal is dispersed using a monochromator equipped with an 1800 mm^{-1} grating and detected with a Peltier cooled Si CCD camera.

Transmission electron microscope (TEM) is a microscope technique to study the growth of materials, their composition and defects like dislocations and grain boundaries. Our TEM work is performed on a FEI Tecnai F30 300kV TEM. Also, High Resolution TEM (HRTEM) is used to illustrate the strain and twinning planes of NWs. Figure 2.7 shows configuration of electron beam direction in TEM. In the plot, the atomic planes are oriented parallel to the incident electron beam in the microscope. This orientation produces a strong transmitted beam and a multitude of diffracted beams for the different sets of atomic planes that are parallel to the incident beam. The multitude of beams diffracted from the planes parallel to the incident beam are collected with a large objective aperture in the microscope and it is the interference of these beams that generates an image which is a reconstruction of the crystal lattice.[10] To prepare the samples for TEM, in-situ focused ion beam (FIB) is used to slice NW apart from Si substrate. The samples are then mounted to a TEM grid for operation.

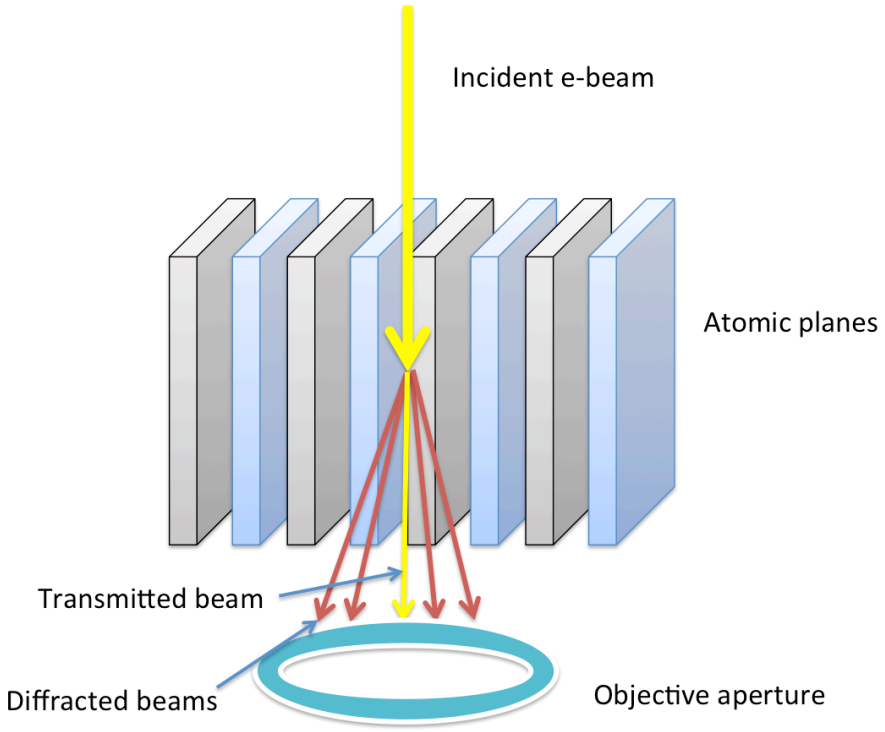

Figure 2.7 High-resolution TEM imaging configuration[10].

Reference

[1] J. R. Arthur. Molecular beam epitaxy. Surface Science, 500(1-3):189–217, 2002.

[2] M. B. Panish and H. Temkin. Gas-source molecular-beam epitaxy. Annual Review of Materials Science, 19:209–229, 1989.

[3] R. P. Vaudo, Z. Yu, J. W. Cook, Jr., and J. F. Schetzina, Optics Lett., 18, 1843 (1993)

[4] K. D. Vernon-Parry, III-Vs Review, 13, 41 (2000).

[5] Vladimir Odnoblyudov, 2006, "Gas-Source Molecular Beam Epitaxial Growth and Characterization of the (Al, In, Ga)NP/GaP Material System and its Application to Light-Emitting Diodes", Doctor of Philosophy thesis, University of California San Diego.

[6] D. McMullan. Scanning Microsc, 17, 175 (1995).

[7] A. M. White, E. W. Williams, P. Porteous, and C. Hilsum, J. Phys. D: Appl. Phys, 3,

1322 (1970).

[8] R. Tanta, C. Lindberg, S. Lehmann, J. Bolinsson, M. R. Corro-Temboury, K. A. Dick, T. Vosch, T. S. Jespersen, and J. Nygard, Phys. Rev. B 96, 165433 (2017).

[9] F. J. Lopez, E. R. Hemesath, and L. J. Lauhon, Nano Lett. 9, 2774 (2009).

[10.] T. Gugov, 2005, "Transmission Electron Microscopy Characterization of Long Wavelength Dilute Nitrides", Doctor of Philosophy thesis, Stanford University.

[11] W. Bi, 1997, "Nitrogen-containning mixed group-V compounds grown by gas-source molecular beam epitaxy using a nitrogen radical beam source", Doctor of Philosophy thesis, University of California San Diego.

Chapter 3

The Growth of GaAsP/GaNAsP NWs on Si substrate

3.1 Overview

This chapter is focused on the epitaxial growth of dilute nitride GaNAsP nanowires (NWs) and GaAsP/GaNAsP core-shell NWs on Si (111) by a self-catalyzed method. The III-V semiconductor NWs grown on Si substrate is very promising in the application of solar cells due to their superior properties of III-V materials and the low cost of Si.[1-4] With respect to thin film solar cell, a core/shell nanowire configuration solar

cell provides several advantages, which are: (1) greater light absorption, [5,6] and (2) enhanced carriers collection because of decoupling the requirements for light absorption and carrier extraction.[7]

This chapter is devoted to the study of self-catalyzed GaAsP, GaNAsP and GaAsP/GaNAsP NWs growth on Si (111) substrate. First, the optimized growth temperature and V/III ratio of GaAsP NWs are investigated. Then the N effect on the GaNAsP NWs is reported. The structural properties are characterized using scanning electron microscopy (SEM). Last, the lateral growth rate of GaAsP/GaNAsP core-shell NWs is studied and a model is built to simulate the shell growth rate based on several growth parameters.

3.2 GaAsP NWs

3.2.1 Growth

The GaAsP NWs growth is the first step towards the growth of GaAsP/GaNAsP core/shell structure. The samples grown on Si (111) substrate. The growth window of these III-V NWs ranges from ~600 to ~650 °C. Prior to growth, the Si (111) substrate is dipped in an HF solution at room temperature for 5 seconds to remove the intrinsic oxide, and then rinsed with deionized water. The substrate was then placed into the growth chamber and heated to 710 °C for 15 min, and then, T_{sub} was decreased to the growth temperature.

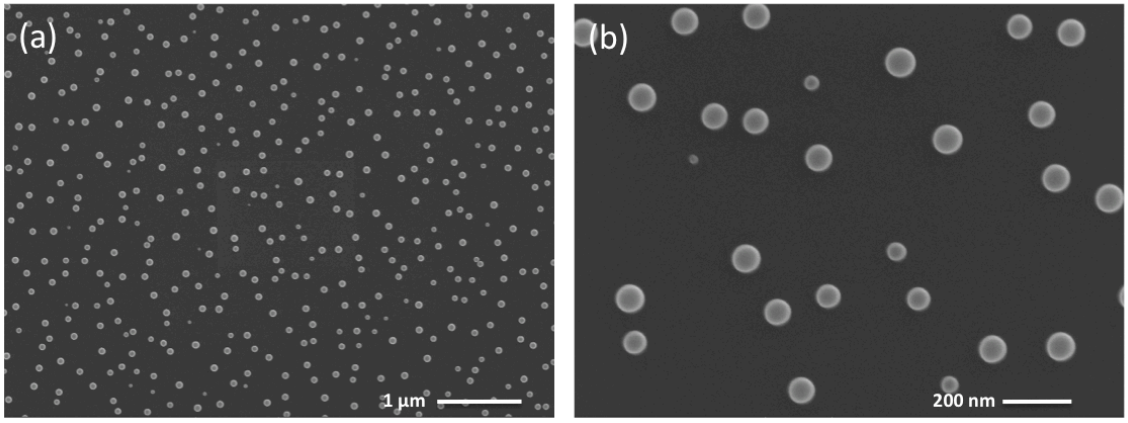

Figure 3.1: Ga droplets as catalysts on Si (111)

For NW growth, Ga atoms were deposited on the Si (111) surface for 1 min with a Ga flux of ~ 0.7 monolayer/s, calibrated by Ga-induce reflection high-energy electron diffraction (RHEED) intensity oscillation for the planar growth of GaP under the same substrate temperature (T_{sub}). Then, the substrate was annealed for 30 s to form Ga droplets on the surface. Ga nsnowire growth lasts 20 minutes under a V/III incorporation ratio of 2.5 and a substrate rotation speed of 8 RPM.

3.2.2 Growth Temperature

The vapor-liquid-solid (VLS) growth mechanism, suggested by Wagner in 1964[8], has been widely used to explain the growth of NWs as shown in Figure 3.2. In this mechanism, the NWs absorb vapor atoms on the catalyst Ga droplets and then grow with solidification of liquid alloy under the droplets. Eventually, the diameters of the grown NWs are determined by the size of the droplets. The minimum radius[9] of a liquid droplet is defined as

$$R_{min} = \frac{2\sigma_{VL}V_L}{RT_{sub}ln\sigma} \quad (3.1)$$

where σ_{VL} is the liquid-vapor surface free energy, V_L is the molar volumn, and σ is the vapor phase supersaturation. High temperature will result in a small radius of droplets and in turn, yield NWs with a small diameter.

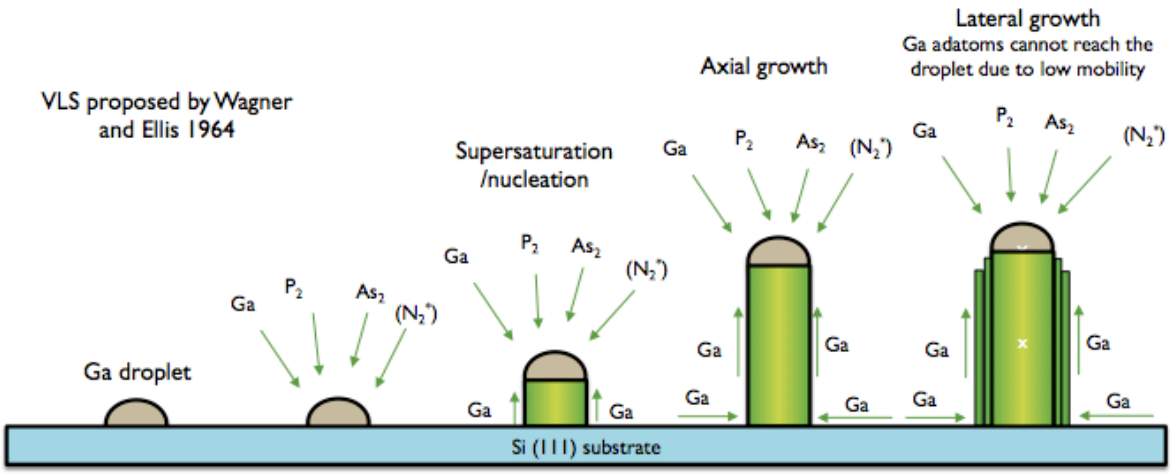

Figure 3.2 Schematic showing the VLS growth of Ga(N)AsP/GaNAsP core/shell NWs.[8]

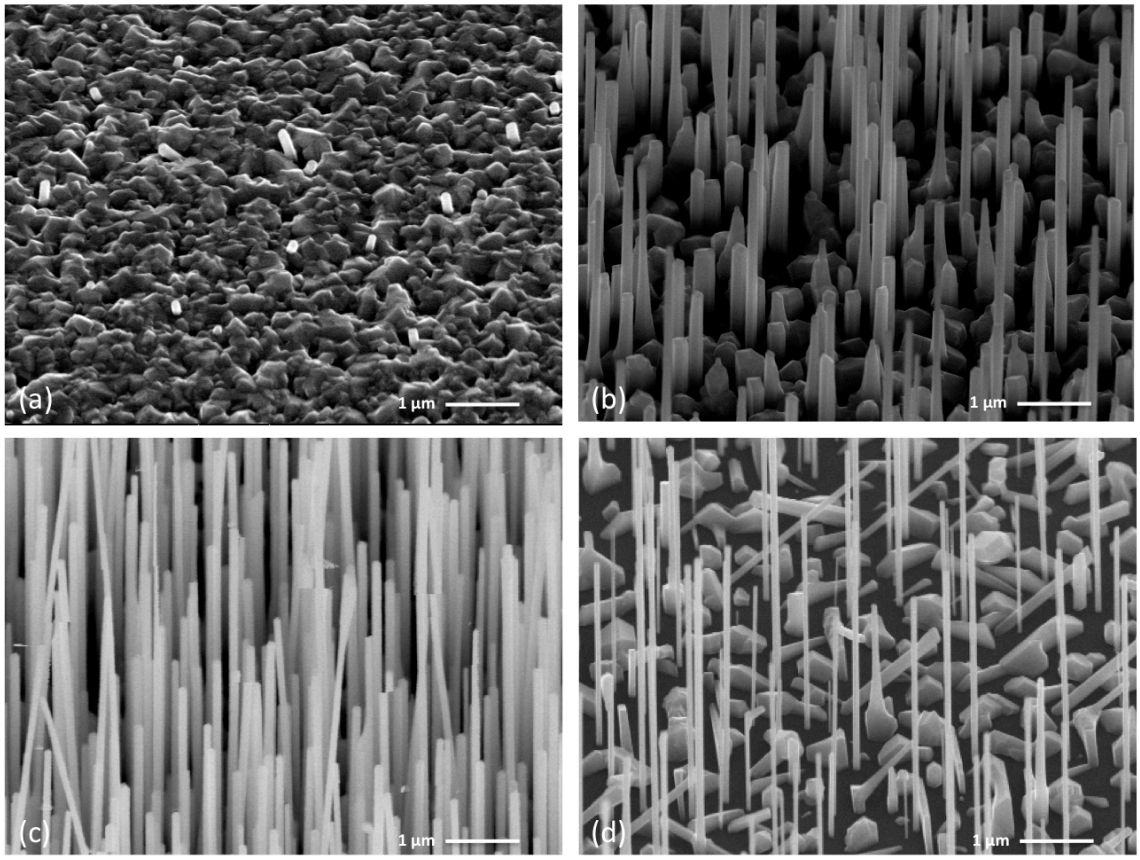

Figure 3.3: SEM images of GaAsP NWs on Si (111): GaAsP NWs grown with T_{sub} of (a) 550°C, (b) 600 °C (c) 650 °C, (d) 700 °C. The scale in each photograph is $1\mu m$

Figure 3.3 shows SEM images of GaAsP NWs grown at various substrate temperatures. The growth windows and the temperature-dependent structural characteristics of GaAsP NWs are studied by observing performance of NWs under 550°C, 600 °C, 650 °C, and 700 °C which corresponds to the sample name GaAsP-550, GaAsP-600, GaAsP-650, and GaAsP-700, respectively.

Table 3.1: The average diameters and length of NWs grown at different temperature

T_{sub} (°C)	Diameter (nm)	Length ($\boldsymbol{\mu m}$)
GaAsP-550	-	-
GaAsP-600	123 $\pm$ 21	1.5 $\pm$ 0.7
GaAsP-650	87 $\pm$ 9	2.8 $\pm$ 0.4
GaAsP-700	73 $\pm$ 5	2.8 $\pm$ 0.5

The diameters and lengths of GaAsP NWs are depicted in Table 3.1. At higher T_{sub}, the average diameter of our grown NWs becomes smaller, which is inline with Equation 3.1. We can also see highest NWs density is at T_{sub} equals to 650 °C. In the vapor-liquid-solid (VLS) mechanism, liquid droplets act as catalyst and absorb vapor components (both Ga, As and P here) to incorporate into and supersaturate alloy droplets (Ga rich here) and initiate the growth of the reaction byproduct (GaAsP NW) from a supersaturated melt. At 550 °C, Ga adatom mobility is very low. Consequently, most adatoms stay at the surface of Si substrate, which results in GaAsP cluster growth. At high T_{sub} like 650 °C, Ga adatom mobility is increased to have successful vertical growth. At 700 °C, the high temperature drives Ga adatoms to vaporize in the chamber, and therefore, the density of NWs is smaller than that at lower substrate temperature.

3.2.3 V-III ratio in GaAsP NWs growth

The As and P compositions in the NWs were estimated by comparing with a GaAsP thin film grown on GaP substrate under the same conditions. The As and P compositions of the GaAsP thin film were characterized by in situ group-III and group-V-induced RHEED intensity oscillation and Photoluminescence spectra of GaAsP NWs. A typical As and P induced RHEED intensity oscillation is shown in Figure 3.4. After a growth interruption, Ga induced RHEED oscillation was triggered when the Ga shutter was open, from which the Ga growth rate R_{Ga} was obtained. Then the Ga shutter was closed and As, P shutter were open. The group-V induced RHEED oscillation indicates the group-V elements growth rate R_{As+P}. The V-III ratio of GaAsP growth can be expressed as follow,

$$V - III\ ratio = \frac{R_{As+P}}{R_{Ga}} \tag{3.2}$$

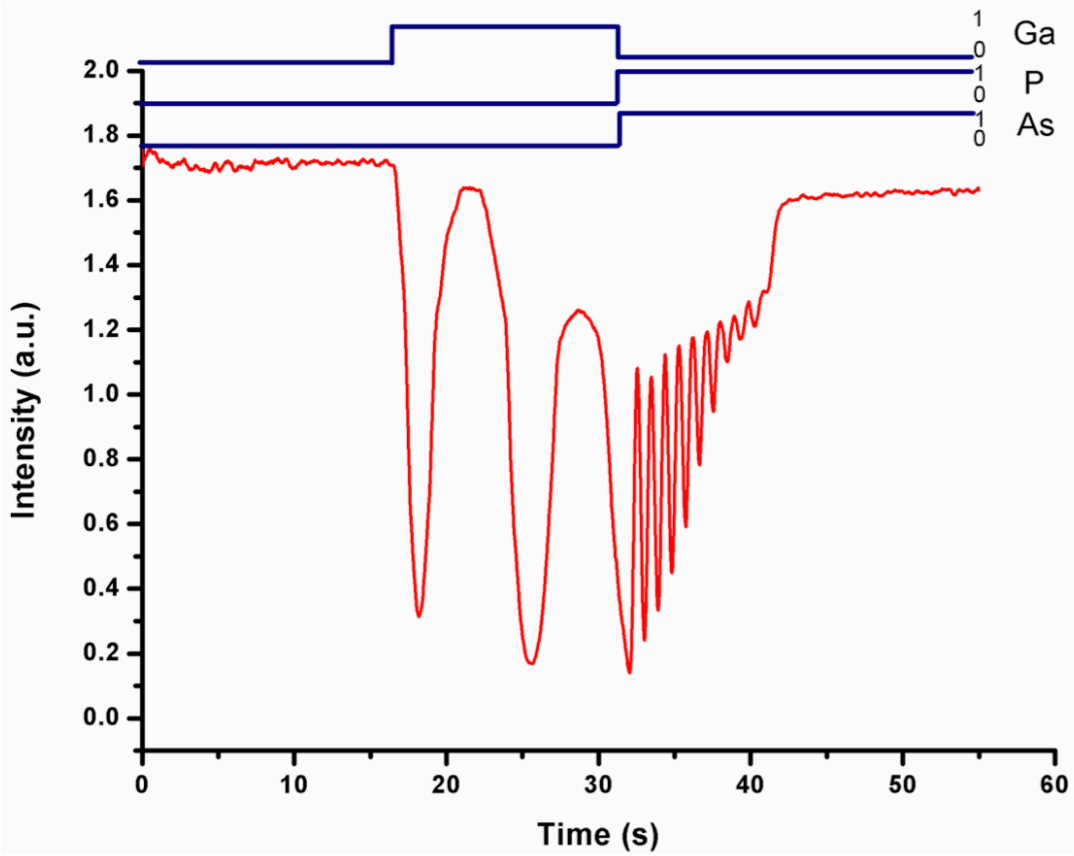

Figure 3.4. As and P induced RHEED intensity oscillation. The time series on top show the status of Ga, As and P shutters, where 0 stands for closed and 1 stands for open. (Adapted from Y. J. Kuang's Ph.D. thesis, UCSD, 2014)

To get a suitable nucleation rate of GaAsP for NW growth, the morphology of GaAsP nanostructures is first studied by varing the V/III ratios from 2 to 10 while keeping a constant group V flux, as shown in Fig 3.5. When the V/III flux ratio is

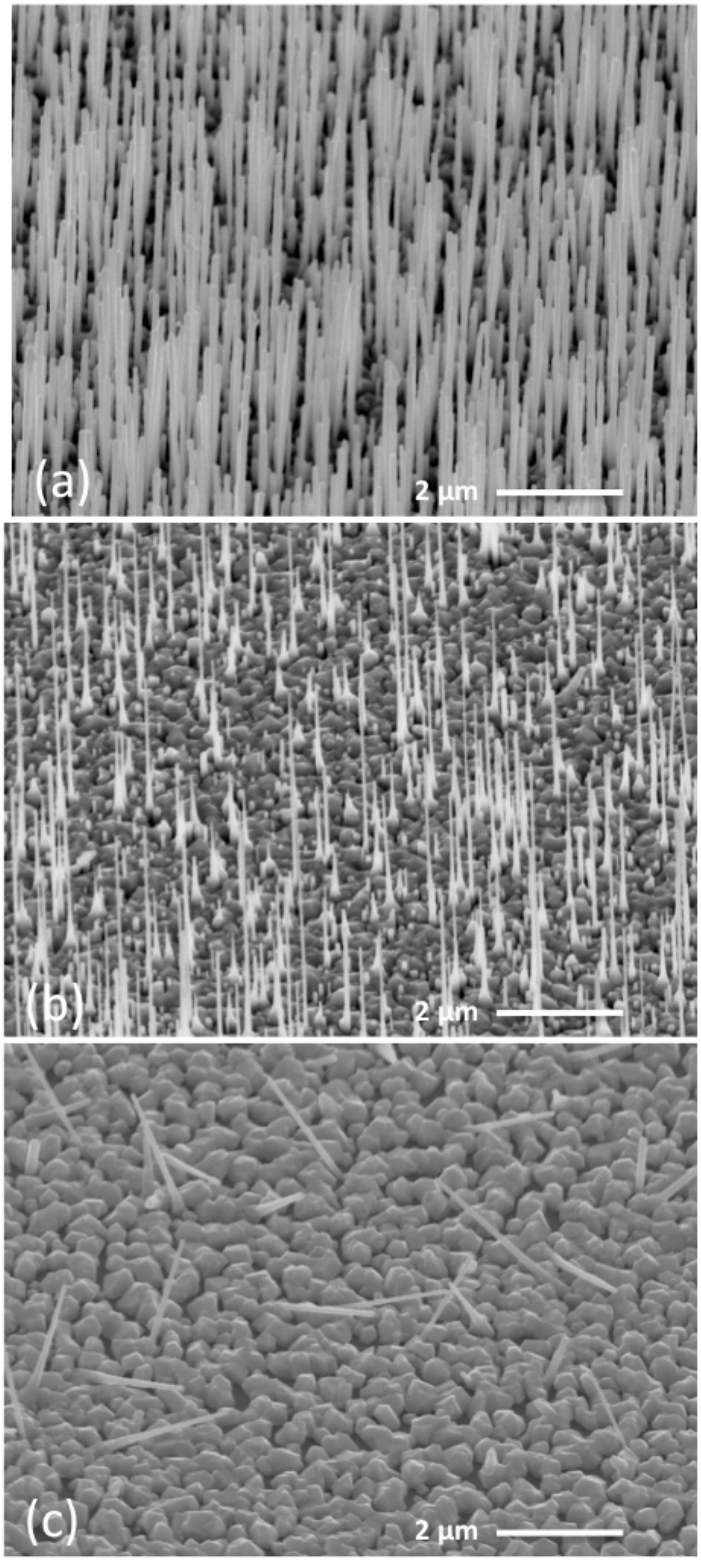

Figure 3.5. SEM image of GaAsP NWs with same P/As flux ratio but different V/III ratios: (a) V/III = 2, (b) V/III = 6, (c) V/III = 10.

2, the diameter is homogeneous over the whole length (Figure 3.5(a)). At this V/III ratio, the replenishment and consumption rate of Ga droplets on the top of NWs reach a dynamic equilibrium so as to maintain a constant Ga droplet size over the nanowire length. When the V/III ratio is increased to 6, most of NWs show a tapered shape, which is caused by the shrinkage of Ga droplets (Figure 3.5(b)). As higher V/III ratio will break the balance between replenishment and consumption of Ga droplets, the size of Ga droplets on the tip of NWs will shrink during growth. Further increasing the V/III ratio to 10, the droplets can only survive on few NWs and the rest droplets are consumed rapidly. As a result, only a few NWs with cone shape have been observed in Figure 3.5 (c).

3.3 GaNAsP NWs

3.3.1 Growth

After GaAsP NWs are successfully grown on Si (111) substrate, the growth condition of GaNAsP NWs was studied to investigate the effect of N injection to the growth and determine N composition in the quaternary alloy. GaNAsP NWs were grown on Si (111) with the similar growth conditions but injecting N plasma in the growth. Before the growth, the Si (111) substrate is prepared the same way as the GaAsP growth, described in section 3.2.1. Then, in the growth chamber, Ga atoms are deposited as catalyst on the Si (111) substrate for 30 seconds with a Ga flux of ~0.7 ML/s, and is annealed for 30 seconds to form Ga droplets. Growth started by opening the Ga shutter

and injecting PH_3 and AsH_3 into the chamber to initiate growth of GaAsP nanowire and then the RF nitrogen plasma was excited at different power (200-250 W) after 60s of GaAsP NWs growth. To ensure uniformity, the substrate is rotated at 5 RPM during growth. To study the effect of N concentrations to the GaNAsP NWs growth, different RF nitrogen plasma power and N flux are adopted. For comparison, the data from GaAsP NWs grown in Section 3.2 are used.

3.3.2 Structural properties and discussion

By first growing the GaAsP NWs seeding roots, GaNAsP can be successfully grown on Si (111) substrate. The SEM images of GaAsP NWs and GaNAsP NWs with vaious N conditions (0.3 sccm, 200W; 0.6 sccm, 220 W; and 0.9 sccm, 250 W) are shown in Figure 3.6. The growth conditions of each NWs sample are summarized in Table 3.2. N0, LN, MN, and HN represent samples with different nitrogen concentrations (zero, low, medium and high [N]). As more N atoms were incorporated, the average diameter of NWs was increased while the average length was decreased. The observed average diameters are 70 $\pm$ 8, 86 $\pm$ 11, 118 $\pm$ 15, and 164 $\pm$ 20 nm for samples N0, LN, MN, and HN. Also, the NW length is shorter at higher plasma RF N incorporation. The average lengths are 2.4 $\pm$ 0.4, 2.0 $\pm$ 0.2, 1.7 $\pm$ 0.3, and 1.2 $\pm$ 0.3 μm for samples N0, LN, MN, and HN, respectively. Generally speaking, introducing impurity N in III-V NWs leads to reduction in the vertical growth and enhancement of sidewall growth. A possible explanation is that during growth with N plasma, the formation of Ga-N bonds

can significantly reduce the mobility of Ga adatoms. Also, Ga adatom diffusion length decreases with increasing number of reactive nitrogen species. Thus, the top Ga droplets will be consumed by plasma nitrogen. With a further increase in the nitrogen flux, the Ga droplets can only survive for a very short time, and the VLS process is terminated at a certain height. After the droplets are fully consumed, the vapor solid epitaxial growth on sidewalls will dominate and the NW diameter will increase. A good example is the growth under the plasma nitrogen conditions of 0.9 sccm and 250 W. NWs of this sample show nonuniform diameter along the whole NW length and exhibits a tapered shape. The latter is caused by the consumption of Ga droplets on the NW sidewalls.

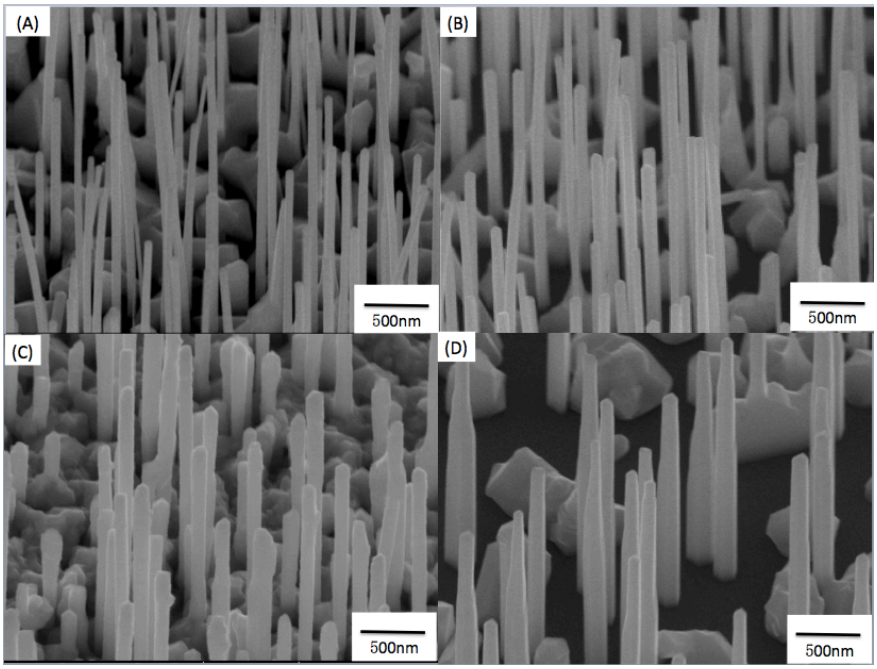

Figure 3.6 SEM images of (a) GaAsP NWs on Si (111), (b) GaNAsP with N growth condition of 0.3 sccm, 200 W, (c) GaNAsP with N growth condition of 0.6 sccm, 225 W, and (d) GaNAsP with N growth condition of 0.9 sccm, 250 W.

Table 3.2. Growth condition, diameter, and length of each NWs sample

Sample	N flux (sccm)	Plasma power (W)	Diameter (nm)	Length ($\boldsymbol{\mu m}$)
GaAsP(N0)	-	-	70 ± 8	2.4 ± 0.4
GaNAsP (LN)	0.3	200	86 ± 11	2.0 ± 0.2
GaNAsP (MN)	0.6	225	122 ± 15	1.7 ± 0.3
GaNAsP (HN)	0.9	250	164 ± 20	1.2 ± 0.3

3.4 GaAsP/GaNAsP core/shell NWs

3.4.1 Growth

To have highest NWs density, we used the growth condition of GaAsP-650 to growth the GaAsP core in GaAsP/GaNAsP core/shell NWs. The GaAsP core were grown using the procedure described above, and subsequently, for the shells, T_{sub} was decreased to ~500 °C. The N plasma power condition for the shell was 0.9 sccm, 250W, and the shells were grown for 10-30 min. Decreasing T_{sub} reduces Ga adatom mobility on the growing surfaces. This decreased mobility suppresses axial growth rate and promotes the radial growth rate through the step-mediated growth mode. Most of Ga adatoms on the sidewall of the NWs will be kept from diffusion all the way to the Ga droplets on the NW tip; otherwise, they would contribute to the NW axial growth.

3.4.2 Structural properties and discussion

The SEM images in Figure 3.7 show the evolution in the morphology of GaAsP/GaNAsP core/shell NWs for shell growth duration between 0 and 30 min. It is assumed that all the Ga adatoms will be incorporated in the growing NW shells. We assume that the NW growth occurs only in the radial direction at low growth temperature. Therefore, the NWs maintain a constant length l throughout the shell growth. An area A surrounding the NW represents the collection area of adatoms. Atoms impinging in this area can reach the NW interface by diffusion and contribute to radial growth. Under the above assumptions, the total number of atoms in the shell is given by

$$FAdt = nl \times 2\pi r dr \tag{3.3}$$

where F is the flux of Ga atoms and r is the radius of the NW.

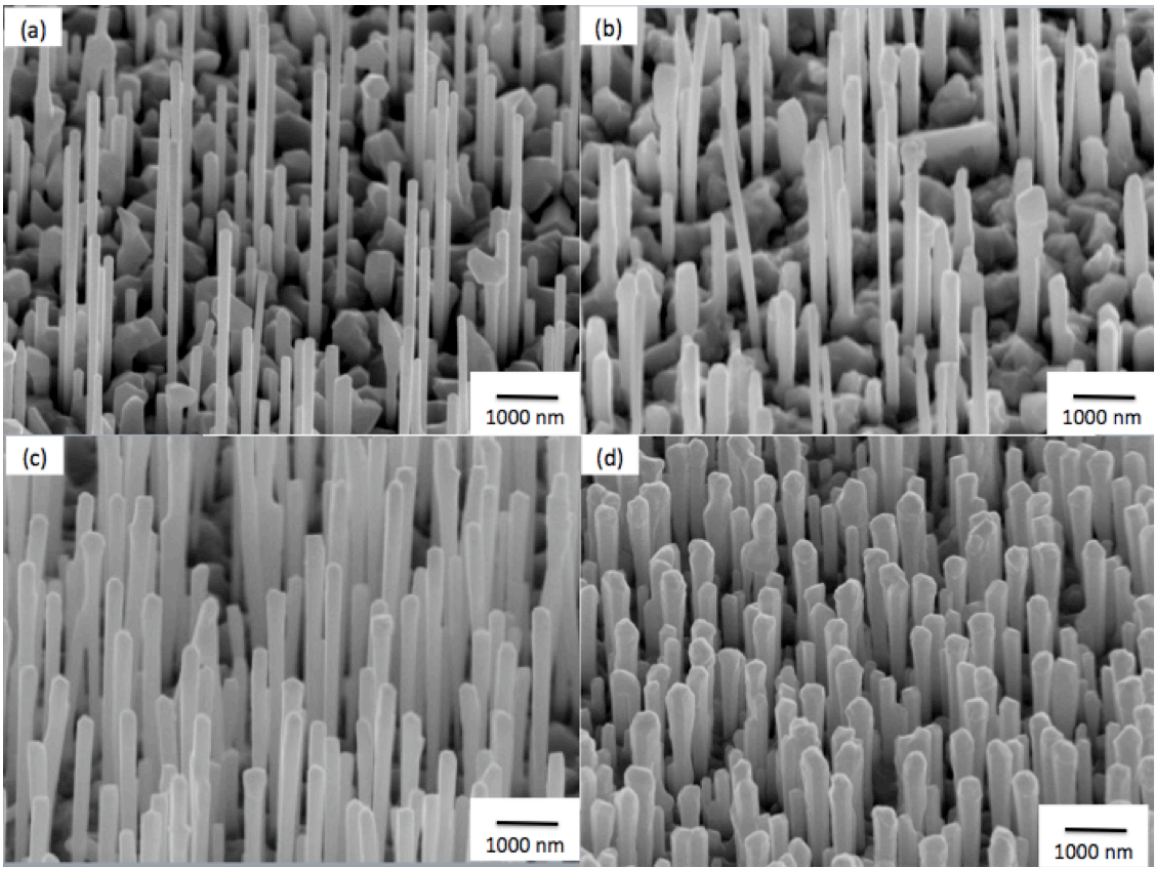

Figure 3.7. SEM images of (a) GaAsP/GaNAsP core/shell NWs on Si (111), shell growth temperature = 500 °C, shell growth time = (b) 10 min, (c) 20 min, and (d) 45 min.

The data point in Figure 3.8 Show the NW radius evolution (i.e., r as function of the growth duration) for the case l = 2.1μm, For the purpose of comparison with Eq. (3.3), various parameters need to be established. The Ga flux is 0.7 monolayer/s calibrated by RHEED oscillation. The size of the collection area A surrounding the NW is fixed to 2.5×10^5 nm^2, an average value measured from SEM pictures. Note that the parameters in Eq. (3.3) quantitatively explain the measured data in Figure 3.8

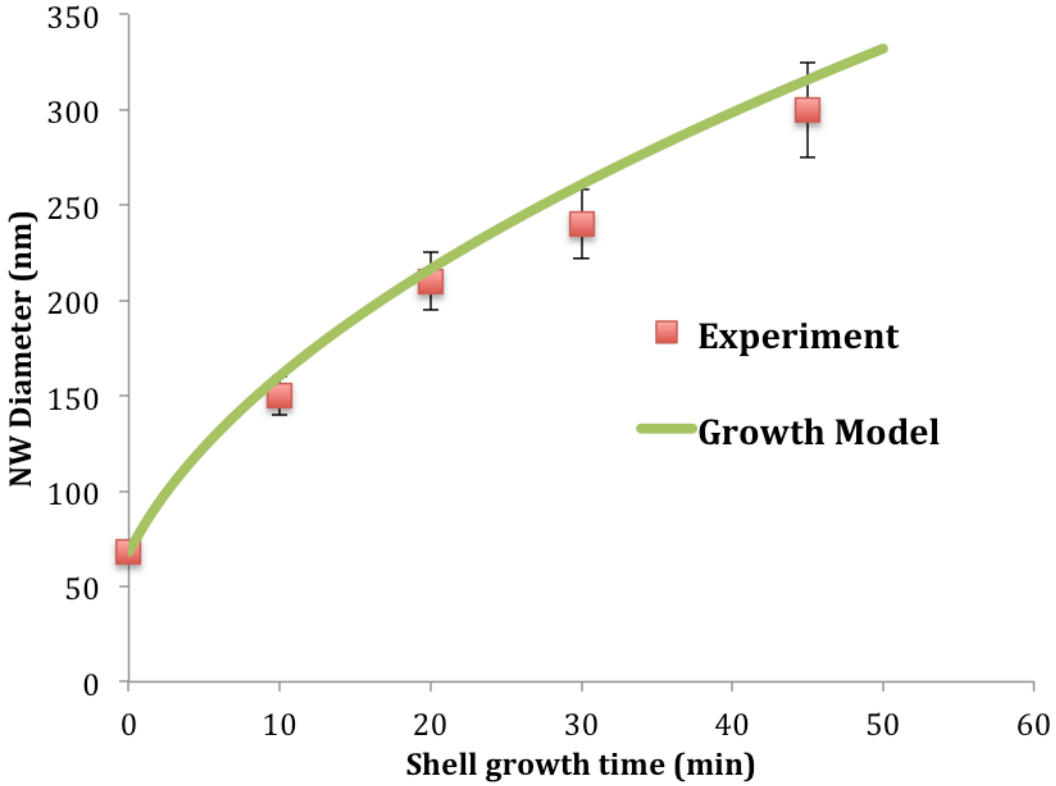

Figure 3.8 Dependence of the NW diameter on shell growth time. The GaAsP core growth time was 20 min.

3.5 Conclusion

In this chapter, vertical self-catalyzed Ga(N)AsP NWs and GaAsP/GaNAsP core/shell nanowires have been grown on Si (111) by GSMBE. The growth window such as substrate temperature and V/III ratio of the NW growth is investigated. Increasing concentration of N consumes Ga droplets, resulting in shorter and larger diameter of NWs. Finally, The diameter of NWs respect to the growth time is studied.

3.6 Acknowledgments

This chapter has been published in “Self-catalyzed Ga (N) AsP nanowires and

GaAsP/GaNAsP core–shell nanowires grown on Si (111) by gas-source molecular beam epitaxy", Rui La, Janet L. Pan, Faebian Bastiman, Charles W. Tu, J. Vac. Sci., Technol. B 34, 02L108 (2016). The dissertation author was the primary investigator and author of this paper.The work was partially supported by the National Science Foundation under Grant No. DMR-1106369.

Reference:

[1] Maoqing Yao, Sen Cong, Shermin Arab, Ningfeng Huang, Michelle L. Povinelli, Stephen B. Cronin, P. Daniel Dapkus, and Chongwu Zhou. Tandem solar cells using GaAs nanowires on Si: Design, fabrication, and observation of voltage addition. Nano Letters, 15(11): 7217, 2015.

[2] Andreas Brenneis, Jan Overbeck, Julian Treu, Simon Hertenberger, Stefanie Morkt- ter, Markus Dblinger, Jonathan J. Finley, Gerhard Abstreiter, Gregor Koblmller, and Alexander W. Holleitner. Photocurrents in a single InAs nanowire/silicon heterojunc- tion. ACS Nano, 9(10):9849–9858, 2015.

[3] Mattias Borg, Heinz Schmid, Kirsten E. Moselund, Giorgio Signorello, Lynne Gignac, John Bruley, Chris Breslin, Pratyush Das Kanungo, Peter Werner, and Heike Riel. Vertical III-V nanowire device integration on Si(100). Nano Letters, 14(4):1914–1920, 2014.

[4] Jesper Wallentin, Nicklas Anttu, Damir Asoli, Maria Huffman, Ingvar berg, Martin H. Magnusson, Gerald Siefer, Peter Fuss-Kailuweit, Frank Dimroth, Bernd Witzigmann, H. Q. Xu, Lars Samuelson, Knut Deppert, and Magnus T. Borgstrm. InP nanowire array solar cells achieving 13.8% efficiency by exceeding the ray optics limit. Science, 339(6123):1057–1060, 2013.

[5] Jia Zhu, Zongfu Yu, George F. Burkhard, Ching-Mei Hsu, Stephen T. Connor, Yueqin Xu, Qi Wang, Michael McGehee, Shanhui Fan, and Yi Cui. Optical absorption enhancement in amorphous silicon nanowire and nanocone arrays. Nano Letters, 9(1):279–282, 2009.

[6] Yue Liang, William D. Nix, Peter B. Griffin, and James D. Plummer. Critical thickness enhancement of epitaxial SiGe films grown on small structures. Journal of Applied Physics, 97(4):043519, 2005.

[7] Brendan M. Kayes, Harry A. Atwater, and Nathan S. Lewis. Comparison of the device physics principles of planar and radial p-n junction nanorod solar cells. Journal of Applied Physics, 97(11), 2005.

[8] R. S. Wagner and W. C. Ellis. Vapor-liquid-solid mechanism of single crystal growth. *Applied Physics Letters*, 4(5), 1964.

[9] Jiangtao Hu, Teri Wang Odom, and Charles M. Lieber. Chemistry and physics in one dimension: synthesis and properties of nanowires and nanotubes. *Accounts of Chemical Research*, 32(5):435–445, 1999.

Chapter 4

The Characterization of Ga(N)AsP/GaNAsP NWs on Si substrate

4.1 Overview

This chapter is devoted to the optical characterization of GaAsP, GaNAsP, and GaAsP/GaNAsP NWs. A variety of optical characterizations techniques are used to study the optical properties of these materials, especially the effect incorporating a small amount of nitrogen in the traditional III-V semiconductor system. In this chapter, the optical properties are characterized different techniques. Photoluminescence (PL), energy

dispersive x-ray (EDX) and rapid thermal annealing (RTA) are completed in University of California San Diego. Photoluminescence excitation (PLE) and cathodoluminescence (CL) are measured in our collaborator's lab in Linköping University.

4.2 Determination of P composition in Ga(N)AsP NWs

Energy-dispersive X-ray spectroscopy (EDX) is an analytical technique used for elemental analysis or chemical characterization of a sample. To study the effects composition of NWs, EDX was used to acquire the spectra. The EDX is performed with a FEI Quanta Scanning electron microscope. Figure 4.1 shows the EDX signal from scanning the electron beam on the GaAsP (HN) and GaNAsP NWs, where the signal has been integrated over the whole scan length and normalized to the Ga Kα-peak intensity. It can be seen that the relative peak intensities of the P, As, and Ga peaks are quite similar on these two NWs samples. Therefore, incorporation of N did not change As/P ratio obviously in GaNAsP NWs. This in turn implies that the N content in the GaNAsP NWs is very low, below the detection limit of approximately 2%. Consistently, no N Kα-peak was detected in the EDX spectra. On the basis of the measured intensity ratios between the Kα-peak, the P composition is estimated to be around 29% $\pm$ 5%.

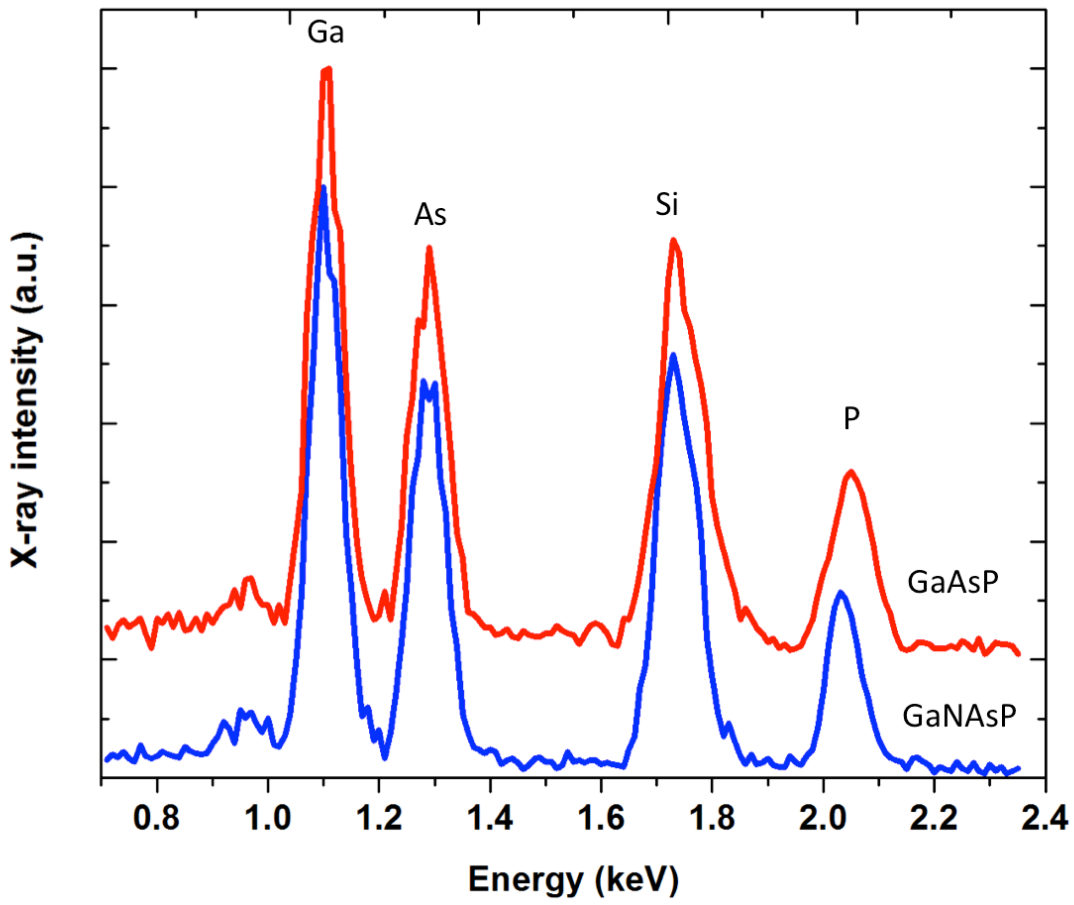

Figure 4.1 EDXS spectra, acquired from GaAsP and GaNAsP NWs.

4.3 Determination of N composition in Ga(N)AsP NWs

4.3.1 PL and PLE

The optical properties of GaAsP and GaNAsP NWs were studied with PL spectroscopy from the 532 nm excitation from a diode-pumped solid-state laser at 10 W/cm^2. A monochromator was used to disperse the PL spectra, which were then detected by a photomultiplier tube (PMT). The response curve of R636-10 PMT tube was applied to normalize PL curves. The room-temperature PL spectra shown in Figure 4.2 were obtained from GaAsP and GaNAsP with various nitrogen plasma conditions. The growth

conditions for these NWs are described in section 3.3.1. N0, LN, MN, and HN represent samples with different nitrogen concentrations (zero, low, medium and high [N]). The spectral peak of the PL emission from GaAsP is around 720 nm with a full width at half maximum of about 30 nm. The peaks in the emission from samples LN, MN, and HN are around 750, 775, and 800 nm, respectively. The dilute nitride NWs show a red shift with respect to the GaAsP NWs, and the shift increases with increasing N content. This red shift suggests that the higher flux leads to higher nitrogen content. From the plot, it is apparent to see a broader and more asymmetric line shape of PL emission from N incorporated samples. Also, a tail or shoulder extending to the low energy side of the PL spectra is observed. This lower energy shoulder of GaNAsP NWs is due to N related defects and variation in N compositions between individual wires within the NW array,[5] as it is also observed in micro-CL spectra acquired from a single NW. The asymmetric PL line shape and related broadening are observed in the study of dilute nitrides materials.[1,2] Previous studies of GaNAsP quantum well structures have shown that the emission at low temperature is dominated by localized exciton (LE) recombination, where the excitons are localized within band tail states arising from compositional fluctuations.[3] Chen et. al stated that similar results were observed in GaAs/GaNAs core/shell NWs in 2014.[4]

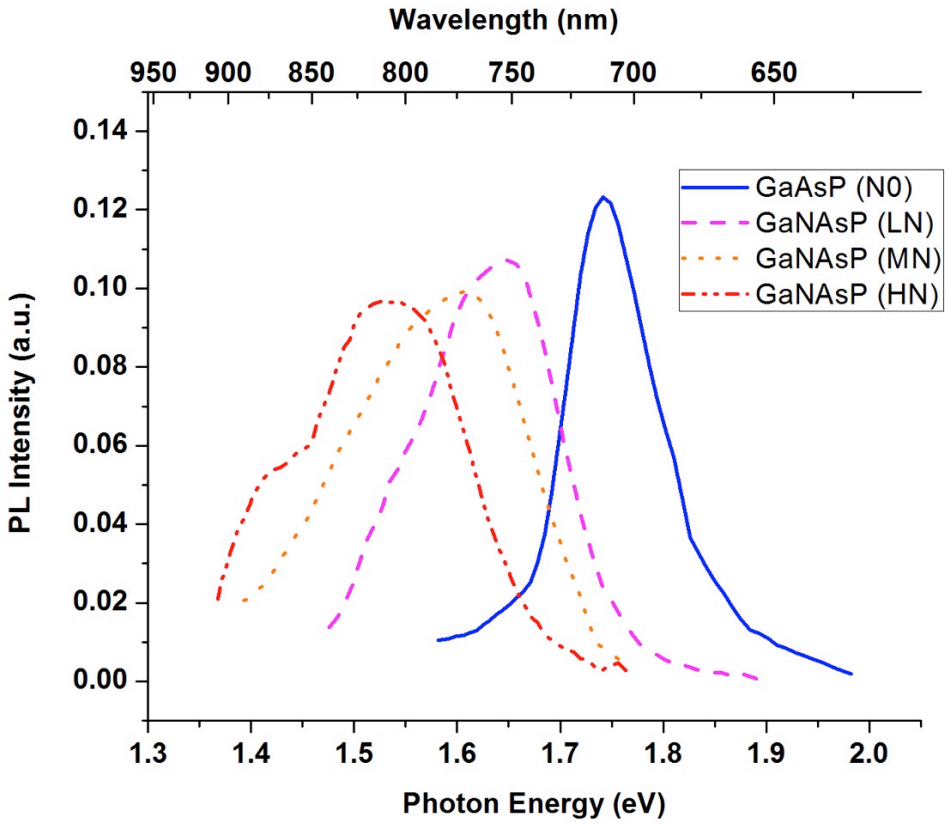

Figure 4.2 PL of GaAsP NWs and GaNAsP (LN, MN, HN) NWs arrays grown with increasing N flux.

4.3.2 Temperature dependent PL of Ga(N)AsP NWs

To further investigate the energy band states in NWs, a comparison of the spectral positions of the peak in the temperature-dependent PL spectra between GaAsP NWs and GaNAsP (HN) NWs is shown in Figure 4.3. The blue dots represent the peak positions of the emission from the GaNAsP NWs, where the orange dots show the peak positions of the corresponding PL bands from the GaAsP NWs. There are two types of recombination mechanism, localized exciton (LE) recombination and free exciton (FE)

recombination. As the sample temperature increases from 50 K to 150 K, the PL peak from localized excitons of the GaNAsP NWs sample red shifts due to bandgap shrinkage with increasing temperature. At 150 K the PL peak blue shifts due to detrapping of excitons. Electrons are now in the conduction band, and free exciton emission is dominant. Near 220 K the PL peak red shifts due to band shrinkage with temperature. The spectral positions of the peak from an S-shape with decreasing temperature and this phenomenon can be explained by the defect-band filling in the dilute nitride. At low temperature, optically pumped electrons from the valence band fill the N-related defect states in the bandgap; while at a higher temperature, electrons have enough thermal energy to hop into the conduction band. For the recombination mechanism, the excitons are trapped at the localized states at low temperature. As the temperature increases, the detrapped exciton jump into free exciton state and free carrier recombination start to appear. As a result, the peak from dilute nitrides in general exhibits an S-shape. For GaAsP NWs, we can only see a red shift of the peak with increasing temperature the peaks from the GaAsP NWs following the Varshni model[6],

$$E(T) = E(0) - \frac{\alpha T^2}{T + \beta} \tag{4.1}$$

where E(T) is the bandgap at temperature T, E(0) is the bandgap at 0K, and α and β are Varshini coefficients defining the shape of the dependence. The bandgap of GaNAsP NWs is less temperature sensitive than GaAsP at a high measurement temperature, as observed previously.[5] It can be concluded that the energy difference between FE energy and LE energy is larger for the GaNAsP wires and that the transition between FE and LE

carrier emission occurs at high temperature is more obvious compared to GaAsP wires. This finding proves that the localization potential becomes deeper with an incorporation of nitrogen. Similar results were concluded in the research of GaNP[6] and GaNAs[7] nanowires.

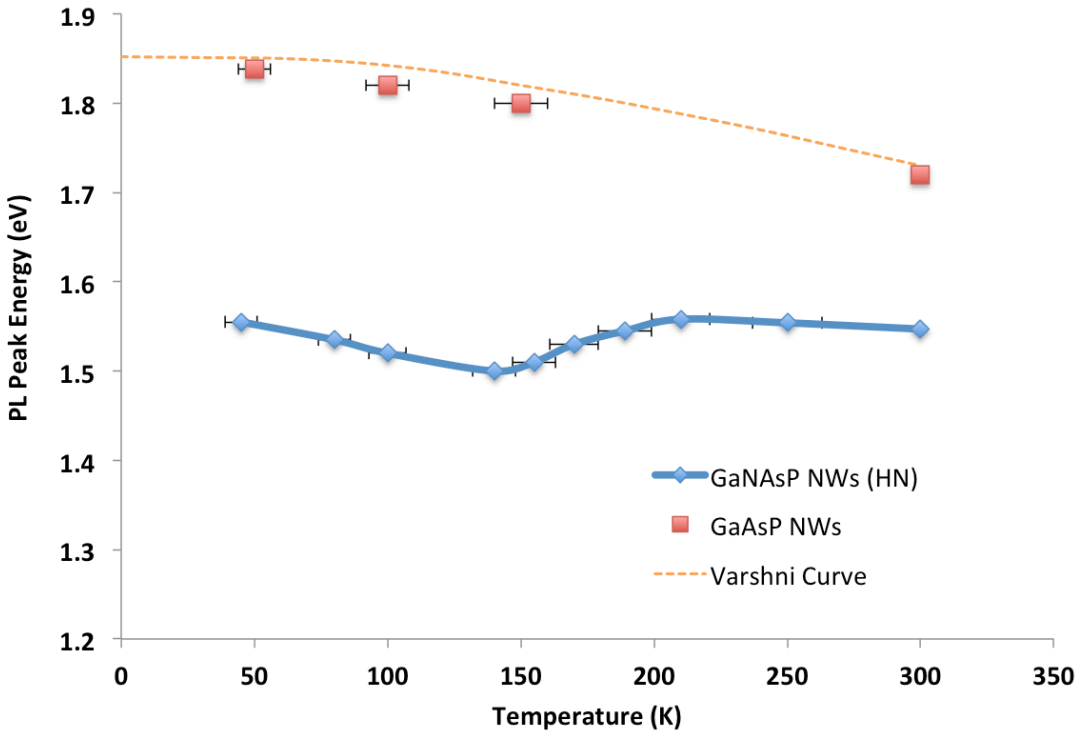

Figure 4.3. PL peak energy across 50 – 300 K of GaAsP NWs and GaNAsP (HN) NWs. The dotted line is the best fits to the experimental data using the Varshni equation for the GaAsP NWs

4.3.3 Alloy composition

The aforementioned results from the temperature-dependent PL measurements allow us to investigate the As/P ratio in the NWs and also to determine the N composition. Based on the band anticrossing (BAC) model, the bandgap energy of GaNAsP NWs

(E_g^{GaNAsP}) can be calculated using equation 4.2 from the BAC model. The calculation of E_g^{GaNAsP} is to calculate E. in the equation. Thus, the equation to calculate E_g^{GaNAsP} is

$$E_g^{GaNAsP} = \frac{1}{2}\{[E_g^{GaAsP} + E_N] \pm \sqrt{[E_g^{GaNAsP} - E_N]^2 + 4C_{NM}^2 \cdot x}\} \quad (4.2)$$

In the equation, both E_N and C_{NM} of GaNAsP can be calculated by a linear interpolation from E_N and C_{NM} of GaNAs and GaNP system. The E_g^{GaAsP} and E_g^{GaNAsP} can be measured from the peak position of the PL spectrum. The P composition x as the bandgap of $GaAs_{1-x}P_x$ can be computed by the following equation:

$$E_g^{GaAs_xP_{1-x}} = xE_g^{GaAs} + (1-x)E_g^{GaP} - x(1-x)\beta \quad (4.3)$$

where β= 0.19 is the bowing parameter of GaAsP[8] and E_g^{GaAs} and E_g^{GaP} are the temperature-dependent bandgaps of GaAs and GaP, respectively. Since the As/P ratio is not apparently affected by the presence of nitrogen, the nitrogen composition of the GaNAsP NWs can be determined as y = 0.8%, 1.4% and 3% in the LN, MN, and HN NWs, respectively. One thing worth noticing is that in spite of the very low N composition, the bandgap energy of the GaNAsP NWs can be varied by more than 100 meV.

4.4 CL measurements of single NW

In addition to PL measurements, room temperature cathodoluminescence (CL) was measured on single GaAsP and GaNAsP (MN) NWs. The CL spectra were obtained by scanning the electron beam along the NW axis. The CL spectra are shown in Figure 4.4. The dots on Figure 4.4(a) SEM images represent the focusing point of CL spectra. Here, the excitation volume of the beam is much smaller (with a typical radius of about

100 nm for an acceleration voltage of 5 kV) than the length of NWs, which allows direct correlation between the NW morphology and emission. The CL spectra in Figure 4.4 (a) show a broad shape and peaks shifting from 760 nm to 800 nm from bottom to the tip of single NW. The tapered NW indicates that the growth is affected by N flux, which is discussed in chapter 3. From the CL spectra, we can conclude that with a higher N composition show a gradual shift of the emission spectra along the wire, indicative of changes in [N] along the wire. Figure 4.4 (b) shows the CL spectra of GaNAsP (LN) NW with constant peak positions around 750 nm. This emission originates from the GaNAsP NW with the uniform diameter along the wire. By comparing the results of the CL mapping with the overview SEM image shown on the side, it becomes clear that the tapered NW structure originates from non-uniform of nitrogen distribution inside NW position along the wire from GaNAsP (LN) sample.

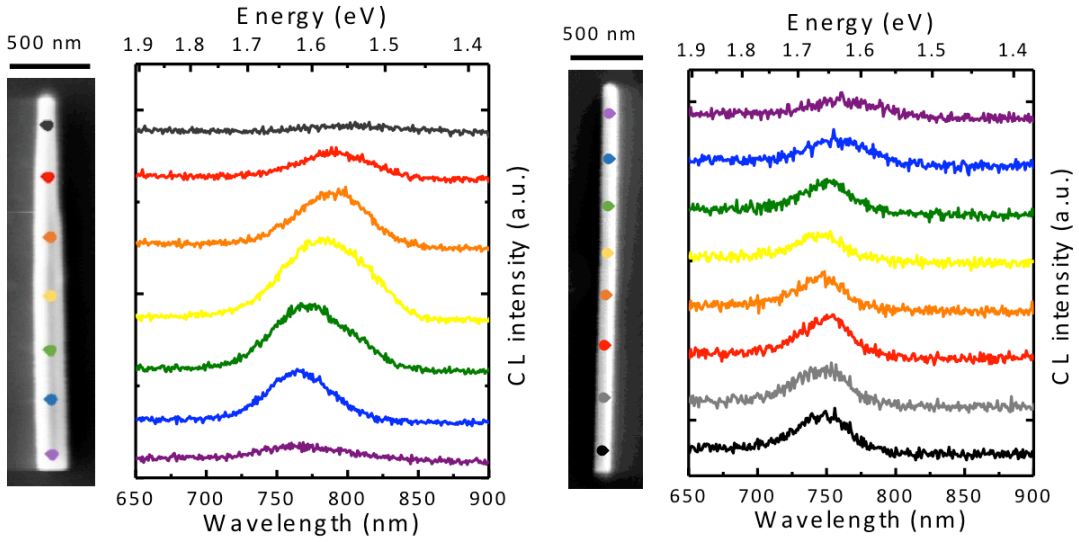

Figure 4.4 CL spectra measured from GaNAsP NW with different nitrogen concentration. (a) CL spectra measured as a function of the wavelength and emission position along the wire from GaNAsP (HN) sample. (b) CL spectra measured as a function of the wavelength and emission

4.5 Effect of RTA on NWs

To improve the crystal quality of the GaNAsP NWs, rapid thermal annealing (RTA) was done on one MN sample. The sample was annealed at a series of temperature for 60s in forming gas (5% hydrogen balanced with nitrogen). Figure 4.5 shows the improvement in the PL for different annealing temperatures along with the as-grown sample. The maximum PL intensity appears at the annealing temperature of 950 °C, where the band tail is significantly reduced, indicating N related defects are partially removed and the crystal quality is improved. The as-grown sample with N incorporation shows some defects at the low-energy tail, which is primarily due to N-induced defects. RTA is essential for dilute nitride-based materials, as it will improve the crystal structure and improve the minority carrier lifetime and the diffusion length. The blue shift in the spectral peak after the RTA, observed commonly in dilute nitrides, is believed to result from an RTA-induced structural change with an accompanying bandgap change. RTA is important for dilute nitride materials and solar cell devices since the introduction of N into the crystal will largely reduce the minority carrier lifetime and diffusion length. Because of high electron negativity of N, such effect is more obvious on electrons than on holes. There are a large amount of anti-site defects that trap or induce recombination for the photo-generated minority electrons in the dilute materials without annealing. Therefore, RTA or passivation processes are very critical steps for solar cell fabrication.

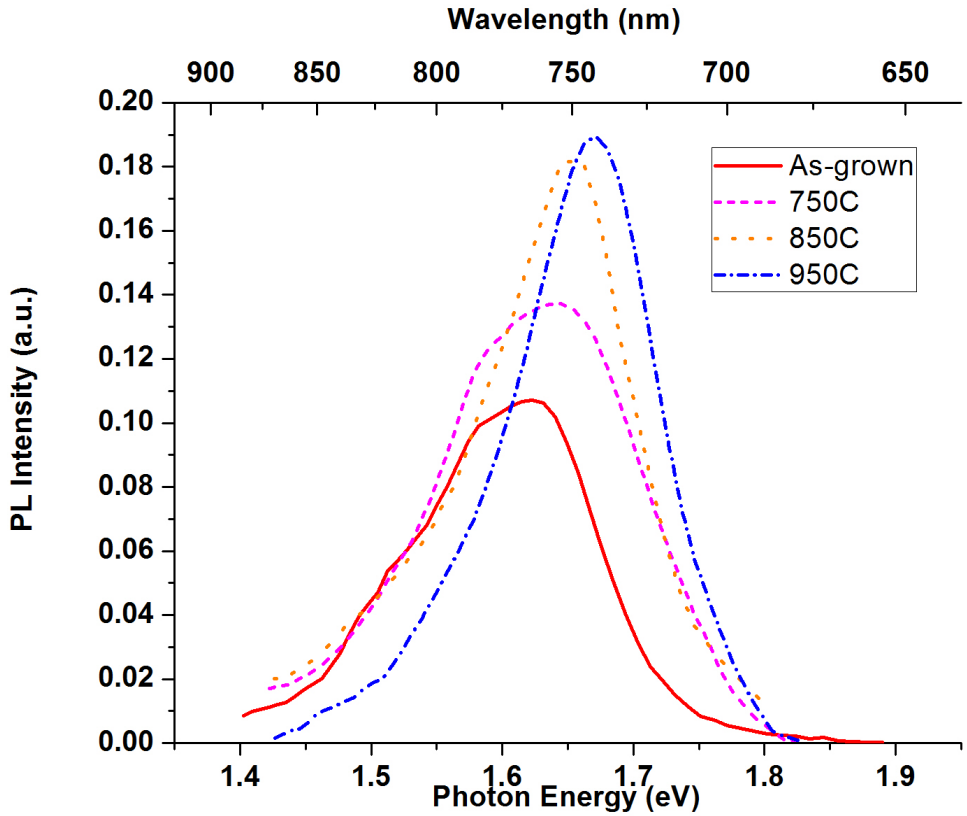

Figure 4.5 Room temperature PL intensity of GaNAsP NWs (MN) improved by rapid thermal annealing.

4.6 PL on GaAsP/GaNAsP core-shell NWs

To further investigate the origins of PL from GaAsP/GaNAsP core-shell NWs, the PL spectra of GaAsP/GaNAsP core-shell NWs, GaAsP NWs, and GaNAsP NWs are compared. The PL emission shows a single PL peak for all the NWs including core/shell GaAsP/GaNAsP NWs. Figure 4.6 shows room-temperature emission from GaAsP/GaNAsP core-shell NWs with peak intensity at ~820 nm which exhibits their good optical quality and demonstrates their potential application as optoelectronic materials. By comparing PL peaks from GaAsP/GaNAsP core-shell NWs with GaAsP

NWs and GaNAsP NWs (HN), we conclude that the emission is attributed to the GaNAsP shell layer, as a result of fast diffusion of photo-excited electrons from the core to the shell with lower conduction band edge. This is expected from the band alignment that the conduction band of GaNAsP is lower than that of GaAsP. It should be noted that the PL peak of GaNAsP NWs (HN) shows at slightly higher energy than core-shell GaAsP/GaNAsP NWs. This is believed to be the effect of variation of N composition between the shell of GaAsP/GaNAsP NWs and GaNAsP NWs. Also, the shoulder effect existed in GaNAsP NWs is not obvious in GaAsP/GaNAsP NWs. As is discussed above, the tail or shoulder effect extending to lower energy part is attributed to the N related defects. The GaNAsP shell in core-shell NWs is grown on GaAsP core, which has small lattice mismatch with GaNAsP. Therefore, the N related defects are reduced. With regard to higher energy peak of GaAsP NWs, the N composition in GaNAsP shell is approximately 0.16%. This is consistent with N composition in HN GaNAsP NWs.

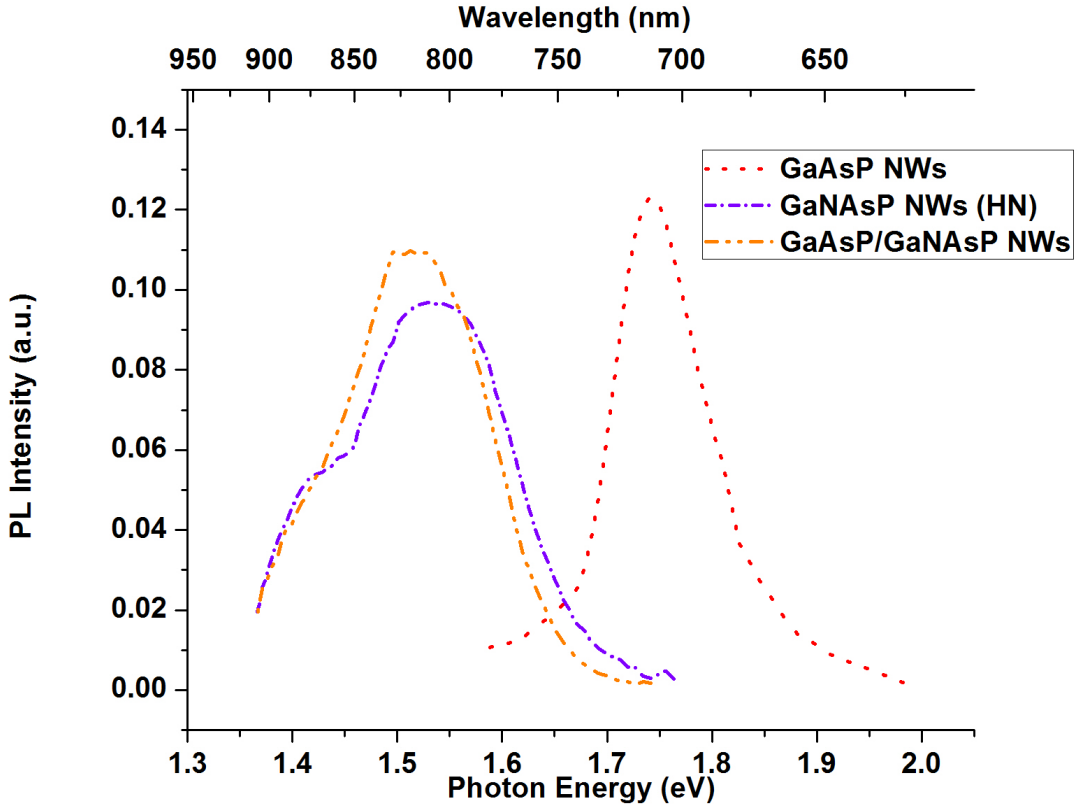

Figure 4.6 RT PL of GaAsP NWs, GaNAsP NWs (HN) and GaAsP/GaNAsP core/shell NWs.

4.7 Conclusion

In summary, the optical properties of GaNAsP and GaAsP/GaNAP core-shell NWs are characterized. Optical emission from GaNAsP NWs indicates a decreasing bandgap with increasing N. The spectral peak of temperature-dependent PL from GaNAsP NWs exhibits an S-shape. At high temperature, the emission comes from band-to-band radiative recombination. At low temperature, the emission originates from N-related localized states below the conduction band. The room temperature PL from

N-related defects can be reduced by rapid thermal annealing. The PL from GaAsP/GaNAsP core-shell NWs exhibit a red shift with respect to the PL from GaAsP NWs. This indicates that the optical emission comes from the GaNAsP shell layer.

4.8 Acknowledgments

This chapter has been published in "Self-catalyzed Ga(N)AsP nanowires and GaAsP/GaNAsP core–shell nanowires grown on Si (111) by gas-source molecular beam epitaxy", Rui La, Janet L. Pan, Faebian Bastiman, Charles W. Tu, J. Vac. Sci., Technol. B 34, 02L108 (2016). The dissertation author was the primary investigator and author of this paper.The work was partially supported by the National Science Foundation under Grant No. DMR-1106369.

Reference

[1] I. A. Buyanova, W. M. Chen, W. M., Eds. Phys and Appl of Dilute Nitrides, (2004).

[2] C. Karcher, H. Gruning, M. Gungerlich, P. J. Klar, K. Volz, W. Stolz, W. Heimbrodt, Phys. Status Solidi C 6, 2638, (2009).

[3] B. Kunert, K. Volz, I. Nemeth, W. Stolz ,and J. Lumin. 121, 361, 2006.

[4] S. L. Chen, S. Filippov, Fumitaro Ishikawa, W. M. Chen, and I. A. Buyanova, 105, 253106, (2014).

[5] V. A. Odnoblyudov and C. W. Tu, J. Vac. Sci. Technol., B 24, 2202 (2006).

[6] Y. P. Varshni, Physica 34, 149, (1967).

[7] S. Filippov, M. Jansson, J. E. Stehr, J. Palisaitis, P. O. Å. Persson, F. Ishikaw W. M. Chen and I. A. Buyanova, Nanoscale 35, 15935, (2016)

Chapter 5

GaAs/GaNAs NWs grown on patterned Si (111) substrate

5.1 Overview

This chapter is devoted to the epitaxial growth of GaAs/GaNAs core-shell nanowires (NWs) on patterned Si (111) by self-catalyzed method using GSMBE. The growth conditions of GaAs NWs on patterned Si substrate are investigated. The objective of growing GaAs/GaNAs core-shell NWs on patterned Si is to improve device performance, such as to achieve high-efficiency NW solar cells. The optimized substrate temperature and diluted HF etching time are investigated to have the highest yield of the growth. Optical properties are studied using micro-PL (μ-PL) and micro-Raman

(μ-Raman) spectroscopy. Transmission electron microscopy (TEM) is used to study the crystal structure and defects in the NWs. The μ-PL and μ-Raman spectrum are measured in Linköping University and TEM is measured in Los Alamos National Laboratory.

5.2 Selective Area Growth

In previous sections, we have discussed the growth of NWs on Si (111) randomly. To improve device performance, such as to achieve high-efficiency NW solar cells[1, 2], NWs should locate on precise positions. Thus, controlling the NW position is of critical importance. Also, the parasitic cluster deposition, which is often accompanied with the NW growth on unpatternted substrates, can be suppressed by pattern growth. Therefore, significant work has been reported on III-V NW growth on a patterned Si substrate using the gold-catalyzed method[3-6]. The self-catalyzed growth method, by depositing one layer of Ga droplets on the Si substrate before growth, has the advantage of avoiding contamination associated with foreign metal catalytic droplets.[7, 8] In Chapters 3 and 4, we demonstrate the growth of GaAsP/GaNAsP core-shell NWs Si. However, to better investigate the growth condition of selective area growth (SAG), GaAs/GaNAs system is chosen because it is simpler than the GaAsP/GaNAsP system.

The process of Selective Area Growth in GSMBE is shown in Figure 5.1 First, the substrate was etched with hydrofluoric (HF) solution cleaned with Acetone, IPA, and DI water to remove metal particles and contamination from their surfaces. Then, SiO_2

was formed by PECVD at 350 ℃. Reactive-ion etching (RIE) was then used to form periodic opening patterns on the Si surface. The masked substrates was then slightly etched with buffered HF solution to remove the native oxide that formed in the opening area during these processes. Finally, NWs were grown on the masked substrate by GSMBE.

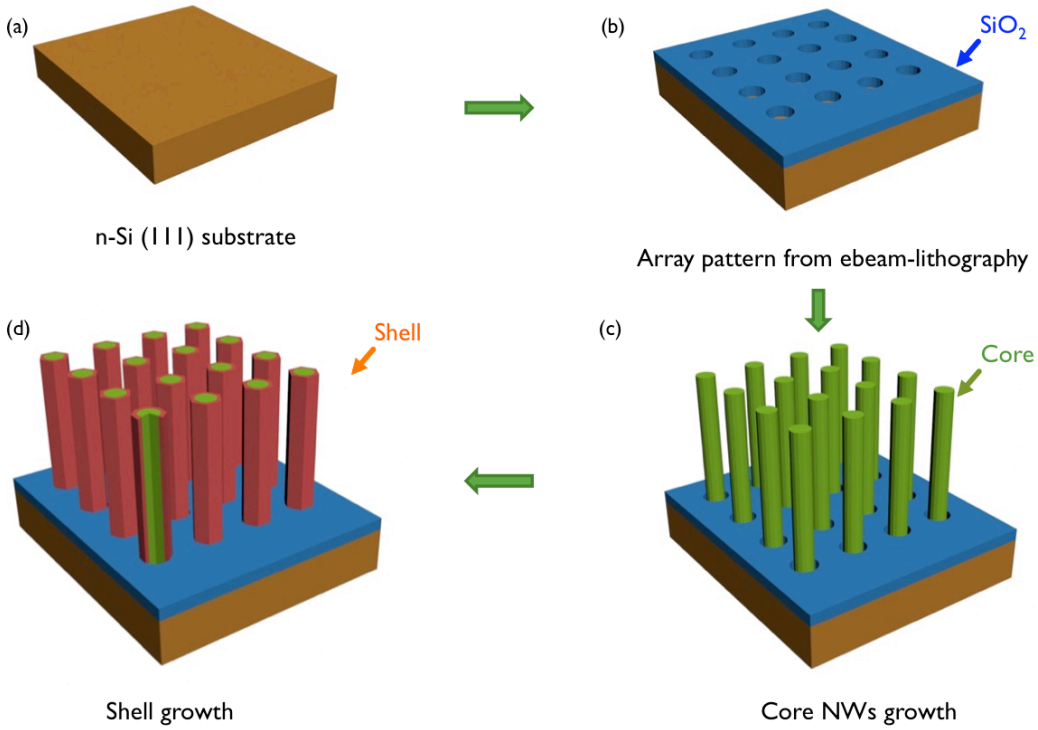

Figure 5.1 Illustration of Selective Area Growth. (a) n-Si (111) substrate. (b) Deposition of 45-nm-thick SiO_2 film on Si (111) substrate by PECVD and definition of patterns by E-beam lithography and RIE etching. (c) MBE growth of core GaAs NWs. (d) MBE growth of shell GaNAs layer.

5.3 Growth of GaAs/GaNAs NWs

5.3.1 Pattern preparation

Patterned Si (111) substrates were prepared using electron beam lithography[9].

First, a layer of silicon dioxide (SiO_2) was grown by plasma-enhanced chemical vapor deposition (PECVD). A polymethyl methacrylate (PMMA) resist was subsequently spin-coated and baked at 180 °C for 10 min on a hotplate, resulting in a thickness of about 120 nm. Electron beam lithography (EBL) was performed using a JEOL 6400 SEM/NPGS EBL system. After a dose optimization step, the array with the diameter of ~90 nm and inter-hole center spacing (pitch) of 1.5 μm was written on PMMA. The pattern was transferred to the SiO_2 layer by reactive ion etching (RIE) using a Plasma Lab 80 chamber from Oxford Instruments. Optimized chamber conditions were used to promote anisotropic etching using a $CF_4/CHF_3/Ar$ mixture applied to SiO_2 etching. Then the PMMA resist was stripped using Acetone solution. Prior to the introduction of the samples into the ultra-vacuum environment, a diluted aqueous hydrofluoric acid (HF) solution was used to chemically etch the substrates in attempt to remove the native oxide from the patterned holes. HF was diluted in DI water at a ratio of 1:40. Different dipping time was used to investigate the effects of the HF etching time on the NWs growth. The optimized final mask SiO_2 thickness was ~30 nm, measured from transmission electron microscopy (TEM). The substrates were then rinsed with deionized water, dried with nitrogen and then transferred into the MBE chamber immediately.

The NW samples were grown in a Varian Gen-II MBE system modified to handle gas sources. Thermally cracked AsH_3 was used as the As_2 source, while solid elemental Ga was used to generate a Ga atomic beam through an effusion cell. The substrate was heated to 690 °C for 15 min before growth.

For NW growth, Ga atoms were deposited on the Si (111) surface for 1 minute with a Ga flux of ~0.7 monolayer/s, calibrated by Ga-induced reflection high-energy electron diffraction (RHEED) intensity oscillation for the planar growth of GaAs under the same substrate temperature (T_{sub}). Then the substrate was annealed for 30 s to form Ga droplets inside the holes. GaAs NWs growth last 20 minutes at a V/III incorporation ratio of 2 and a substrate rotation speed of 3 RPM, which ensure sample uniformity. The AsH_3 flow rate was set at 3 sccm during growth. Scanning electron microscope (SEM) measurements of the NWs were performed with an FEI XL30 ultra-high resolution SEM system.

5.3.2 Effect of HF etching time

It is believed that the HF treatment can not only remove the native oxide layer but also form a stable hydrogen-terminated Si surface[10]. The effect of using a diluted HF solution to remove oxide in the patterned holes prior to the growth of GaAs NWs was first investigated. Figure 5.2 shows 45° tilted SEM images of GaAs NWs with various diluted HF etching time. In the first case of Figure 5.2(a) (without HF etching), a significant number of patterned holes are vacant. For the longer etching time (10 s), more holes are occupied by NWs and the diameters of holes are larger than holes in Figure 5.2(a). Further increasing the etching time to 30 s, most holes are occupied by NWs and none is vacant as observed in Figure 5.2(c). When the etching time was increased to 60 s, NWs grew randomly on the Si substrate as non-patterned growth reported in the previous

work[11]. These results suggest that the patterned holes in Figure 5.2(a) (b) might be entirely or partly covered by the native oxide and/or SiO_2 residue prior to NWs growth. Although there are a few holes covered by parasitic clusters in Figure 5.2(c), most of the holes are grown with NW, indicating that native oxide was removed after 30 s diluted HF etching. It is believed that the formation of GaAs NWs started from some pinholes in intergranular regions etched by HF solution. The Ga droplets could only reach the Si substrate through a pinhole after HF etching. However, for longer etching time in Figure 5.2(d), the HF rapidly removed SiO_2 pattern and created excessive nucleation area for Ga droplets and lead to a random growth of NWs on the whole substrate. The corresponding yields, depicted in Table 5.1, are 1%, 18%, and 62%, respectively. At HF etching time of 60 seconds, the NWs were randomly grown on the substrate due to the removal of the SiO_2 pattern.

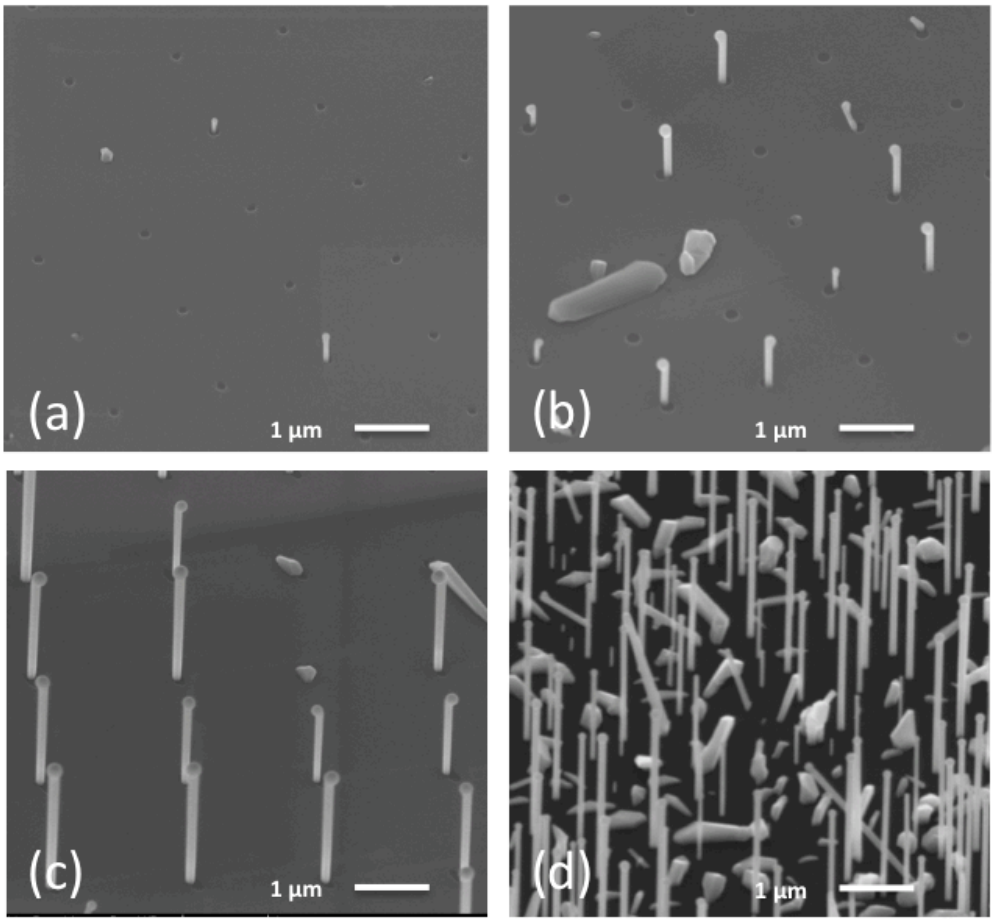

Figure 5.2 SEM images of GaAs core NWs on Si (111) with diluted HF etching time of (a) t = 0 s, (b) t = 10 s (c) t = 30 s, (d) t = 60 s. Ga flux was set at 0.7 monolayer/s, growth time = 20 min. HF was diluted in DI water at a ratio of 1:40.

Table 5.1 SAG yield under different HF etching time

Sample	Substrate Temp (°$\boldsymbol{C}$)	HF etching time(s)	Yield
H0	690	0	~1%
H10	690	10	~18%
H30	690	30	~62%
H60	690	60	Random

5.3.3 Effect of substrate temperature

Next, we optimized the morphology of the grown GaAs NWs by studying the effects of the growth temperature, T_{sub} of 630, 650, 670 and 690 °C. Prior to growth, all the samples were dipped in dilute HF for 30 s to fully remove the native oxide. Figure 5.3 shows SEM images of NWs with different growth temperatures. As illustrated in the images, the higher the growth temperature, the higher is the NW growth yield. In the vapor-liquid-solid (VLS) mechanism, liquid droplets act as the catalyst and absorb vapor components (both Ga and As here) to incorporate into and supersaturate alloy droplets (Ga rich here) and initiate the growth of the reaction byproduct (GaAs NW) from the supersaturated melt. At high T_{sub}, Ga adatom mobility is increased. Consequently, most adatoms can diffuse to the Ga droplet in the SiO_2 hole or on the NW tip, which provides abundant Ga replenishment for a well super-saturated GaAs NW VLS growth. This is in accordance with the NW growth results of Figure 5.3(d). When the T_{sub} is low, the Ga adatoms are not only diffusing and incorporating into the droplet but also deposited together with As in the vacant oxide-free area in the hole, preventing the formation of a Ga rich melt for the VLS growth and resulting in a direct vapor-solid (VS) GaAs cluster growth in the hole. (e.g. Figure 5.3 (a)).

The higher growth rate of NWs via the VLS mechanism depends on several factors such as better absorption on the droplet, a high rate of chemical reaction and a faster nucleation of crystal phase. In our NWs growth, the higher substrate temperature could lead to faster diffusion of Ga adatoms from substrate surface to the tip of the NWs as the

diameter of the NWs increases. Table 5.2 shows that the higher NWs growth yield is achieved at higher growth temperatures.

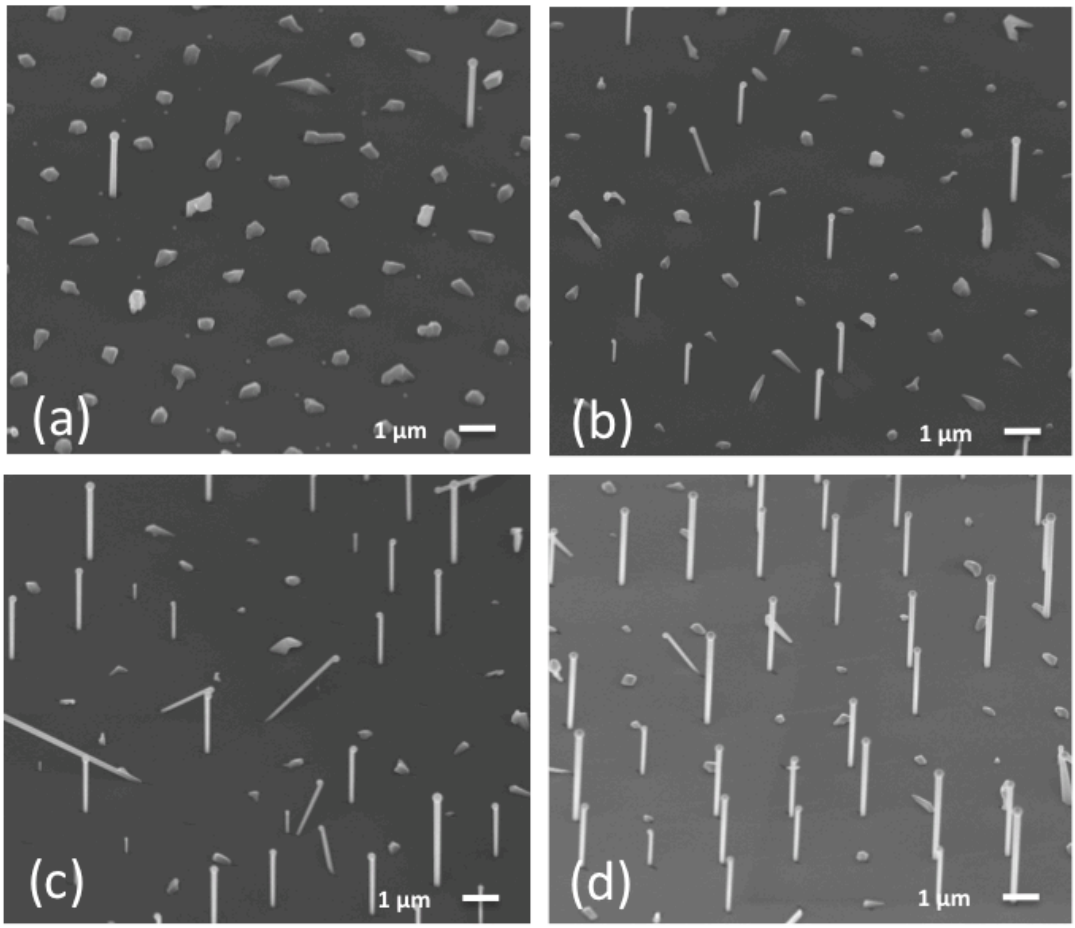

Figure 5.3 Scanning electron microscope (SEM) images of GaAs core NWs on Si (111) at (a) T_{sub} = 630 °C, (b) T_{sub} = 650 °C, (c) T_{sub} = 670 °C, (d) T_{sub} = 690 °C. Ga flux was set at 0.7 monolayer/s, growth time = 20 min.

Table 5.2 SAG yield under different growth substrate temperature

Sample	Substrate Temp (°C)	Yield
T630	630	~1%
T650	650	~3%
T670	670	~23%
T690	690	~62%

5.3.4 Growth of GaNAs shell

Core-shell growth is a very intriguing topic for NW applications as it not only adjusts the NW diameter but also permits the growth of an advanced structure by radial composition and doping modulation, such as p-i-n lateral junction and lateral quantum wells. The absorption and solar cell efficiency could be tuned by adjusting the thickness of different layers of core-shell NWs.

With the optimization of the GaAs NW core growth, we proceeded to the dilute nitride shell growth. For GaAs/GaNAs core/shell NWs, the T_{sub} for the shell growth was decreased to ~500 °C. Decreasing T_{sub} reduces Ga adatom mobility on the growing surfaces and depletes the NW tip from a liquid Ga droplet to cease the axial NW growth. However, the Ga shutter was closed while ramping down the growth temperature for 20 min and keeping the group V flux to consume the Ga droplets prior to the growth of the GaNAs shells. The Ga flux was kept at 0.7 monolayer/s. The N plasma power condition for the shell was 0.9 sccm and 250 W, and the shell growth time was 30 min. Figure 3 shows a SEM image of the core-shell GaAs/GaNAs NWs. The average diameter of

core-shell NWs is ~220 nm. Figure 5.4 shows the SEM images of the core-shell GaAs/GaNAs NWs. The core-shell NW array has uniform morphology with smooth sidewalls. The SiO_2 substrate is covered by amorphous GaNAs grown during shell growth. The core-shell NWs also show hexagonal shape. Each parallel sidewall is aligned normal to one of the three equivalent <110> directions.

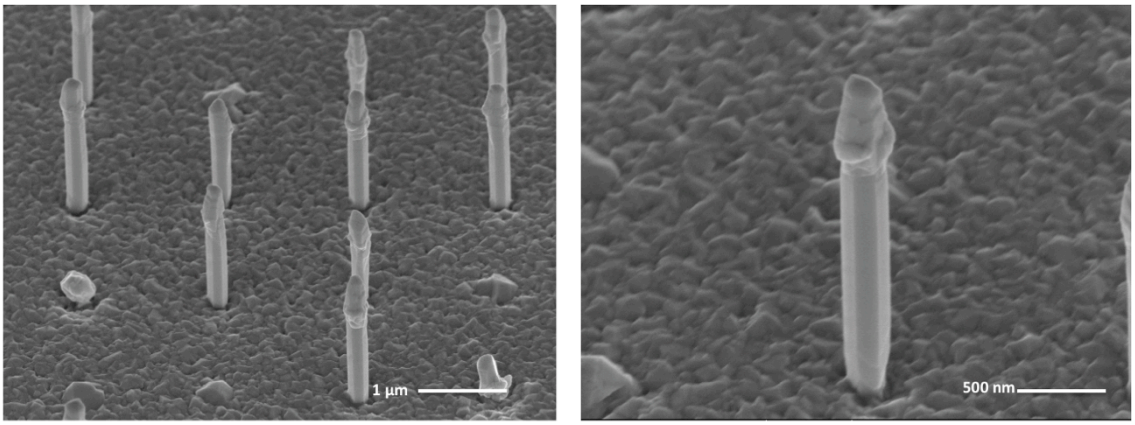

Figure 5.4 (a) SEM image of GaAs/GaNAs core-shell NWs. (b) SEM image of single core-shell NW

5.4 Characterization

5.4.1 Optical Characterization

Figure 5.5 (a) shows a µ-PL spectrum of the core-shell NW. µ-PL measurement was carried out on as-grown NW arrays with excitation from a 659 nm solid-state laser source at 6K. The excitation beam was focused on the sample using a 50X objective (NA=0.5). The excitation power was 1 mW. The signal was dispersed using a

monochromator equipped with a 950 mm^{-1} grating and detected with a liquid nitrogen cooled InGaAs CCD. Figure 5.5 (b) shows a μ-PL spectrum of the core-shell NWs (the solid line) together with the reference GaAs NWs (the dashed line). The spot diameter of the m-PL laser beam focused on the sample is estimated to be 0.8 - 1mm. That means the PL-spectra came from one or two NWs. The m-PL spectrum of the reference sample is dominated by a single line at around 1.52 eV, likely due to free exciton (FE) recombination. The lack of other transitions in the spectra indicates very good structural and optical quality of the sample, consistent with the results of TEM measurements to be discussed below. For the GaAs/GaNAs core-shell NW, the PL spectra contain two dominant emission bands peaking at 1.45 and 1.17 eV. The former could be attributed to the GaAs core based on performed photoluminescence excitation (PLE) measurements (Figure 5.5(b)). We note that the GaAs emission in the core-shell structures is no longer dominated by the FE transitions, which could reflect fast FE trapping by the shell with a lower bandgap. Instead, it contains a broader PL band, which likely arises from radiative transitions involving residual impurities or defects formed due to the strain in the core-shell structure. The second PL band is due to emission from the GaNAs shell and arises from recombination of weakly localized excitons, which are trapped by potential fluctuations induced by long-range alloy disorder in the GaNAs shell.[12] The numerous fine features overlapping with the broad peak could be attributed to excitons strongly confined in quantum-dot like states induced by short-range fluctuations in nitrogen composition that are superimposed on long-range alloy disorder.[13] These PL bands could

be attributed to the GaAs core and GaNAs shell, respectively. The third peak at around 0.93 eV may be caused by N related defects, which is often seen in dilute nitride materials. [14, 15] Figure 5.5 (c) shows the relationship between N composition and bandgap energy (eV) based on the calculation from the band anti-crossing (BAC) model. The X-axis represents composition of nitrogen in GaNAs alloy and Y-axis represents the corresponding bandgap. From PLE spectra detected from GaAs/GaNAs core-shell NWs in Fig 5.5 (b) we conclude that the bandgap of GaNAs shell is about 1.32 eV, therefore the N composition in the shell is estimated to be ~0.8%.

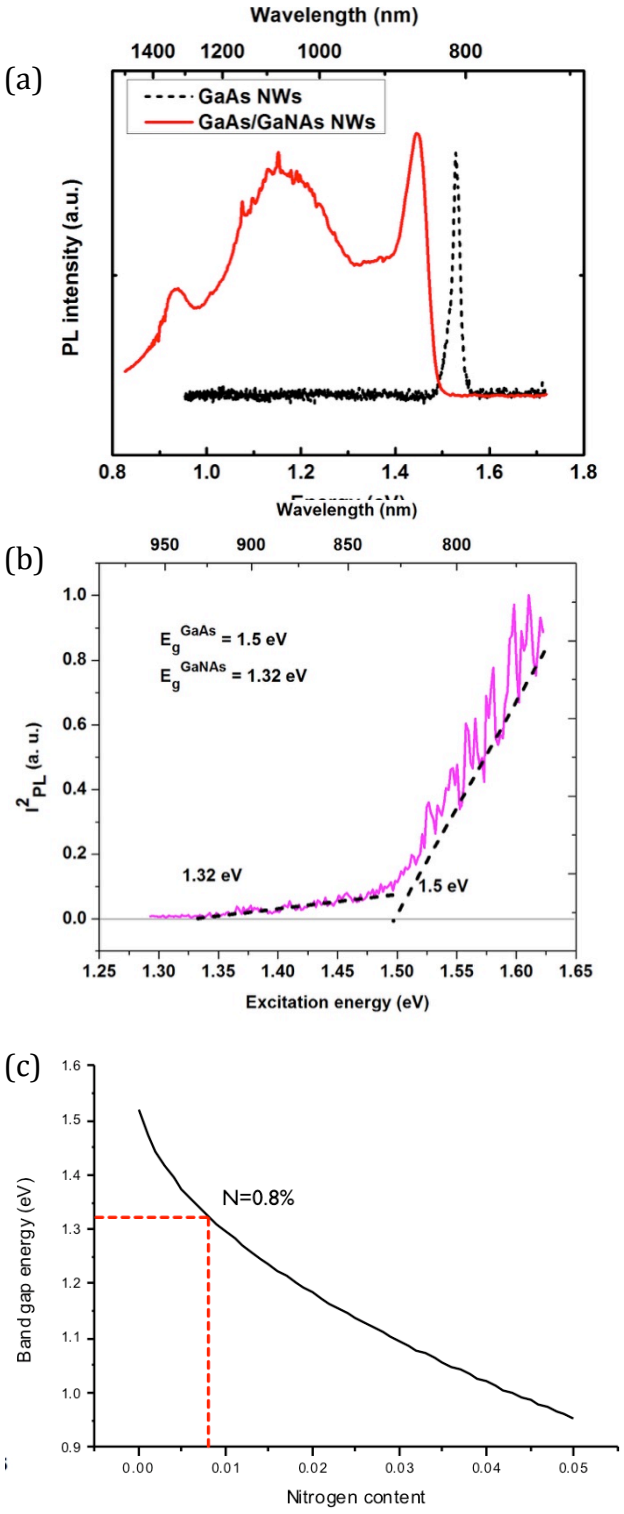

Figure 5.5 (a) μ-PL spectra of the GaAs NWs and GaAs/GaNAs NWs measured under 659 nm excitation. (b) PLE spectrum detected from the GaAs/GaNAs core-shell NWs, plotted as the square of the PL-intensity (I_{PL}) (c) Calculated bandgap energy of GaNAs vs nitrogen content by the band anti-crossing model.

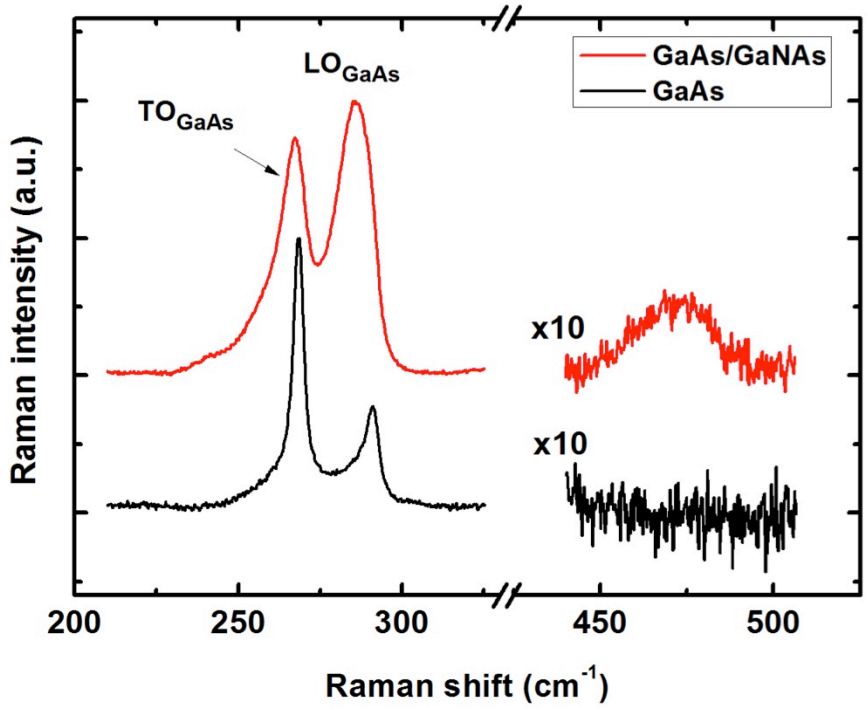

Figure 5.6 μ-Raman spectra acquired in the backscattering geometry along the [111] direction from GaAs and GaNAs NWs. The spectra are normalized to the intensity of the LO GaAs mode and are shifted vertically for clarity

To obtain evidence of N incorporation in the NWs, and also to get further insight into the crystalline quality of the GaNAs alloy, μ-Raman spectroscopy was performed. Figure 5.6 shows μ-Raman spectra acquired from a single GaAs NW and GaAs/GaNAs NW, which were performed with the excitation and detection paths along the [111] crystallographic direction. In this geometry, scattering involving zone-center longitudinal optical (LO) and transverse optical (TO) phonons is allowed from the μ-Raman selection rules. The detected μ-Raman spectra are characteristic for zincblende GaAs, as the formation of the wurtzite phase should cause the appearance of an additional optical mode. The appearance of an additional local mode representing vibrations of the Ga-N was observed from μ-Raman spectra.

5.4.2 TEM measurements.

We then studied the interface of the selective area grown GaAs NW and GaAs/GaNAs core/shell NW with the Si substrate using TEM. To prepare the samples for TEM, we first deposited a 200 nm-thick SiO_2 layer by PECVD and then deposited by in-situ focused ion beam (FIB) a Pt protection layer. Second, careful FIB slicing at the GaAs NW growth site from the Si substrate was performed. The sample was then mounted by a controlled manipulator inside the FIB to a TEM grid and was further thinned to an e-beam transparent lamella thickness of 80 - 120 nm. An overall view of the studied GaAs NW is shown in Figure 5.7(a) where the NW grows from the SiO_2 hole and increases diameter above the hole to overlap its edge. Overall, we found that the GaAs NW grown on the Si substrate at 690 °C exhibited the zincblende crystal structure [Figure 5.7(b)-(d), Figure 5.7(f)] and was relatively free of defects except for a few twinning planes observed in the hole and near the base of the NW. These twinning planes are commonly observed for III-V semiconductor NWs due to the small energy difference between the zincblende (ZB) phase and the hexagonal wurtzite (WZ) phase[16]. In addition to the free NW surface that helps in stress relief, the stepped morphology of the GaAs NW at the SiO_2 mask at the base is expected to significantly lower the strain near the base of the GaAs nanowire thereby minimizing the formation of edge dislocations and twin boundaries at the GaAs/Si heterointerface (Figure 5.7d) [17]. On a stepped interface, there are atoms at the edges that can be dislocated from their pre-supposed position on a

flat interface. These atoms at multiple edges can adapt to strain and the interfacial in-plane strain is supposed to reduce and be accommodated. The strain distribution was calculated by manually measuring atomic distances at different locations near the Si/GaAs interface in Figure 5.7(d). According to the strain distribution analysis in Figure 5.7(e), the in-plane strain ($\varepsilon_{\parallel}$) in the Si substrate at 1.2 nm from the interface is 1.3%, and the in-plane strain ($\varepsilon_{\parallel}$) in the GaAs core at 1.2 nm from the interface is -1.7%. The in-plane strain ($\varepsilon_{\parallel}$) and out-of-plane strain ($\varepsilon_{\perp}$) in Si decreases gradually to nearly 0 at 12 nm from the interface. Of note is the stepped diameter before, at, and after the planar twinned layer near the base as shown in Figure 5.7(f). Recent in-situ TEM growth of GaAs NWs concludes that their phase is dictated by the dynamics of the catalyst volume and contact angle at the edge of the NW.[18] The change of Ga droplet volume during the growth affects the phase of crystal and consequently the diameter of NWs.

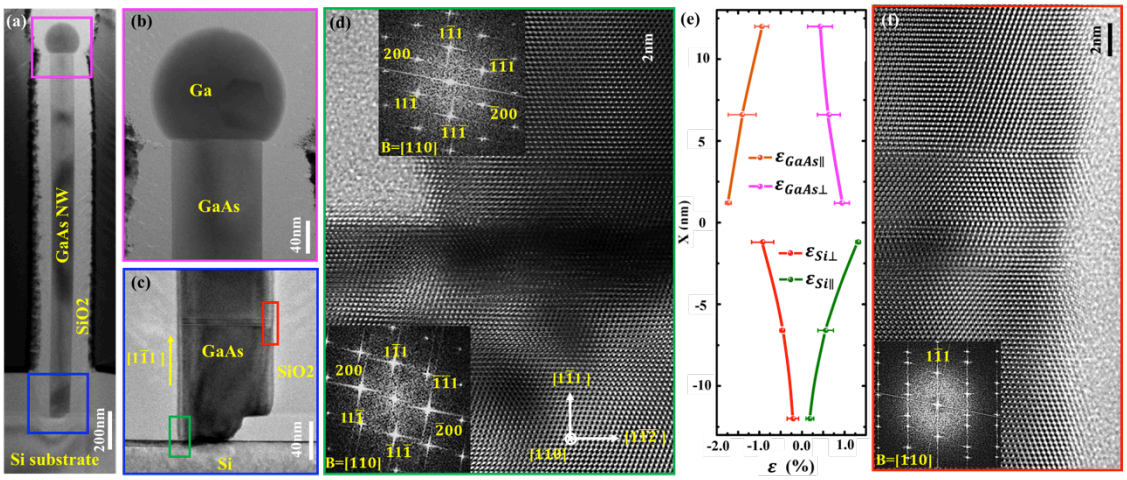

Figure 5.7 (a) TEM image of an overview of a GaAs NW on Si substrate. (b) High-magnification TEM image of the tip of the GaAs NW. (c) High-magnification TEM image of the bottom of the GaAs NW on Si substrate. (d) High-Resolution TEM (HRTEM) image of the interface of GaAs NW and Si substrate indicated by the green rectangle in (c). (e) The strain distribution at the interface of GaAs NW and Si substrate. (f) HRTEM image of a part of the NW near the base indicated by the red rectangle in (c) showing the twinning planes in GaAs NW. The insets in (d) and (f) show Fast Fourier Transform (FFT) of the crystal in respective regions.

It is imperative to study the interfaces of the GaNAs shells on GaAs NWs. Figure 5.8(a) shows an overall TEM image view of a GaAs/GaNAs core-shell NW grown on the Si substrate. Defective growth at the tip of the NW is observed in Figure 5.8(b) indicating that the Ga droplet was not fully depleted prior to the GaNAs shell growth. The magnified image of the NW base in Figure 5.8 (c) reveals that the parasitic GaNAs is grown on the SiO_2 pattern at ~500 °C substrate temperature with a thickness of ~200 nm. The catalyzed growth on the SiO_2 surface is about 4 times thicker than that on the NW sidewalls which were ~ 55 nm. The strain between GaAs and GaNAs on the sidewall was estimated to be ~0.18 % for an expected nitrogen concentration of 0.8% in these experiments.[19] Using the Matthews and Blakeslee force balance for strain relaxation, the

critical thickness of planar GaNAs containing 0.8% nitrogen on GaAs was calculated to be ~180 nm.[20] Core/shell nanowires are known to have a larger critical thickness for strain relaxation compared to planar layers.[21] Thus, the boundary between GaAs and GaNAs is not obvious in the TEM image. Interestingly, we found that GaNAs filled laterally the empty space in the patterned hole and epitaxially grew on the Si (111) surface as observed in Figure 5.8(d) – (g). The HRTEM images at the Si/GaNAs interface did not reveal evident defects except for the planar twinned layers within the GaAs/GaNAs core/shell NW. We suspect that these planar defects also help in relieving the ~ 4% GaAs/Si lattice mismatch, in addition to the free surface. Future work will concern with the optimization of the shell growth conditions and Ga depletion from the NW tip to enable an epitaxial defect-free core/shell tip that is crucial for light absorption or emission.

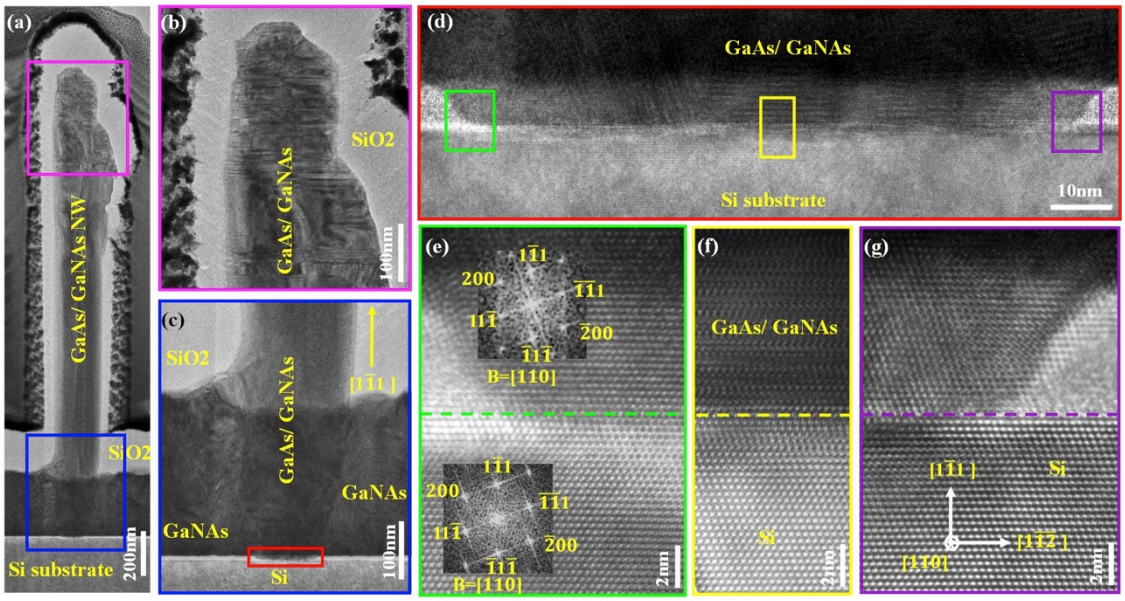

Figure 5.8 (a) TEM image of an overview of a GaAs/GaNAs core-shell NW on Si substrate. (b) High-magnification TEM image of the tip of the GaAs/GaNAs core-shell NW. (c) High-magnification TEM image of the bottom of the GaAs/GaNAs core-shell NW on Si substrate. (d) HRTEM image of the interface of the GaAs/GaNAs NW and Si substrate. (e), (f) and (g) HRTEM images of the interface of GaAs/GaNAs NW and Si, respectively, green, yellow and purple rectangles in (d). The inset in (e) and (g) shows selected-area diffraction pattern.

5.5 Conclusion

In conclusion, vertical self-catalyzed GaAs NWs and GaAs/GaNAs core-shell NWs were grown on patterned Si (111) substrate by GSMBE. Typical diameters are ~110 nm for GaAs NWs and ~220 nm for GaAs/GaNAs core-shell NWs for a 30 min shell growth time. The yield of vertical NW growth increased with optimal wet etching of the native oxide layers and at higher growth temperatures with the best result obtained at 690 °C. GaNAs shells were grown and maintained an epitaxial interface with both the Si substrate and the GaAs NW core deduced from detailed HRTEM studies.

5.6 Acknowledgment

This chapter, in part, has been published in "Self-catalyzed core-shell GaAs/GaNAs nanowires grown on patterned Si (111) by gas-source molecular beam epitaxy", Rui La, Ren Liu, Weichuan Yao, Renjie Chen, Mattias Jansson, Janet L. Pan, Irina A. Buyanova, Jie Xiang, Shadi A Dayeh, Charles W. Tu, Appl. Phys. Lett., 111, 072106 (2017). The dissertation author was the primary investigator and author of this paper. The work was performed in part at the San Diego Nanotechnology Infrastructure (SDNI) of UCSD, a member of the National Nanotechnology Coordinated Infrastructure, which is supported by the National Science Foundation (Grant ECCS-1542148). The TEM work was performed at the Center for Integrated Nanotechnologies (CINT), U.S. Department of Energy, Office of Basic Energy Sciences User Facility at Los Alamos National Laboratory (Contract DE-AC52-06NA25396) and Sandia National Laboratories (Contract DE-AC04-94AL85000). Optical characterization at Linköping University was supported in part by the Swedish Energy Agency (grant # P40119-1) and the Swedish Research Council (grant # 2015-05532).

Reference

[1]M. Yao, N. Huang, S. Cong, C. Chi, M. A. Seyedi, Y. Lin, Y. Cao, M. L. Povinelli, P. D.

Dapkus and C. Zhou, Nano Lett. 14, 3293 (2014)

[2]J. Wallentin, N. Anttu, D. Asoli, M. Huffman, I. Aberg, M. H. Magnusson, G. Siefer,
[3]K. Tomioka, P. Mohan, J. Noborisaka, S. Hara, J. Motohisa and T. Fukui, J. Cryst. Growth 298, 644 (2007).

[4]E. Nakai, M. Yoshimura, K. Tomioka and T. Fukui, Jpn. J. Appl. Phys. 52, 055002 (2013)

[5]S. Assali, I. Zardo, S. Plissard, D. Kriegner, M. A. Verheijen, G. Bauer, A. Meijerink, A. Belabbes, F. Bechstedt, J. E. M. Haverkort, and E. P. A. M. Bakkers, Nano Lett. 13, 1559 (2013).

[6]K. Ikejiri, T. Sato, H. Yoshida, K. Kiruma, J. Motohisa, S. Hara and T. Fukui, Nanotechnology 19, 26 (2008).

[7]M. Bar-Sadan, J. Barthel, H. Shtrikman and L. Houben, Nano Lett. 12, 2352 (2012).

[8]Y. Wang, V. Schmid, S. Senz and U. Gosele, Nat. Nanotechnol. 1, 186 (2006).

[9]S. Plissard, G. Larrieu, X. Wallart and P. Caroff, Nanotechnology 22, 275602 (2011).

[10]G. S. Higashi, Y. J. Chabal, G. W. Trucks and K. Raghavachari, Appl. Phys. Lett. 56, 656 (1990)

[11]C. Colombo, D. Spirkoska, M. Frimmer, G. Abstreiter, and A. Fontcuberta I Morral, Phys. Rev. B 88, 155326 (2008).

[12]S. L. Chen, S. Filippov, F. Ishikawa, W. M. Chen and I. A. Buyanova, Appl. Phys. Lett. 105, 253106 (2014).

[13]S. Filippov, M. Jansson, J.E. Stehr, J. Palisaitis, P. O. A. Persson, F. Ishikawa, W. M. Chen, and I. A. Buyanova, Nanoscale, 8, 15939, (2016)

[14]P. K. Kasanaboina, E. Ahmad, J. Li, C. L. Reynolds, Jr., Y. Liu, and S. Iyer, Appl. Phys. Lett. 107, 103111 (2015).

[15]Y. J. Kuang, S. Chen, H. Li, S. K. Sinha, and C. W. Tu, J. Vac. Sci. Technol., B 30, 02B121 (2012).

[16]S. Sukrittanon, Y.J. Kuang, and C. W. Tu, J. Vac. Sci. Technol. B 31, (2013).

[17]R. Chen, and S. A. Dayeh, Nano Lett. 15, 3770, (2015).

[18] D. Jacobsson, F. Panciera, J. Tersoff, M. C. Reuter, S. Lehmann, S. Hofmann, K. A.

[19]W. Li, and M. Pessa, Appl. Phys. Lett., 78, 2864, (2001).

[20]J. W. Matthews, A. E. Blakeslee, J. Cryst. Growth, 27, 118, (1974).

[21]S. A. Dayeh, W. Tang, F. Boioli, K. L. Kavanagh, H. Zheng, J. Wang, N. H. Mack, G. Swadener, J. Y. Huang, L. Miglio, K. N. Tu, S. T. Picraux, Nano Lett., 5, 1869, (2013).

Chapter 6

Fabrication of single nanowire solar cell

6.1 Overview

Nanostructured materials have been explored as components of photovoltaic (PV) in an effort to improve efficiency[1]. There are several key advantages of using single nanowire (NW) as photovoltaic element[2]. First of all, the bottom-up method of nanowire grown on substrate allows precise control of key parameters, which will determine solar cell performance, including dopent composition, diode junction structure, size and morphology. Second, single NW solar cell device could be seamlessly integrated with

conventional electronic devices to provide energy for low-power application. Thirdly, studies of PV properties as the single NW level will determine the limits, area of improvement, and potential benefits of NW solar cell. Therefore, investigation of single NW solar cell is the first step to study large scale NW solar cell on silicon. This chapter is devoted to the fabrication of single NW solar cells, including the process to create metal contact markers, the reactive ion etching (RIE) process to expose the core of NWs, the wet etch technique to smooth the rough sidewalls of NWs, and metal contact lines to connect NW with measurement circuits.

6.2 GaNP/GaNP/GaNP core-shell-shell NWs

Improving the efficiency of III-V nanowire compound semiconductor solar cells can be achieve by stacking different junctions to the cell structure or through the lowering of cost by replacing the expensive III-V substrate with silicon. However, integrating III-V compound with silicon substrate requires overcoming lattice mismatch and thermal expansion coefficient mismatch. The small contact interface between NWs and Si substrate could accommodate the lattice mismatch and relax the strain within the first few monolayers, which is discussed in the Chapter 5.4.2. In addition, a sparse array of NWs can absorb almost all-incoming light, which can significantly improve efficiency of solar cells[3].

The material we used in this chapter is GaNP/GaNP/GaNP core-shell-shell pin junction NWs. The growth condition is similar to that of growing GaAsP/GaNAsP

core-shell NWs. Prior to growth, the Si (111) substrate was dipped in an HF solution for 10 seconds to remove the intrinsic oxide, and then it was rinsed with deionized (DI) water. The substrate was then loaded into the MBE load-lock chamber. In the growth chamber, the substrate was heated to ~710 °C for 15 minutes for thermal cleaning, and then the substrate temperature was decreased to the growth temperature.

For NW growth, Ga atoms were deposited on the Si (111) surface for one minute with a Ga flux of ~ 0.7 monolayer/s, calibrated by Ga-induce reflection high-energy electron diffraction (RHEED) intensity oscillations for the planar growth of GaP under the same substrate temperature (T_{sub}). Solid elemental Ga was used to generate a Ga beam, and solid Si was used as the n-type dopant. Then, the substrate was annealed for 30 s to form Ga droplets on the surface. Growth started by opening the Ga and Si shutters and injecting PH_3 into the growth chamber to initiate growth of GaNP nanowires, after 90 seconds of growth, RF N plasma is then ignited, and the GaNP nanowires were grown for 15 minutes with a V/III ratio of ~2.5. Then, the substrate temperature was decreased to 500 °C and the intrinsic GaNP shells were grown for 15 minutes. Finally, the Be shutter was opened to complete 15 minutes of p-GaNP shell layer growth. The average diameter and length of the nanowires are 210 ± 4 nm and 2.3 ± 0.2 μm, respectively. After the shells were grown, the average diameter increased by ~160% with no significant increase in length. This confirms that lowering T_{sub} can suppress axial growth, and, instead, promote radial growth.

PL measurement was carried out for optical studies. Figure 6.1(a) shows the

SEM image of p-i-n GaNP NWs. Figure 6.1(b) shows the PL measurements at 300 K, performed on p-i-n GaNP core-shell NWs. The PL emission shows single PL peaks at 1.96 eV. The single PL peak of core-shell NWs shows that the distribution of nitrogen in NWs is uniform. The estimated [N] is approximately at 1.8% based on PL emission.

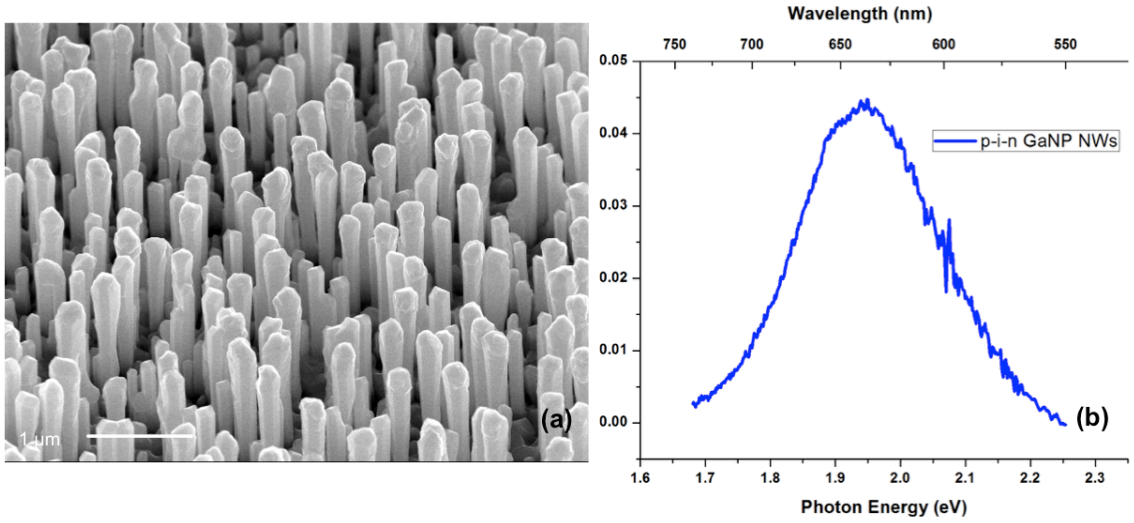

Figure 6.1 (a) SEM image of p-i-n GaNP core-shell-shell NWs. (b) PL spectra of p-i-n GaNP core-shell-shell NWs

6.3 Fabrication process

Single NW solar cell (SNWSC) devices were fabricated on a SiO_2/Si substrate. Figure 6.2 shows a detailed schematic of the SNWSC fabrication methodology. Initially, the wires were removed from the growth substrate by sonication in isopropanol and drip dried onto highly p-doped Si (111) substrates covered with 100 nm-thick thermal SiO_2 and pre-fabricated alignment masks. Poly(methyl methacrylate) (PMMA) was deposited by spin-coating, and dried on a hot-plate at 180 °C for 1.5 minutes. Patterns were developed by exposing the samples to light under a mask, and followed by a lift-off

process. The contact to the n-doped core was defined using e-beam lithography followed by 1 minute dry etching and 30 °C wet etching in $HCl:H_2O_2:H_2O$ (1:1:1) to expose the core and for subsequent e-beam evaporation of 50 nm Cr/ 150 nm Au. The contact to the p-doped wire surface was defined using e-beam lithography followed by a 5s B-HF etch to remove oxide and quick loading into the evaporation chamber. The bilayer contact 50 nm Ge/150 nm Au was deposited by e-beam evaporation. The lift-off process was carried out in acetone for 10 hours. Using this process, we have developed SNWSC devices with different contacts attached to it. Figure 6.3 shows a fabricated SNWSC after metallization.

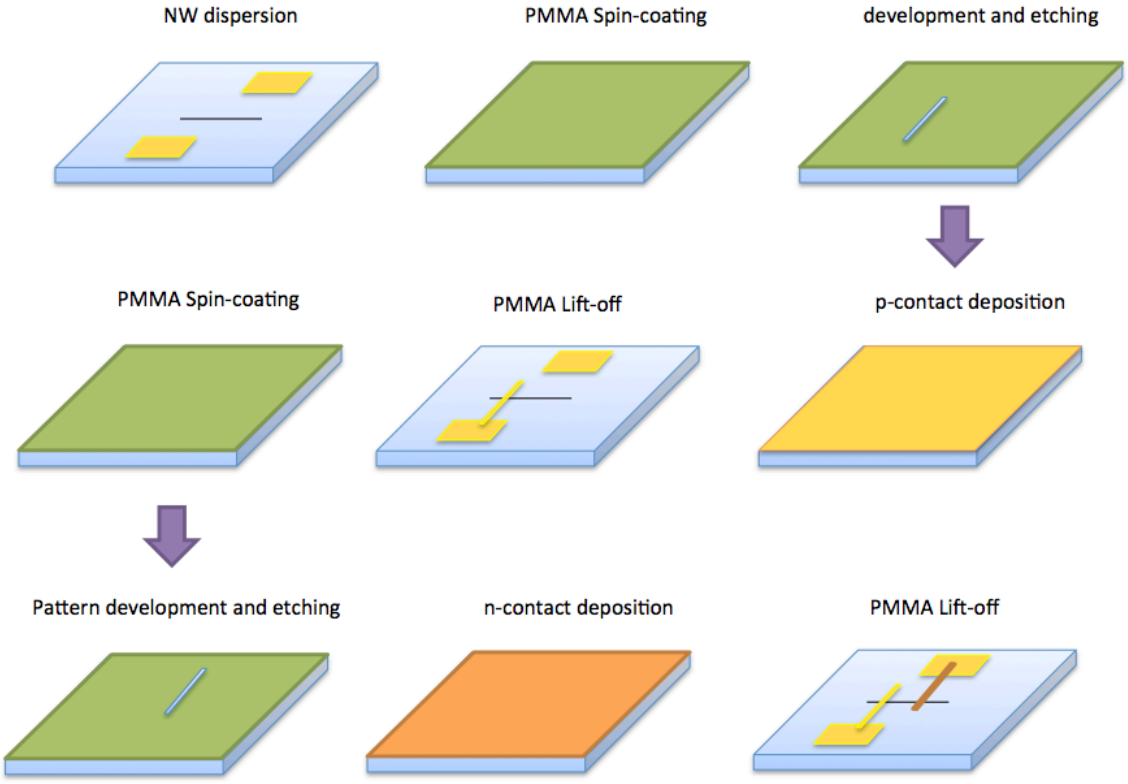

Figure 6.2 Schematic plot of the SNWSC fabrication process

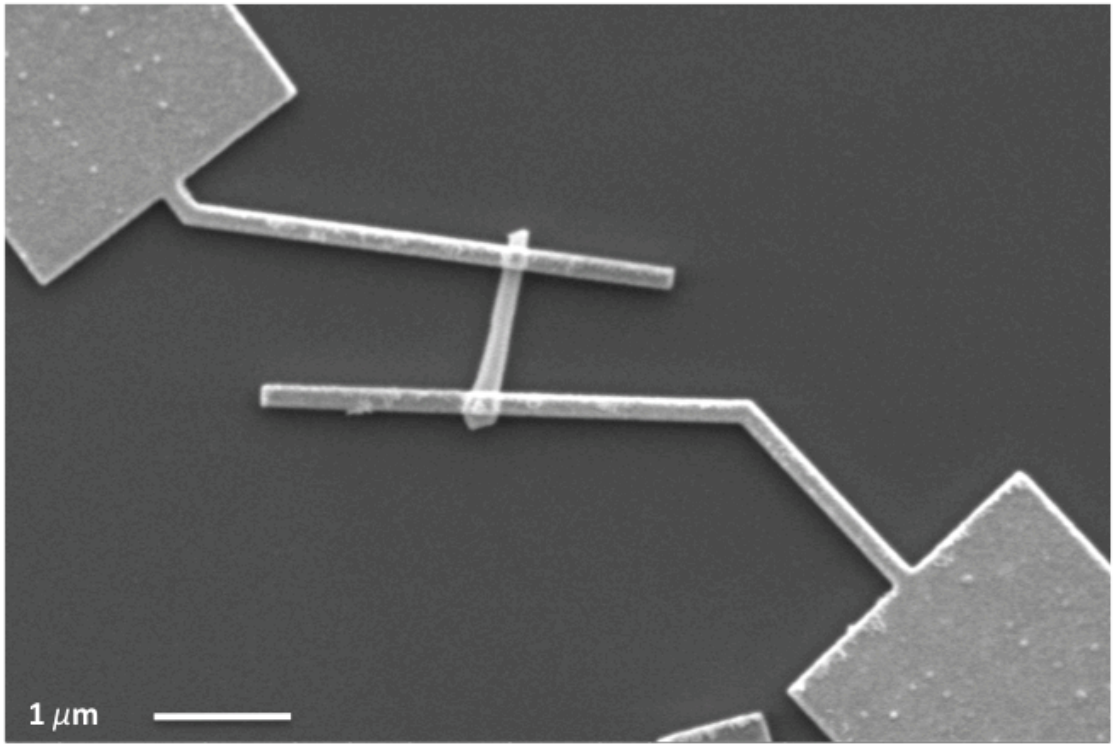

Figure 6.3 top view SEM image of fabricated SNWSC.

Different fabrication parameters were adjusted during the experiment to optimize the process. In dry etching, a combination of Cl_2 and BCl_3 was selected as the main etching gases. Etching is achieved in two ways: (a) a chemical process in which Cl_2 and BCl_3 are excited and produce reactive Cl atoms, which react promptly on the nanowire surface; (b) a physical process in which the surface of the sample is bombarded by ions that are also produced in the plasma[4]. In our experiment, the reactive ion etching (RIE) process was performed in an Oxford Plasmalab 80 equipment with a 13.56 MHz RF source at room temperature. To avoid over-etching, different etching times under the same gases condition were investigated. Figure 6.4 shows NW after 1 minute, 2 minutes and 3 minutes of etching. Both 2 minutes and 3 minutes etching images show damage to

the core NW. In order to expose the core NWs as much as possible and also not damage the core, the one-minute of etching condition was selected as the optimal condition.

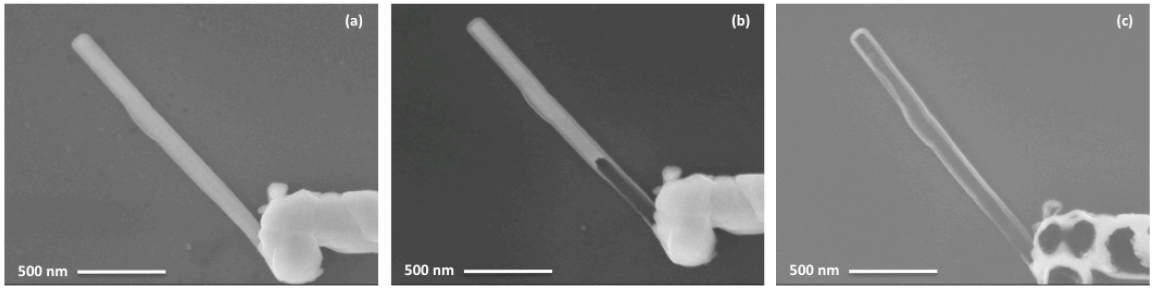

Figure 6.4 SEM images of morphology of the etched sample after (a) 1 minute, (b) 2 minutes, and (3) 3 minutes dry etching

6.4 Performance simulation

The standard test condition for a solar cell is air mass 1.5 global (AM 1.5G) spectrum, which defines the power of incident light as 100mW/cm^2. There are several key parameters of a solar cell: (1) short circuit current density (J_{sc}), which is the current density when the voltage across the cell is zero, (2) open circuit voltage (V_{oc}), which is the maximum voltage of the operation region of the cell, and (3) current density (J_m) and voltage (V_m) that result in the solar cell's maximum power density and correspond to its fill factor (FF) and solar cell efficiency (η).

The short-circuit current through the device junction can be solved by using the semiconductor transport equations and Poisson's equation with appropriate boundary conditions. In the calculation, we assume that there are no free carriers in the depletion region and only the minority carriers determine the current. In this simulation, we use a p-i-n junction for our solar cell. The p-region and n-region are employed as emitter and

base, and their doping concentrations are 5×10^{17} and 3×10^{18} cm^{-3} respectively. To simplify the model, we treat the nanowire as two symmetric thin films with the same dimensions. The thickness of p, i, and n regions are 40 nm, 35 nm and 35 nm, respectively. The short circuit current can be calculated using the following equation:[5]

$$j_{sc}(E) = j_e(E) + j_b(E) + j_{i,gen}(E) \tag{6.1}$$

$$J_{sc} = \int_0^\infty j_{sc}(E)\, d(E) \tag{6.2}$$

where j_e and j_b are the minority carrier current densities from the emitter and the base, respectively, and $j_{i,gen}$ is the current density generated in the i-region. Each current density is given by:

$$j_e(E) = \left[\frac{qb_s(1-R)\alpha L_e}{\alpha^2 L_e^2 - 1}\right] \times \left[\frac{\left(\frac{S_e L_e}{D_e} + \alpha L_e\right) - e^{-\alpha W_e}\left(\frac{S_e L_e}{D_e}\cosh\frac{W_e}{L_e} + \sinh\frac{W_e}{L_e}\right)}{\frac{S_e L_e}{D_e}\sinh\frac{W_e}{L_e} + \cosh\frac{W_e}{L_e}} - \alpha L_e e^{-\alpha W_e}\right] \tag{6.3}$$

$$j_b(E) = \left[\frac{qb_s(1-R)\alpha L_b}{\alpha^2 L_b^2 - 1}\right] \times \left[\frac{\left(\frac{S_b L_b}{D_b} + \alpha L_b\right) - e^{-\alpha W_b}\left(\frac{S_b L_b}{D_b}\cosh\frac{W_b}{L_b} + \sinh\frac{W_b}{L_b}\right)}{\frac{S_b L_b}{D_b}\sinh\frac{W_b}{L_b} + \cosh\frac{W_b}{L_b}} - \alpha L_b e^{-\alpha W_b}\right] \tag{6.4}$$

$$J_{i,gen}(E) = qb_s(1-R)e^{-\alpha W_e}(1 - \alpha e^{-\alpha W_i}) \tag{6.5}$$

where b_s is incident spectral photon flux density; R is the reflectance of the material; α is the absorption coefficient of the material; L_e and L_b are the diffusion length of minority carriers in the emitter and the base regions, respectively; S_e and S_b are the recombination velocities at the front and the back surface, respectively; and D_e and D_b are the diffusion coefficients of minority carriers in the emitter and the base regions, respectively.

The short circuit current can be calculated by:

$$J_{sc} = q \int b_s(E) EQE(E)\, d(E) \tag{6.6}$$

where EQE is external quantum efficiency, which is the ratio of the number of electrons collected at the terminals of the cell to the number of incident photons. EQE is given by

$$EQE = \frac{j_e(E) + j_b(E) + j_{i,gen}(E)}{q b_s(E)} \tag{6.7}$$

To get the efficiency of solar cell, the open circuit voltage is firstly calculated as the maximum possible potential across the terminals of the solar cell at J = 0.

$$V_{oc} = \frac{n k_B T}{q} \ln\left(\frac{J_{sc}}{J_0} + 1\right) \tag{6.8}$$

J_0 is dependent on the minority carrier diffusion current of the emitter and base region as well as the recombination current of the depletion region.

$$J_0 = J_{0,e} + J_{0,b} + J_{0,rec} \tag{6.9}$$

where

$$J_{0,e} = \left[\frac{q D_e N_C N_V}{L_e}\right] \times \left[\frac{\left(\frac{S_e L_e}{D_e} cosh\frac{W_e}{L_e} + sinh\frac{W_e}{L_e}\right)}{\frac{S_e L_e}{D_e} sinh\frac{W_e}{L_e} + cosh\frac{W_e}{L_e}} - e^{\frac{-E_g}{k_B T}}\right] \tag{6.10}$$

$$J_{0,b} = \left[\frac{q D_b N_C N_V}{L_b}\right] \times \left[\frac{\left(\frac{S_b L_b}{D_b} cosh\frac{W_b}{L_b} + sinh\frac{W_b}{L_b}\right)}{\frac{S_b L_b}{D_b} sinh\frac{W_b}{L_b} + cosh\frac{W_b}{L_b}} - e^{\frac{-E_g}{k_B T}}\right] \tag{6.11}$$

$$J_{0,rec} = q W_i \times \sqrt{\frac{N_C N_V}{t_e t_b}} \times e^{\frac{-E_g}{k_B T}}] \tag{6.12}$$

With the equation for the short circuit current and open circuit voltage, we perform simulation on our p-i-n GaNP structure. The Python code used in calculation are

shown in Appendix A. The default parameters used for this structure are listed in Table 6.1.

Table 6.1 Parameters used in our simulation.

General parameters	
Bandgap (Eg)	1.96 eV
Effective conduction band density of states (Nc)[6]	$1.8 \times 10^{19}19$ cm^{-3}
Effective valence band density of states (Nv) [6]	1.9×10^{19} cm^{-3}
Core (n-type)	
Doping concentration (N_D)	3×10^{18} cm^{-3}
Diameter of core	40 nm
Diffusion coefficient of minority carriers(D_b)[7]	1.68 cm^2/s
Diffusion length of minority carriers (L_b)[7]	190 nm
Shell 1 (Intrinsic layer)	
Thickness of i-layer	35 nm
Shell 2 (p-type)	
Doping concentration (N_A)	5×10^{17}
Thickness of p-layer	35 nm
Diffusion coefficient of minority carriers (D_e)[7]	1.53 cm^2/s
Diffusion length of minority carriers (L_e)[7]	4100 nm
Dielectric constant (zincblende structure)	11.01 (300K)

Since the diameter of core nanowire is a constant, the effect of various intrinsic layer thickness and outer-shell-p layer thickness are studied. Figure 6.5 shows simulated solar cell short circuit current of p-GaNP/i-GaNP/n-GaNP NW solar cell with different i-layer thickness (W_i) and emitter layer thickness (W_e).

As can be seen in the figure, increasing W_i increases short circuit current for the solar cells. This is because more absorption of light and generation of electron hole

pairs in intrinsic layer. The short circuit current is relatively independent of emitter layer thickness. In our structure, the thickness of emitter (W_e) is smaller than the diffusion length (L_e). Utilizing a thinner emitter layer ($W_e < L_e$) will have less recombination in emitter layer, thus the generated carriers can transport across the junction with less loss, resulting in improved J_{sc} as shown in Figure 6.5 In our simulation, the thicknesses of intrinsic (W_i) and emitter (W_e) layers are varied from 10 nm to 100 nm. We assume 100% collected electron-hole pairs generated by photons. Also, absorption of GaNP material respect to various wavelengths is taken account of during simulation.

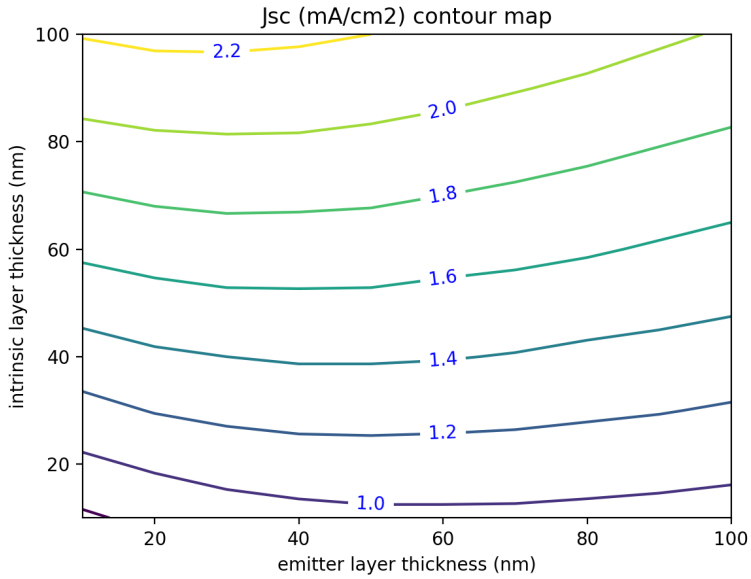

Figure 6.5 Maximum short circuit current density as a function with various intrinsic layer thicknesses and emitter layer thickness

Figure 6.6 shows maximum efficiency of our GaNP solar cell under one sun. We assume AM 1.5G and take absorption coefficients of GaNP into account during simulation. The simulated value of J_{sc} is used in combination with V_{oc} simulated from radiative recombination only model[7] to calculate the maximum efficiency. In radiative

recombination only model, the bandgap-open circuit voltage offset (W_{oc}) is around 0.4V. Using E_g = 1.96 eV from our PL measurement, our GaNP solar cell is capable of providing a maximum J_{sc} and efficiency of 1.27 mA/cm^2 and 1.8%, respectively.

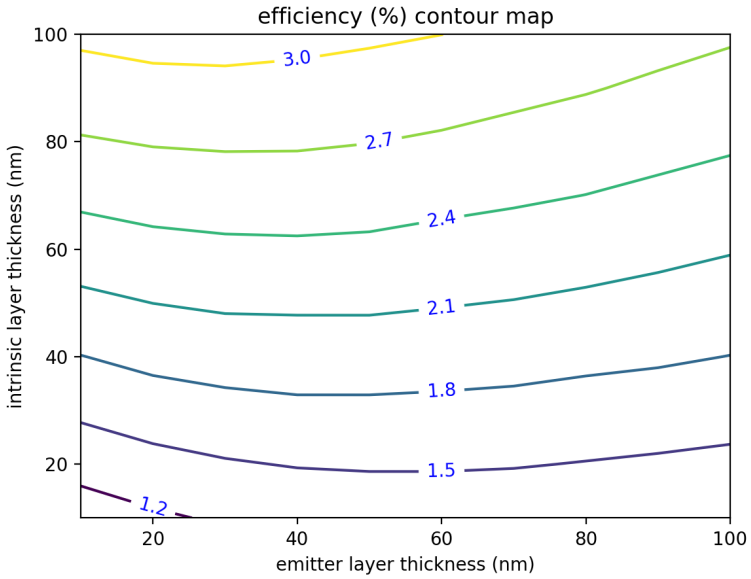

Figure 6.6 Maximum solar cell efficiency as a function with various intrinsic layer thicknesses and emitter layer thickness

6.5 Current-voltage characteristic

Current-voltage (I-V) measurement is used to investigate the performance of solar cells. In our I-V measurement setup, a Newport 67015 solar simulator using a 150 W Xenon lamp equipped with a 1.5 AM filter is used as a light source. A 1 cm × 1 cm calibrated PV measurements, Inc. Si solar cell is used as a reference cell to calibrate the intensity of the light source to AM 1.5G (100 mW/cm^2) for measurements. An HP 4155A Semiconductor Parametric Analyzer is used to measure current and voltage. Figure 6.7 shows the SNWSC characterized by measuring current-voltage curves in the dark and

under AM1.5G illumination. The SNWSC had an efficiency of 0.04%, short circuit current density J_{sc} = 0.23 mA cm^{-2}, open circuit voltage V_{oc} = 1.21V and fill factor (FF) = 0.16. The measured efficiency is lower than the theoretical limit calculated in Figure 6.6, which for a 1.96 eV bandgap the efficiency should be 1.8%. A low J_{SC} could be attributed to non-radiactive recombination. The recombination in single NW solar cell can result from (1) the nanowire outmost non-passivated surface; (2) defective growth at tip of NW due to Ga droplet was not fully depleted prior to the intrinsic GaNP shell growth; (3) N related defects in GaNP NW. The small fill factor (FF) indicates a large leakage current between base and emitter GaNP layers. During dry etching and wet etching steps to expose the core and subsequent evaporation of metal contact, the n-contact to the core is very likely to connect with intrinsic shell layer and p-shell layer through metal contact. Direct contacting the p-shell layer and n-type core layer leads to increasing the leakage current, consequently, a small shunt resistance and fill factor in the circuit.

To compare solar cell performance made of different materials, the bandgap (E_g) to V_{oc} offset (W_{oc}) is used.

$$W_{oc} = \frac{E_g}{q} - V_{oc} \tag{6.13}$$

W_{oc} theoretically and experimentally proven to be independent of E_g[8], and it is commonly used to perform for a fair comparison between solar cells that are comprised of different materials. It is basically a measure of how close electron and hole quasi-Fermi levels are to the conduction and valence band edges at open circuit. Usually a smaller W_{oc} represents better device performance. In this dissertation, we have achieved a relative low

bandgap to V_{oc} offset of 0.75 V. This number is lower than many reported single NW solar cell[9-11] including materials of Si and GaAsP. Although the power conversion efficiency is still low, the well-preserved V_{oc} opens up a broad opportunity and a bright future for GaNP single nanowire solar cell since there is still plenty of room for device improvement.

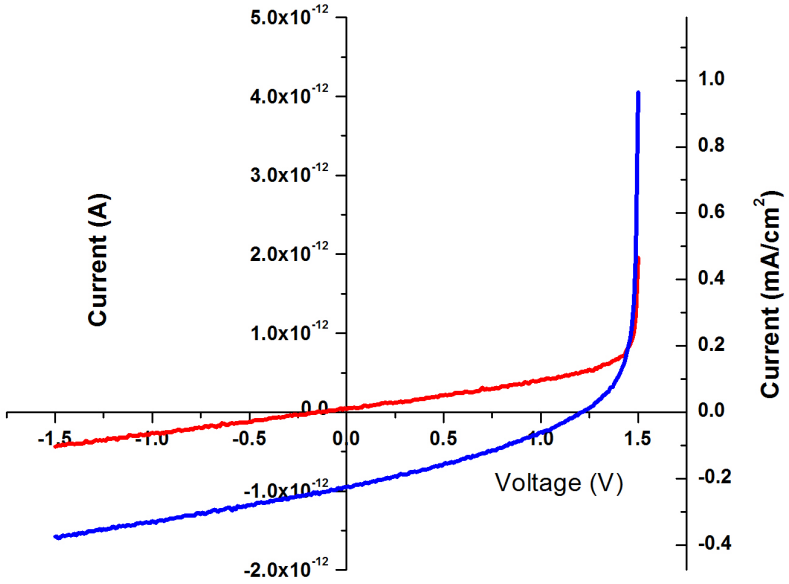

Figure 6.7 I-V characteristics under dark (red line) and AM1.5G illuminated conditions (blue line) of SNWSC.

6.6 Conclusion

In conclusion, we have fabricated a p-i-n GaNP core/shell/shell nanowire solar cell utilizing a complicated process: dry etching and wet etching to expose the cores and

deposit metal contact separately on the p and n regions. Simulations are performed to show the effect of different layer's thickness to device short circuit current and efficiency. Finally, a single NW solar cell performance is determined by using current density–voltage curve. A high V_{oc} (1.21V) has been achieved.

Reference

[1] A. Luque, A. Marti and A. J. Nozik, MRS Bull, 32, 236 (2007).

[2] B. Tian, T. J. Kempa, and C. M. Lieber, Chem. Soc. Rev., 38, 16 (2009).

[3] M. D. Kelzenberg, S. W. Boettcher, J. A. Petykiewicz, D. B. Turner-Evans, M. C. Putnam, E. L. Warren, J. M. Spurgeon, R. M. Briggs, N. S. Lewis, H. A. Atwater, Nat. Mater. 9, 239 (2010).

[4] M. L. Young and D. R. Wight. J. Phys. *D* 7,1824, (1974).

[5] Jenny Nelson. The physics of solar cells. Imperial College Press, 2013.

[6] Band structure and carrier concentration of GaP. http://www.ioffe.ru/SVA/NSM/ Semicond/GaP/bandstr.html, (accessed November, 2015).

[7] M. L. Young and D. R. Wight. J. Phys. *D* 7,1824, (1974).

[8] R. R. King, D. Bhusari, A. Boca, D. Larrabee, X. Q. Liu, W. Hong, C. M. Fetzer, D. C. Law, and N. H. Karam, Prof. Photovolt: Res. Appl. 19, 797 (2010).

[9] J. V. Holm, H. I. Jorgensen, P. Krogstrup, J. Nygard, H. Liu, and M. Aagesen, Nat. Photonics 7, 306 (2013).

[10] T. J. Kempa, B. Tian, D. R. Kim, J. Hu, X. Zheng, and C. M. Lieber, Nano Lett. 8, 3456 (2008).

[11] M. D. Kelzenberg, D. B. Turner-Evans, B. M. Kayes, M. A. Filler, M. C. Putnam, N. S.

Lewis, and H. A. Atwater, Nano Lett. 8, 710 (2008).

Appendix A

Python scripts for a p-i-n GaNP solar cell

Short circuit and Efficiency contour with various emitter and intrinsic layer thickness

The follow Python script is used to calculate the effect of the emitter layer thickness and intrinsic layer thickness to p-i-n GaNP solar cell short circuit current and efficiency in Section 6.4.

```
import math
import numpy as np
import pandas as pd
import matplotlib.pyplot as plt
from decimal import Decimal
```

```
#spectrum irradiance (W*m - 2*nm -1)
bs0 =
np.array([3.3569E-03,6.5654E-02,2.0579E-01,4.0688E-01,4.5418E-01,5.1862E-01,5.4231E-01,6
.6788E-01,1.0847E00,6.7673E-01,9.3964E-01,1.1668E00,1.2235E00,1.1376E00,1.3480E00,1.49
87E00,1.5611E00,1.5562E+00,1.5976E00,1.5198E00,1.5490E00,1.5578E00,1.4952E00,1.5348E
00,1.5353E00,1.5427E00,1.5153E00,1.4932E00,1.5042E00,1.4497E00, 1.4657E00, 1.4715E00,
1.4423E00, 1.4107E00, 1.4470E00, 1.4014E+00, 1.3570E+00 ,1.4139E+00,
1.3933E+00 ,1.2180E+00 ,1.2919E+00])
lam =np.arange(3.0000E2, 7.1000E2, 0.1000E2)
# reflectance of GaP
R =
np.array([0.335389271,0.338317678,0.358920463,0.387429202,0.46732241,0.462001638,0.4250
36008,0.410300539,0.397651128,0.386522899,0.376718617,0.368397468,0.361528971,0.35563
7645,.355637645,0.349013391,0.34002413,0.34002413,0.34002413,0.323432229,0.31695021,0.
31695021,0.311190855,0.311190855,0.305920486,0.301336477,0.301336477,0.297115935,0.29
7115935,0.293208024,0.293208024,0.289535326,0.289535326,0.286013677,0.286013677,0.286
013677,0.286013677,0.286013677,0.282968709,0.282968709,0.280219865])
# absorption coefficient of GaP
alpha =
np.array([436332,440026,455180,493335,249576,145283,97857,80000,71244,54643,43207,3405
4,30000,26896 ,16744,11000, 3694, 2500, 1450, 1000, 760, 600, 487, 350, 233,0,0,])
rest_alpha = np.repeat(0,14)
alpha = np.concatenate([alpha,rest_alpha])
#absorption coefficient of GaNP
alphaN = np.array([436332,440026,455180,493335,249576, 145283, 97857, 80000, 71244,
54643, 43207, 34054, 30000,
26896,24000,24000,24000,24000,24000,21000,21000,21000,21000,19777.34352, 18140.75909,
```

```
15074.87478, 12736.7502 ,10047.57244, 6987.87609, 3876.71375, 1677.71656, 527.5873,
204.7378 ,5.74542, 0.19919,0, 0, 0 ,0, 0, 0])

#parameter fo structure
print bs0[29], lam[29], R[29], alpha[20], alphaN[29]
EgN = 1.96 #bandgap of GaNP, eV
n = 1
q = 1.6E-19
Nc = 1.8E19
Nv = 1.9e19
De = 1.68
Ne = 3E18
Le = 35E-7
Se = 1e6
We = 40e-7

Db = 1.53
Nb = 4e17
Lb = 35e-7
Sb = 1e6
Wb = 80e-7
tb = 1e-6

bs = bs0/q*lam/1240

wis = np.arange(10e-7,11e-6,10e-7)
wes = np.arange(10e-7,11e-6,10e-7)
```

```
def contour_plot(data_matrix1, title):


    plt.figure()
    X,Y = np.meshgrid(wes/1e-7,wis/1e-7)
    cp = plt.contour(X,Y,data_matrix1)
    plt.clabel(cp,colors = 'blue',inline=True, fontsize = 10, fmt = '%0.1f')
    plt.title('{} contour map'.format(title))
    plt.xlabel ('emitter layer thickness (nm)')
    plt.ylabel ('intrinsic layer thickness (nm)')
    plt.show()


def cal_of_efficiency (wis,wes):
    Jsc = [[0]*len(wes) for i in range(len(wis))]
    for i, Wi in enumerate(wis):
        for j, We in enumerate(wes):
            bs = bs0/q*lam/1240
            Jln1 = q*bs*(1-R)*alphaN*Le/((alphaN*Le)**2-1)
            Jln2 =
(Se*Le/De+alphaN*Le)-np.exp(-alphaN*We)*(Se*Le/De*np.cosh(We/Le)+np.sinh(We/Le))
            Jln3 = Se*Le/De*np.sinh(We/Le) + np.cosh(We/Le)
            Jln4 = alphaN * Le*np.exp(-alphaN*We)
            Jln = Jln1*(Jln2/Jln3-Jln4)


            Jlp1 =
(q*bs*(1-R)*alphaN*Lb/((alphaN*Lb)**2-1))*np.exp(-alphaN*We)*np.exp(-alphaN*Wi)
            Jlp2 = Sb*Lb/Db*(np.cosh(Wb/Lb)-np.exp(-alphaN*Wb))
```

```
            Jlp3 = np.sinh(Wb*Lb)+alphaN*Lb*np.exp(-alphaN*Wb)
            Jlp4 = Sb*Lb/Db*np.sinh(Wb/Lb)+np.cosh(Wb/Lb)
            Jlp5 = alphaN*Lb
            Jlp = Jlp1*(Jlp5-(Jlp2+Jlp3)/Jlp4)

            Jgen = q*bs*(1-R)*np.exp(-alphaN*We)*(1-np.exp(-alphaN*Wi))

            J = Jln + Jlp + Jgen
            QE1 = J/(q*bs)
            Jsc[i][j] = float("%0.2f"%(0.1*np.trapz(J, lam)))

    return Jsc

Jsc = cal_of_efficiency(wis, wes)
contour_plot(Jsc, "Jsc (mA/cm2)")
te = 1e8
effs = [[0]*len(wes) for i in range(len(wis))]
for i, Wi in enumerate(wis):
    for j, We in enumerate(wes):
        #diffusion current
        Jn =
q*De*Nc*Nv/Le/Ne*((Se*np.cosh(We/Le)+De/Le*np.sinh(We/Le))/(De/Le*np.cosh(We/Le)+S
e*np.sinh(We/Le)))
        Jp =
q*Db*Nc*Nv/Lb/Nb*((Sb*np.cosh(Wb/Lb)+Db/Lb*np.sinh(Wb/Lb))/(Db/Lb*np.cosh(Wb/Lb)+
Sb*np.sinh(Wb/Lb)))
        J0 = (Jn+Jp)*np.exp(-EgN/0.0259)
```

```
            # recombination current at depletion region
            Jscr = q*((Nc*Nv/te/te)**(1/2))*Wi
            Jscr1 = Jscr*np.exp(-EgN/2/0.0259)

            # total dark current
            Jt = J0 + Jscr1

            # open circuit voltage
            Voc = 0.0259 * np.log(Jsc[i][j]/Jt + 1)

            # fill factor
            Voc1 = Voc/0.0259
            FF = (Voc1 - np.log(Voc1 + 0.72)) / (Voc1 + 1)

            effs[i][j] = Jsc[i][j] * Voc * FF

contour_plot(effs, "efficiency (%)")
```